Stony Brook University

OFFICIAL COPY

The official electronic file of this thesis or dissertation is maintained by the University Libraries on behalf of The Graduate School at Stony Brook University.

© All Rights Reserved by Author.

Analysis of the vibrational structure in the electronic spectra of molecules: Phenylacetylene as a prototype molecule

A Dissertation Presented

by

Gary Vladimir Lopez

to

The Graduate School

in Partial Fulfillment of the

Requirements

for the Degree of

Doctor of Philosophy

in

Chemistry

(Chemical Physics)

Stony Brook University

August 2012

Copyright by
Gary Vladimir Lopez
2012

Stony Brook University
The Graduate School

Gary Vladimir Lopez

We, the dissertation committee for the above candidate for the
Doctor of Philosophy degree, hereby recommend
acceptance of this dissertation.

Trevor J. Sears
Professor of Chemistry, Department of Chemistry, Advisor

Philip M. Johnson
Professor of Chemistry, Department of Chemistry, Chairman

David M. Hanson
Professor of Chemistry, Department of Chemistry

Thomas Weinacht
Professor of Physics, Department of Physics

This dissertation is accepted by the Graduate School

Charles Taber
Interim Dean of the Graduate School

Abstract of the Dissertation

Analysis of the vibrational structure in the electronic spectra of molecules: Phenylacetylene as a prototype molecule

by

Gary Vladimir Lopez

Doctor of Philosophy

in

Chemistry

(Chemical Physics)

Stony Brook University

2012

Experimental studies of phenylacetylene (PA) in the gas phase previously revealed an unusual new set of photophysical properties following the $S_1 \leftarrow S_0$ excitation. The decay of the initially excited level showed the expected short (75ns) lifetime component assigned to the S_1 state and a second very long lifetime (>100 microsec) component that were both created during the excitation laser pulse [Hofstein J., Xu H., Sears T. J., Johnson P. M., J. Phys. Chem. A **112** (2008)].

To investigate the identity and formation mechanism of the long-lived species, a good understanding of the vibrational structure in the $S_1 \leftarrow S_0$ spectrum of PA is required. The interaction of the vibrational and electronic (vibronic) motions was calculated in order to predict the $S_1 \leftarrow S_0$ electronic spectrum of PA using a combination of time-dependent density functional theory (TD-DFT) electronic structure codes, Franck-Condon integral calculations, and a second order vibronic model developed previously [Johnson P. M., Xu H. F., Sears T. J., J. Chem. Phys. **125** (2006)]. The sensitivity of the calculations to different DFT functionals (B3LYP, LC-BLYP and CAM-B3LYP) and basis sets (aug-cc-pVDZ and aug-cc-pVTZ) was explored and compared to accurate experimental relative intensities of the vibrational bands up to energies of 2000 cm^{-1} above the band origin obtained by recording the $S_1(A\ ^1B_2) \leftarrow S_0(X\ ^1A_1)$ electronic transition using resonance-enhanced multiphoton ionization spectroscopy (1+1 REMPI) in a molecular beam and cavity-ringdown (CRD) absorption spectroscopy in a slit jet-cooled sample. The long-range corrected functional CAM-B3LYP resulted in a 5 times bigger equilibrium transition moment than B3LYP, a result more closely matching the observations. The LC-BLYP result is yet 36% higher than CAM-B3LYP. It was observed that CAM-B3LYP produced a good match to most of the experimental spectrum. However, a superior match was observed when the CAM-B3LYP equilibrium transition moment and the moment derivatives from the B3LYP calculation were combined in the simulation. Results from the CRD experiment showed errors in relative

intensities derived from the REMPI spectra, showing that REMPI spectroscopy is a less than accurate technique in this regard.

Further pump-probe photoionization experiments not only confirmed Hofstein et al.'s observations but showed that some of strong assigned vibrational modes ($\nu_{\beta cc}$ and ν_{15}) enhanced the formation of the long-lived species compared to others. The motion of the atoms in $\nu_{\beta cc}$ and ν_{15}, along with the computational analysis of the energies of electronic states of different PA isomers with respect to the S_1 state of PA., suggest isomer formation as a possible explanation for the observed long-lived species. The triplet ground state of Cycloocta-1,3,5-trien-7-yne (COTY), for example, appears to be a good candidate However, the evidence is still far from conclusive and additional experimental work is required to investigate the intriguing complexity in the photophysics of PA.

To my wonderful family, Gary Gonzalo and Maria Magdalena Lopez, without their continued support and counsel I would not have been able to get this far. A special feeling of gratitude to my beloved Jeniffer Quijada whose words of encouragement and push for tenacity, along with her understanding and advice, supported me throughout the whole process. To my grandparents, for always taking care of me and my family, I will always love and remember you. Thank you papa Amaro.

Frontispiece

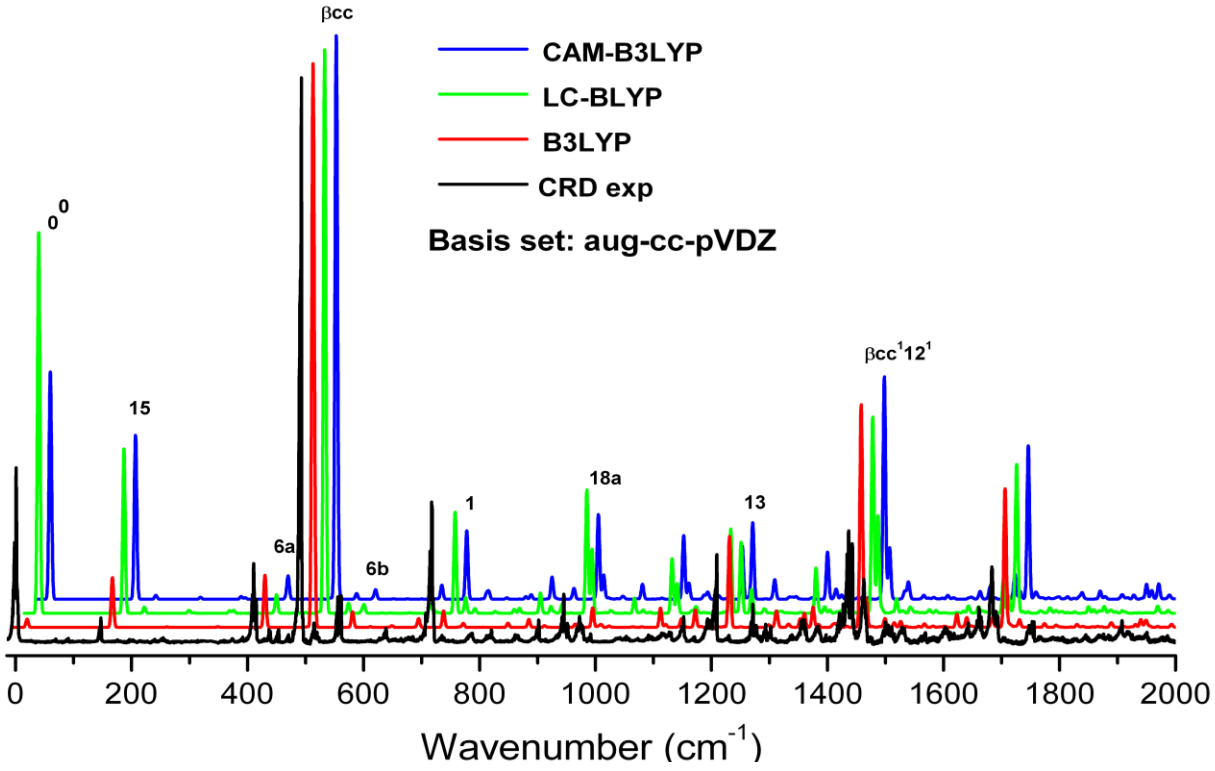

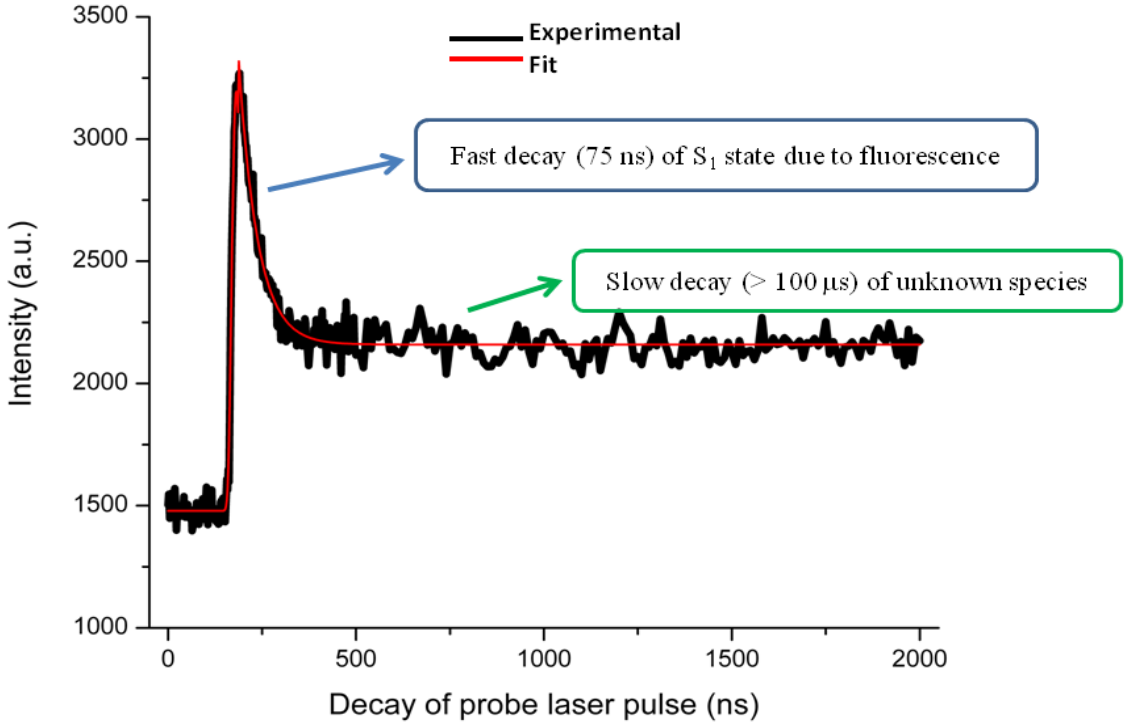

Table of Contents

List of Figures

List of Tables

List of Abbreviations

B3LYP: Becke, three-parameter, Lee-Yang-Parr functional

BBO: Beta Barium Borate crystal

BCBD: Benzocyclobutadiene

BN: Benzonitrile

CAM-B3LYP: long range corrected version of B3LYP using the Coulomb-Attenuating Method

CASSCF: Complete active space self-consistent field

CCO: Cavity coupling optics

CIS: Configuration interaction singles

COTY: Cycloocta-1,3,5-trien-7yne

CRD: Cavity ring-down

DA: Direct absorption

DFT: Density functional theory

EEL: Electron-energy-loss spectrum

eV: Electron volts

F548: Fluorescein 548: 9-(o-Carboxyphenyl)-2,7-dichloro-6-hydroxy-3H-xanthen-3-on-2,7-Dichlorofluorescein

GGA: Generalized gradient approximation

HF: Hartree-Fock

HS: Harmonic separator

HOMO: Highest occupied molecular orbital

IC: Internal conversion

ISC: Intersystem crossing

IP: Ionization Potential

LC-BLYP: long correction of Becke, one-parameter, Lee-Yang-Parr functional

LIF: Laser-induced fluorescence

LLS: Long-Lived Species

LRC: Long-range corrected

LUMO: Lowest unoccupied molecular orbital

MATI: Mass analyzed threshold ionization

MCP: Micro-channel plate detector

MCSCF: Multiconfigurational self-consistent field

MPI: multiphoton ionization

Nd :YAG : neodymium-doped yttrium aluminium garnet ($Nd:Y_3Al_5O_{12}$)

NI-DAQ: National Instruments Data Acquisition

OPO: Optical Parametric Oscillators

PA: Phenylacetylene

PED: Pyroelectric detector

PES: Photo-electron spectroscopy

PG: Pulse generator

PIRI: Photoinduced Rydberg Ionization spectroscopy

PMT: Photomultiplier Tube

PV: Phenyl-Vinylidene

R560: Rhodamine 560: o-(6-Amino-3-imino-3H-xanthen-9-yl)-benzoic acid

RDC: Ringdown cavity

REMPI: Resonance Enhanced Multiphoton Ionization

SCF: Self-consistent field

SD: Standard deviation

SHG: Second harmonic generation

TD-DFT: Time-dependent density functional theory

TM: Transition moment

TOF: Time-of-Flight

WR: Wedged reflector

ZEKE: Zero kinetic energy

Preface

The present dissertation mainly involves four publications. Two of them were previously published by former members of the group and served as starting points and good references for this work while the other two are based on recent results.

As a graduate student at SBU, I got the opportunity to continue a very exciting project which began when Dr. Xu, a post-doc in Dr. Johnson's group, experimentally observed unusual photophysical properties when studying small benzene-based aromatic molecules such as phenylacetylene and benzonitrile. There followed a continuing collaboration between the Johnson and Sears groups to investigate the new photophysics. As a new graduate student in the group, I was able to assist Dr. Chih-Hsuan Chang, a postdoctoral associate, to perform resonance-enhanced multiphoton ionization and velocity map imaging experiments to have more reliable assignments of the vibrational structure of the electronic $S_1 \leftarrow S_0$ transition of phenylacetylene. Later, as a more independent student working under Dr. Johnson's supervision, I was able to perform pump-probe delayed experiments in an effort to identify the strong active vibrations of the $S_1 \leftarrow S_0$ transition of phenylacetylene that may be related to the formation of the long-lived species previously observed. Then, to check the relative band intensities obtained in the resonance-enhanced multiphoton ionization experiments, Dr. Chang and I, with the help of Dr. Gregory Hall and Dr. Alexey Teslja, performed experiments using cavity-ringdown spectroscopy, a direct absorption technique.

As part of my academic formation, I took a course taught by Dr. Johnson related to theoretical studies of the electronic structure of molecules where I was introduced to the basics behind the calculations and the computational programs used (e.g. Gaussian). In fact, Gaussian is used in this work to obtain the optimized geometry, vibrational vectors and frequencies and the

transition moments needed to simulate the vibronic spectra of phenylacetylene. As it is well-known, methods using the most accurate theories have to be compared to accurate experimental data in order to have a refine assignment of any spectra.

The work done in the present dissertation was carried out at Stony Brook University and at Brookhaven National Laboratory under Contract No. DE-AC02-98CH10886 with the U.S. Department of Energy, Office of Science, and supported by its Division of Chemical Sciences, Geosciences, and Biosciences within the Office of Basic Energy Sciences.

Gary V. Lopez

Acknowledgments

I owe my gratitude to all those people who have made this dissertation possible and because of whom my graduate experience has been one that I will cherish forever.

My deepest gratitude is to my advisor, Dr. Trevor Sears. I have been amazingly fortunate to have an advisor who gave me the freedom to explore on my own and at the same time the guidance to recover when my steps faltered. Trevor taught me how to question thoughts and express ideas. His patience and support helped me overcome different situations and finish this dissertation. I hope that one day I would become as good advisor as Trevor has been to me.

My co-advisor, Dr. Philip Johnson, has been always there to listen and give advice. I am deeply grateful to him for the long discussions that helped me sort out all the details of my work. I am also thankful to him for encouraging the use of correct grammar and consistent notation in my writings and for carefully reading and commenting on countless revisions of my reports, posters and presentations among my graduate studies; including this manuscript. Philip is one of the best teachers that I have had in my life. He encourages and guides his students to meet high standards. He introduced me to *ab initio* computer calculations for the study of the physical and chemical properties of molecules and his teachings inspired me to work different parts of this dissertation and previous manuscripts required to advance towards the graduate program. I am indebted to him for his continuous encouragement and guidance.

Dr. Chih-Hsuan Chang's insightful comments and constructive criticisms were thought-provoking and they helped me focus my ideas. I am grateful to him for the long discussions that helped me sort out the technical details of the different devices used in my research.

I am indebted to the members of Gas Phase Molecular Dynamics group at Brookhaven National Laboratory and the members of the Molecular Spectroscopy and Dynamics group at Stony Brook University with whom I have interacted during the course of my graduate studies.

Particularly, I would like to acknowledge Dr. Gregory Hall, Dr. Christopher McRaven and my lab partner Matthew Cich for the many valuable discussions that helped me to better understand our research.

I am thankful to the scientists I have met inside and outside the Stony Brook community. I would like to thank the members of the Nuclear Chemistry group at Stony Brook University, in particular to Dr. Roy Lacey, for his encouragement and advice during the first year of my graduate studies, and Dr. Jiangyong Jia. I am thankful to Dr. Maria-Luisa Tasayco from CUNY/CCNY, Dr. Alexey Teslja from Fairleigh Dickinson University and Dr. Natalia Inostroza from NASA Ames Research Center. I would like to acknowledge Dr. Arlan Mantz, Oakes Ames Professor Emeritus of Physics at Connecticut College, for the numerous discussions and comments on topics related to the analysis of the molecular absorption lineshapes that helped me improve my knowledge in the area.

I would like to thank to the members of the Chemistry Department at Stony Brook University for making my years in graduate school a pleasant experience. I would like to thank my committee members for commenting on my views and helping me understand and enrich my ideas and Dr. Nancy Goroff, the graduate program director. Special thanks to the people from the Chemistry office: Katherine Hughes, Heidi Ciolfi, Charmine Yapchin, Barbara Schimmenti, Norma Reyes and Liz Perez for all her administrative help.

Most importantly, none of this would have been possible without the love, patience and help of my family, my beloved Jeniffer and my good friends: Prof. Bertha Llanos, Prof. Lily Chang, Aurelina de la Cruz, Cesar Calonge, Rodney Versace and all my friends from the Chemistry department at UPCH, especially Mr. Sabino Marquez.

Fields of Study and Publications

Biochemistry/Biophysics

[1] Quijada J., Lopez G., Versace R., Ramirez L., Tasayco M.L., "On the NMR analysis of pKa values in the unfolded state of proteins by extrapolation to zero denaturant", Biophys. Chem., **2007**, 129, 242.

[2] Huber D., Cha M., Debarbieux L., Planson A., Cruz N., Lopez G., Tasayco M.L., Chaffotte A. and Beckwith J., "A selection for mutants that interfere with folding of Escherichia coli thioredoxin-1 in vivo", Proc. Nat. Acad. Soc., **2005**, 102, 18872.

Chemical Physics/Physical Chemistry

[1] Lopez G., Chang C., Johnson P., Hall G., Sears T., Markiewicz B., Milan M., Teslja A., "What is the best DFT functional for vibronic calculations? A comparison of the calculated vibronic structure of the $S_1 \leftarrow S_0$ transition of phenylacetylene with cavity ringdown band intensities" [Submitted to JPCA, March **2012**].

[2] Cich M., McRaven C., Lopez G., Sears T., Hurtmans D. and Mantz A., "Temperature-dependent pressure broadened line shape measurements in the $\nu_1 + \nu_3$ band of acetylene using a diode laser referenced to a frequency comb.", Appl. Phys. B: Lasers and Optics, **2011**, Springer Berlin / Heidelberg, Issn: 0946-2171, Doi: 10.1007/s00340-011-4829-0.

[3] McRaven C., Cich M., Lopez G., Sears T., Hurtmans D. and Mantz A., "Frequency comb-referenced measurements of self- and nitrogen-broadening in the ν1+ν3 band of acetylene", J. Mol. Spectrosc., **2011**, 266, 43.

[4] Chang C., Lopez G., Sears T. and Johnson P., "Vibronic analysis of the $S_1 \leftarrow S_0$ transition of phenylacetylene using photoelectron imaging and spectral intensities derived from electronic structure calculations", J. Phys. Chem. A, **2010**, 114, 8262.

[5] Lopez G., "Inhibición de la corrosión de aluminio y cobre con 5-aminotetrazol en agua de mar. / Corrosion inhibition of aluminum and copper with 5-aminotetrazole in seawater." **2004**, PE1.1; TL-UPCH, TA462, L83, BC:20040705:TL-829/TL-829a.

CHAPTER 1

INTRODUCTION

Molecular vibrations are important in energy transfer processes, chemical reactions, non-radiative transitions and in forbidden spectroscopic transitions that are allowed by excitation of non-totally symmetric vibrations. However, accurate information regarding molecular potential energy surfaces which govern vibrational motion and many photochemical and photophysical processes in electronic ground and excited states is not available for many substituted benzenes.

Aryl olefins of many types of substituted benzenes are important because they can be considered as simple models for the study of substituted aromatic hydrocarbons where the phenyl group is conjugated with a chromophoric substituent. The presence of substituent chromophoric groups raises the question about the underlying mechanism responsible for the observed spectroscopic patterns in a specific electronic excitation. An understanding of the interactions between the differently bounded π-electron systems can be applied to a variety of chemical, physical and biological processes.

The accurate structural characterization of electronically excited states of these species is largely reliant upon the availability of spectroscopic techniques with sufficiently high resolution to allow complete rotational analysis of the resulting spectra. The experimental challenges are great because of the associated small rotational constants, particularly in molecules with a heavy or bulky substituent.

Phenylacetylene (PA), an aryl olefin with possible conjugative interaction between the benzene and acetylene fragment, serves as a good model to understanding the delocalization effects. PA is a molecule with C_{2v} symmetry and a large number of vibrational degrees of

freedom. It has 36 non-degenerate normal modes, 13 of which belong to a_1 symmetry, 3 to a_2, 8 to b_1 and 12 to b_2. Figure 1.1 displays the molecular structure of PA.

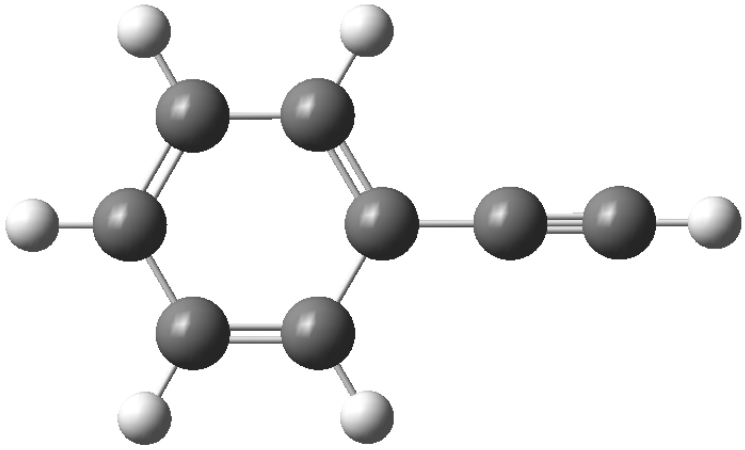

Figure 1.1: Molecular Structure of Phenylacetylene

The literature on experimental techniques applied to the study of PA is enormous [1-9]. Sponer et al. [10] revealed that the intensity observed in the symmetry forbidden $^1B_{2g} \leftarrow {}^1A_{1g}$ excitation in benzene derives entirely through vibronic interactions. Later, Padhye et al. [5] did the first systematic study on the infrared and Raman in the electronic ground state of PA giving a tentative assignment of some of the vibrational bands. Evans et al. [11] did a more complete vibrational analysis. King and So [1-4] extensively studied the infrared and Raman spectra of four isomers of PA (C_6H_5CCH, C_6H_5CCD, C_6D_5CCH and C_6D_5CCD) and refined the spectroscopic assignments. They also recorded the rotational band contours in gas phase absorption, analyzed all the active vibrations in the S_0 and S_1 states and assigned the electronic origin of the spectrum. In fact, they defined the electronic origin to be 35879 cm^{-1} and corrected the prervious work of Padhye et al.[5] who assigned the 36 370 cm^{-1} band as the band origin. Another important conclusion from King and So's work on the $S_1 \leftarrow S_0$ transition of PA was that this transition arises from the $^1B_{2g} \leftarrow {}^1A_{1g}$ excitation in benzene.

Powers et al. [7] confirmed King and So's results by looking at the $S_1 \leftarrow S_0$ transition of PA with the fluorescence excitation of a supersonic jet-expanded sample. The low vibrational and rotational temperature provided by a supersonic expansion removed the sequence band congestion and rotational broadening of the ambient temperature sample. Their fluorescence excitation spectrum also revealed that the spectrum of low-intensity transitions (L_b, according to Platt's notation) possesses much more forbidden character than allowed Franck-Condon (FC) character. According to Platt's notation, the lowest four electronic levels common to all cata-condensed hydrocarbons are ^1L_b, ^1L_a, ^1B_b and ^1B_a. The L transitions are generally almost forbidden (especially the ^1L_b transition) having very small oscillator strength, while the B transitions are strongly allowed, having typically oscillator strengths between one to two orders

of magnitude larger than the L transitions. The subscript "a" stands for electronic levels having the electron density of the electrons on the atoms and the nodal points (zero electron density points) on the bonds connecting the atoms; subscript "b" stands for electronic levels having the electron density of the π–electrons on the bonds and the nodal points on the atoms [12, 13]. Chia et al. [8] who also studied the $S_1 \leftarrow S_0$ transition of PA, using two photon spectroscopy concluded that the π electrons are delocalized over the ring and the acetylene parts of PA.

Techniques like photoelectron spectroscopy (PES), laser-induced fluorescence (LIF) spectroscopy and multiphoton ionization (MPI) have been applied on the study of the photophysics of aromatic substituted molecules like PA [14]. Although PES is a useful technique to investigate electronic states, the poor resolution that this method provides (around 10 meV or 80 cm^{-1}) does not allow obtaining resolved vibrational spectra of polyatomic ions [15]. Laser-induced fluorescence spectroscopy usually has higher resolution than PES and can resolve vibrational peaks. However, it is not generally applicable because most of the excited electronic states of polyatomic cations do not fluoresce [16]. Better resolution than the one achieved with conventional PES has been obtained with two or more laser-photon excitations to study molecular energy levels, a technique known as multi-photon ionization (MPI).

Higher resolution has been achieved using Zero kinetic energy (ZEKE) photoelectron spectroscopy and mass analyzed threshold ionization (MATI). ZEKE spectroscopy involves the detection of electrons with essentially zero kinetic energy formed on photoionisation. These electrons are field-ionised electrons arising from high-lying Rydberg states formed by excitation from the initial level. When the extraction pulse is applied, these Rydberg states are ionised and the electrons formed are detected along with the ZEKE electrons [17, 18]. MATI basically employs the same principle as ZEKE, except that it detects ions instead of electrons and gives

mass-selectivity in the spectra. A high-resolution electron-energy-loss spectrum (EEL) of solid PA was obtained by Swiderek et al. [19] who observed more vibronic structure in the lowest singlet-triplet transition than had been previously available. Meanwhile, Ribblett et al. [20] obtained the spectra of several vibronic bands in the $S_1 \leftarrow S_0$ electronic transition of PA by rotationally resolved fluorescence excitation spectroscopy. Their study confirmed that the band origin of PA is a b-type band and showed that its S_1 state is ^1L_b in character [13]. Kim et al. [9] used MATI spectroscopy to obtain the one-photon MATI spectra of PA reporting the vibrational frequencies of its the molecular ion while vibrational analysis of the third excited electronic state of the $\hat{C}$ state of PA cation was obtained by Johnson et al. using photoinduced Rydberg ionization (PIRI) spectroscopy [21, 22].

The combination of supersonic jet-cooled resonance-enhanced multiphoton ionization (REMPI) with time-of-flight mass spectrometry (TOFMS) is an effective means of probing the photophysical and photochemical properties of polyatomic molecules and clusters [23]. Narayanan et al. [23] and Philis et al. [24] have examined the one-photon and two-photon $S_1 \leftarrow S_0$ spectra of jet cooled PA using these techniques.

Chang et al. [25] combined 1+1 REMPI with slow electron velocity mapping imaging photoelectron spectroscopy to analyze the vibrational structure of the $S_1 \leftarrow S_0$ electronic band of PA. Using photoelectron imaging with velocity mapping allows the measurement of the photoelectron spectrum and the angular distribution at the same time, a great advantage over techniques in which photoelectrons are detected in a small solid angle.

Experimental studies on the electronic spectra of aryl olefins have been complemented by self-consistent field (SCF) quantum chemical calculations. The wave functions, energies and intensities of these molecules in their ground electronic states have been determined [24, 26].

Reliable results obtained at a variety of basis sets and levels of theory and algorithms that take advantage of recently developed technology, i.e. more sophisticate and faster computers, have made these methods more popular [23-26]. Although more accurate descriptions of the observed experimental features are now possible with the help of computational methods, especially for calculations of the ground states in small systems, these methods are found to be less accurate for larger molecules like PA, in their excited states.

For the specific case of PA, theoretical calculations of the molecular geometry and vibrational spectrum in the ground state have been well documented in the literature. King and So's [4] results of LCAO-SCF (molecular orbitals approximated by a linear combination of the atomic orbitals) calculations suggested that the ground state (S_0) and the first excited electronic state (S_1) are planar with C_{2v} symmetry point group. Additionally, they reported that the π molecular orbitals involved in the transition are localized in the ring and not in the acetylenic group. King and So's results were supported by Császár et al. [27] using ab initio Hartree-Fock (HF) calculations with a 4-21 Gaussian (4-21G) basis set and reporting the optimized geometry and the complete harmonic force field of PA. However, the transition was shown to be more complex when King and Van Putten [28] found that the transition involved a contribution from the acetylenic group when using CNDO/CI theory. Later, a systematic study on the completely optimized geometries and vibrational frequencies of PA in both the S_0 and S_1 states calculated using the HF and CIS methods with the 4-31G and 6-31G basis sets was done by Narayanan et al. [23]. Serrano-Andrés et al. [26] applied a high-level theoretical approach on this system known as the multiconfigurational complete active space self-consistent field (CASSCF) method. Based on their calculations performed on the singlet and triplet valence, and Rydberg excited states of PA, they assigned the $^1B_2$ (^1L_b) valence $\pi \rightarrow \pi^*$ excited state related to the S_1-S_0

transition as the lowest singlet state responsible for a very weak band at 4.5eV while the 2 $^1A_1$ (^1L_a) valence $\pi \rightarrow \pi^*$ excited state related to the S_2-S_0 transition as the second and medium intensity band of the absorption spectrum at 5.2 eV. Higher accuracy calculations at CASSCF and second-order multireference Möller-Plesset (MRMP2) of the electronic structure of PA for S_0, S_1 and S_2 by Amatatsu et al. [29] characterized the stable structure of the S_1 state as an enlarged benzene ring caused by the local $\pi \rightarrow \pi*$ excitation within the benzene ring. These results did not agree with King and Van Putten's results. In subsequent work using the same levels of theory, Amatatsu [30] studied the reaction coordinate of the S_2-S_1 internal conversion (IC) of PA. Their calculations showed that the aromatic benzene ring became a quinoid structure while the ethynyl group changed into an allenoid skeleton in the S_2 state but once it relaxed into S_1, it changed quickly into an enlarged benzene ring which they have found to be the most stable geometry in S_1. More recently, Chang et al. [25] calculated the vibrational frequencies and vectors for both S_0 and S_1 states using CASSCF and a large basis set (the Dunning aug-cc-pVDZ basis set); while the electronic transition moments were calculated using time-dependent density functional theory (TD-DFT) in an effort to obtain the simulated the complete S_1-S_0 spectrum of PA with accurate intensities and frequencies. A comparison of their simulated spectra to their experimental REMPI was found satisfactory when the a_1 modes were scaled up by a factor of 3.5. REMPI is a technique that depends on details of the laser pulse shape and focusing since it is a multiphoton process and is a less suitable technique when it comes to quantitative relative band intensities measurements. A more accurate measurement can be made by direct absorption techniques such as cavity-ring down (CRD). With these ideas in mind, we have re-measured the spectrum using CRD spectroscopy and refined the computational model. The comparison with

theory was even more satisfactory than Chang's et al. [25] and brought more insight into the understanding of the electronic spectrum of this molecule.

Further interest in the photophysical properties was opened up when Hofstein et al. [31] found the formation of an unexpected long lifetime (>>100 μs) species after PA was excited to its S_1 state by using two-color pump-probe delayed photoionization technique. A possible explanation for this long lifetime species could be the production of the lower vibrational levels of the triplet manifold due to the dissociation of clusters. However, by looking at the rotationally resolved structure of the origin band of the PA $S_1 \leftarrow S_0$ transition at different pump-probe delays times, Xu et al. [32] demonstrated that the cause for the formation of the long-lived species was the excitation of the isolated monomer and not the production of the triplet manifold due to clusters.

Photo-electron spectroscopic (PES) experiments previously done in our group [31, 32] have shown that the long-lived component is independent of the singlet and triplet manifolds. Moreover, the typical lifetime of higher triplet states of aromatic molecules formed after intersystem crossing from the excited state is much smaller than the lifetime of the unexpected species, which is longer than 100 μs. Overall, the experimental evidence has opened the possibility of explaining the formation of the long lifetime component as due to an isomerization.

Searching for specific vibrational motions that might be related to isomerization pathways that could lead to the identification of the long lifetime component, our group has recently observed that some of the vibrational modes better promote the formation of the long-lived species than others. In fact, the excitation of the non-symmetric, and Coriolis active, ν_{15} and $\nu_{\beta CC}$ modes of the S_1 state seems to increase the yield of the long-lived states.

In Chapter 2, we report the $S_1(A\ ^1A_1) \leftarrow S_0(X\ ^1A_1)$ absorption spectrum of PA measured with spectroscopic techniques (1+1 REMPI, CRD spectroscopy) and theoretical methods in the time-dependent approach in an effort to provide more information for vibrational assignments of this transition and to understand the vibrational structure of the electronic spectrum of this molecule. In Chapter 3, we report the pump-probe delay photoionization decay curve for the band origin and four other previously assigned strong bands in the $S_1 \leftarrow S_0$ transition of PA at different sample pressures complemented with theoretical calculations of the ionization potential of some isomers of PA to indicate in the best case scenario the possible isomerization pathway. Finally, other spectroscopic techniques are suggested as possible future experiments in Chapter 4 to gather more evidence about the identity of the long-lived species.

REFERENCES

1. King G. W., So S. P., *"Allowed and Forbidden Components in 2790 a System of Ethynylbenzene"*. Journal of Molecular Spectroscopy **33**, 376 (1970).

2. King G. W., So S. P., *"Ethynylbenzene - Vibrational Spectra of Some Deuterated Isomers"*. Journal of Molecular Spectroscopy **36**, 468 (1970).

3. King G. W., So S. P., *"Ethynylbenzene Analysis of 2790 a Absorption System"*. Journal of Molecular Spectroscopy **37**, 543 (1971).

4. King G. W., So S. P., *"Ethynylbenzene Calculations of Energies of Electronic States"*. Journal of Molecular Spectroscopy **37**, 535 (1971).

5. Padhye M. R., Rao B. S., *"Infrared Spectra of Substituted Acetylenes"*. Journal of Scientific and Industrial Research B **18B**, (1959).

6. Zhuravleva T. S., Nurmukhametov R. N., Kozlov Y. I., Shigorin D. N., *"Electronic transitions and spectra of phenylacetylene"*. Optika i Spektroskopiya **22**, 898 (1967).

7. Powers D. E., Hopkins J. B., Smalley R. E., *"Vibrational-Relaxation in Jet-Cooled Phenylalkynes"*. J Chem Phys **74**, 5971 (1981).

8. Chia L., Goodman L., *"2-Photon Spectrum of Phenylacetylene"*. J Chem Phys **76**, 4745 (1982).

9. Kim M. S., Kwon C. H., Kim H. L., *"Vibrational analysis of vacuum ultraviolet mass-analyzed threshold ionization spectra of phenylacetylene and benzonitrile"*. Journal of Physical Chemistry A **107**, 10969 (2003).

10. Sponer H., Nordheim G., Sklar A. L., Teller E., *"Analysis of the near ultraviolet electronic transition of benzene"*. J Chem Phys **7**, 207 (1939).

11. Evans J. C., Nyquist R. A., *"The Vibrational Spectra of Ethynyl Benzene and Ethynyl Benzene-D"*. Spectrochimica Acta **16**, 918 (1960).

12. Rappoport Z., *The Chemistry of Phenols*. (John Wiley & Sons Ltd., England ed., 2003).

13. Platt J. R., *"Classification of Spectra of Cata-Condensed Hydrocarbons"*. J Chem Phys **17**, 484 (1949).

14. Dyke J. M., Ozeki H., Takahashi M., Cockett M. C. R., Kimura K., *"A Study of Phenylacetylene and Styrene, and Their Argon Complexes Pa-Ar and St-Ar with Laser Threshold Photoelectron-Spectroscopy"*. J Chem Phys **97**, 8926 (1992).

15. Baltzer P., Karlsson L., Wannberg B., Ohrwall G., Holland D. M. P., M. M., Hayes M., von Niessen W., *"An experimental and theoretical study of the valence shell photoelectron spectrum of the benzene molecule"*. Chemical Physics **224**, (1997).

16. Maier J., *Kinetics of Ion-Molecule Reactions*. P. Ausloos, Ed., (Plenum Press, New York ed., 1979).

17. Wright T. W., Cordes E., Dopfer O., Muller-Dethlefs K., *"Zero-kinetic-energy (ZEKE) Photoelectron Spectroscopy of the Hydrogen-bonded Phenol-Methanol complex"*. J. Chem. Soc. Far. Trans. **89**, (1993).

18. Yeretzian C., Selzle H., Schlag E., *"ZEKE spectroscopy: high-resolution laser spectroscopy in a modified time-of-flight mass spectrometer"*. Eur. Mass. Spectrom. **2**, (1996).

19. Swiderek P., Gootz B., Winterling H., *"Electron-energy-loss spectroscopy of solid phenylacetylene"*. Chemical Physics Letters **285**, 246 (1998).

20. Ribblett J. W., Borst D. R., Pratt D. W., *"Styrene and phenylacetylene: Electronic effects of conjugating substituents "off" and "on" the axis of a benzene ring"*. Journal of Chemical Physics **111**, 8454 (1999).

21. Taylor D. P., Goode J. G., Leclaire J. E., Johnson P. M., *"Photoinduced Rydberg Ionization Spectroscopy"*. J Chem Phys **103**, 6293 (1995).

22. Xu H. F., Johnson P. M., Sears T. J., *"Photoinduced rydberg ionization spectroscopy of phenylacetylene: Vibrational assignments of the C-similar to state of the cation"*. Journal of Physical Chemistry A **110**, 7822 (2006).

23. Narayanan K., Chang G. C., Shieh K. C., Tung C. C., *"S-1<-S-0 transition of phenylacetylene: Ab initio and resonant two-photon ionization studies"*. Spectrochimica Acta Part a-Molecular and Biomolecular Spectroscopy **52**, 1703 (1996).

24. Philis J. G., Drougas E., Kosmas A. M., *"The (L-b)S-1 <- S-0 transition of phenylpropyne and phenylacetylene: an experimental and ab initio study"*. Chemical Physics **306**, 253 (2004).

25. Chang C. H., Lopez G., Sears T. J., Johnson P. M., *"Vibronic Analysis of the S(1)-S(0) Transition of Phenylacetylene Using Photoelectron Imaging and Spectral Intensities Derived from Electronic Structure Calculations"*. Journal of Physical Chemistry A **114**, 8262 (2010).

26. Serrano-Andres L., Merchan M., Jablonski M., *"The electronic spectra of aryl olefins: A theoretical study of phenylacetylene"*. J Chem Phys **119**, 4294 (2003).

27. Csaszar A. G., Fogarasi G., Boggs J. E., *"Theoretical Prediction of the Vibrational-Spectrum, Geometry, and Scaled Quantum-Mechanical Force-Field for Phenylacetylene"*. Journal of Physical Chemistry **93**, 7644 (1989).

28. King G. W., Van Putten A. A. G., *"Extended CNDO[complete neglect of differential overlap] calculations upon benzonitrile and ethynylbenzene"*. Journal of Molecular Spectroscopy **42**, (1972).

29. Amatatsu Y., Hasebe Y., *"Ab initio study on phenylacetylene in S-1 and S-2"*. Journal of Physical Chemistry A **107**, 11169 (2003).

30. Amatatsu Y., *" Reaction Coordinate Analysis of the S2-S1 Internal Conversion of Phenylacetylene"*. Journal of Physical Chemistry A **110**, (2006).

31. Hofstein J., Xu H. F., Sears T., Johnson P. M., *"Fate of excited states in jet-cooled aromatic molecules: Bifurcating pathways and very long lived species from the S-1 excitation of phenylacetylene and benzonitrile"*. Journal of Physical Chemistry A **112**, 1195 (2008).

32. Xu H. F., Sears T., Johnson P. M., paper presented at the 61st. OSU International Symposium on Molecular Spectroscopy, The Ohio State University, Columbus, Ohio, 2006.

CHAPTER 2

ELECTRONIC SPECTRUM OF PHENYLACETYLENE (PA): VIBRATIONAL STRUCTURE OF THE $S_1 \leftarrow S_0$ ELECTRONIC BAND

I. Introduction

Three absorption regions at 4.4, 5.2 and 6.4 eV have been observed in the near-ultraviolet vapor absorption of PA[1] **.** Further analysis based on the Franck-Condon principle demonstrated that the molecular geometry of the ground state only slightly changes upon excitation. The lowest energy absorption $S_1 \leftarrow S_0$ (4.4 eV) has been attributed to the benzenoid-type $\pi \rightarrow \pi^*$ transition where the ground state planarity is maintained [2]. The second region (5.2 eV) showed a very diffuse profile at room temperature even with high resolution techniques [2, 3]. However, Leopold et al. [4] reported a more resolved structure with a very strong peak located at 41 955 cm^{-1} (5.2 eV) and a second component at 43 796 cm^{-1} (5.43 eV) for this excitation in a jet-cooled expansion. This result confirmed King and So's results [1]. Moreover, the lack of extended vibrational progressions in Leopold et al.'s spectrum prompted them to suggest that this state also retains the C_{2v} symmetry upon excitation.

The study of the $S_1 \leftarrow S_0$ transition of PA has been motivated by the possible conjugative interaction between the benzene and acetylene fragments. Chia et al. [5] suggested that the π electrons were strongly delocalized over the ring and acetylene components. In the $S_1 \leftarrow S_0$ transition, the electronic configuration can be thought of as a combination of an electron transfer from the next-to-highest occupied molecular orbital (HOMO – 1) to the lowest unoccupied molecular orbital (LUMO) and from the (HOMO) to the (LUMO + 1). Platt [6] developed a model relating those four orbitals that allows to obtain a qualitative description of the most important valence transitions in the spectra of aryl olefins. According to Platt's classification, the

minus combinations of these configurations results in a weak lower energy band with L_b character while the plus combination gives the strong B_b states [6, 7]. In the $S_2 \leftarrow S_0$ transition, an electron is transferred from the highest occupied molecular orbital (HOMO) to the lowest unoccupied molecular orbital (LUMO) leading to a reduction of the π electron density in the excited state, which reduce the force constants in most out-of-plane vibrations and slightly decreases the frequency for the out-of-plane C-H bending vibrations as compared to the in-plane ones [8].

The second vertical electronic absorption computed at the ground state geometry corresponds to the 2 $^1A_1$ excited state also with $\pi \rightarrow \pi^*$ character. The composition of the wave function of this excited state can be basically described by the HOMO$\rightarrow$LUMO configuration that corresponds to a ^1L_a state in Platt's [6] classification. Indeed, this ordering of the lowest excited states (L_b, L_a) has been confirmed with theoretical calculations [2, 7, 9].

The third vertical singlet transition is to the 1 $^1A_2$ state and has been observed at 6.4 eV [2]. It involves a transition from the in-plane π acetylenic orbital to the out-of-plane π^* molecular orbitals.

Low-lying valence triplet states have also been reported experimental and theoretically. Serrano et al. [2] observed the lowest triplet state, 1 $^3A_1$ at 3.57 eV. and labeled it as ^3L_a. This result allowed the identification of the band origin of the triplet state in optical absorption and phosphorescence (3.12 eV) [10, 11] and in electron-energy loss spectroscopy (3.15eV) [10]. Next in energy, the 1 $^3B_2$ (^3L_b) state has been computed vertically at 4.22 eV. and with band origin at 4.08 eV. [2].

In this work, the vibrational structure of the $S_1 \leftarrow S_0$ electronic band of phenylacetylene has been recorded by 1 + 1 REMPI and CRD spectroscopy. Using the 1+1 REMPI scheme, we

selected different intermediate vibrational levels in the S_1 state. To provide more information for vibrational assignments, velocity map imaging photoelectron spectra were also recorded for the resonant ionization process through all the major vibrational features of the spectrum. Analysis of the mode-dependent angular distribution of the photoelectrons was performed to reveal the electron distribution in the benzene ring and substituted group. The rotational temperature was obtained by doing a band contour analysis of the jet-cooled sample. The spectrum includes many resolved vibrational hot-bands leading to new information on the ground state vibrational structure. The vibronic structure of the electronic transition was simulated using a combination of time-dependent density functional theory (TD-DFT) electronic structure codes, Franck-Condon integral calculations, and a second order vibronic model developed previously [12]. Different DFT functionals and basis sets were explored.

II. Experiments

A. Jet-cooled Resonance Enhanced Multiphoton Ionization (REMPI)

1. Background

The response of atoms and molecules to applied electromagnetic (EM) fields has been of great interest in optics. The interaction of matter and light is described by the Schrödinger equation. Although this interaction is linear in the wave function, the response of the wave function to perturbations is not that linear.

For many years, optics successfully described different phenomena assuming linearity. However, with the arrival of the ruby laser [13], the field of non-linear optics arrived. The development of the laser provided a source of intense monochromatic light and permitted the use of non-linear multiphoton processes as a tool in spectroscopy.

Multiphoton absorption and ionization processes are now considered as powerful tools for the study of atomic and molecular systems. Multiphoton ionization (MPI) spectroscopy is now a standard, simple and useful technique for recording electronic spectra [14]. For example, transitions involving an even number of photons in a molecule with a center of symmetry have the selection rule [gerade (g) → gerade (g) or ungerade (u) →ungerade (u)] while the selection rule for transitions with odd number of photons is [g →u] or [u→g]. In the case of two-photon processes, the two-photon inversion symmetry would be the same for both states, the initial and final states, [g →g] or [u →u]. In a three-photon process, the three-photon inversion symmetry would be different for both states, the initial and final states, [g →u] or [u →g] [14, 15]. The increased signal to noise ratio along with extremely high energy and quantum state selectivity available from the high power nano-second pulsed lasers commonly used in multiphoton processes make it a very attractive technique [16].

Multiphoton processes have been applied in both basic and applied research. For example, Vergès et al. [17] successfully employed single and two-photon processes to look at the second excited state of Na_2. Hurst and co-workers [18] selectively ionized each metastable state of He and measured the absolute number of these states using 1+1 resonance ionization spectroscopy (RIS). RIS became popular in the scientific community with most of its applications in analytical chemistry and the detection of single atoms. The scope of multiphoton processes continued to grow as broad views and new applications were identified.

In comparison with non-resonant multiphoton ionization, which can be thought of as proceeding 'resonantly' through a 'virtual state' with a very short lifetime, resonantly enhanced ionization takes place via a real level which has a much longer lifetime than the virtual state and therefore the ionization rate is greatly enhanced [16].

In general, one-color REMPI is very simple to implement. However, using a second color is preferable in certain cases. Clearly, if the first excited state lies lower than half of the ionization energy the excitation photon will not have enough energy to ionize the molecule with absorption of only one more photon. Fig. 2.1 shows two different REMPI schemes.

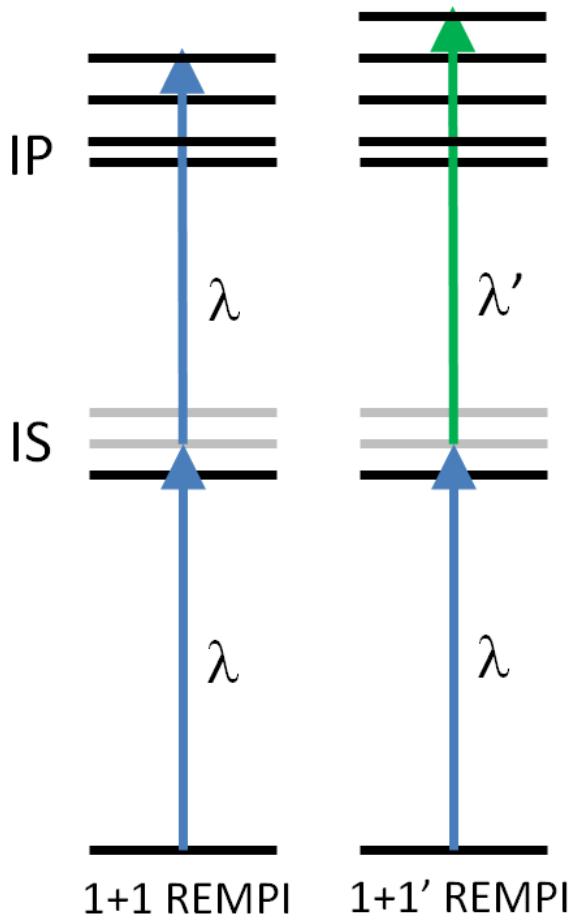

Figure 2.1: REMPI schemes for one-color REMPI (1+1 REMPI) and two-color REMPI (1+1' REMPI). IP is the ionization potential and IS the intermediate or Rydberg state.

The signal levels obtained by REMPI can be significantly improved with a careful design of the ion-extraction optics. One example is the pulsed-laser ionization scheme where the ion formation is constrained to occur over a very limited spatial region and coupled with high efficiency to a TOF mass analyzer and using a pulsed gas inlet impose an additional spatial constraint. In this case, the optimum location exists downstream from the pulsed nozzle where the internal molecular temperature will have reached a minimum, while the local gas density remains relatively high. Ionization at this location yields the optimum optical spectroscopic selectivity with the maximum ion signal level. Because the optimum ionization region is located only a few centimeters from the exit nozzle, the ion optics have to be designed carefully to include the influence of the pulsed valve on the extraction fields.

Supersonic jet cooled-REMPI is one of the superior ionization methods for the spectroscopic analysis of cyclic aromatics. This method has ultra-high sensitivity and selectivity of molecules in ionization detection by simply fixing the wavelength of the laser to a well-resolved transition.

As shown in Fig. 2.2, the 1+1 REMPI scheme has allowed us to select different intermediate vibrational levels in the S_1 state. More information for vibrational assignments was obtained using velocity map imaging photoelectron spectroscopy by recording the spectrum for the resonant ionization process through all the major vibrational features.

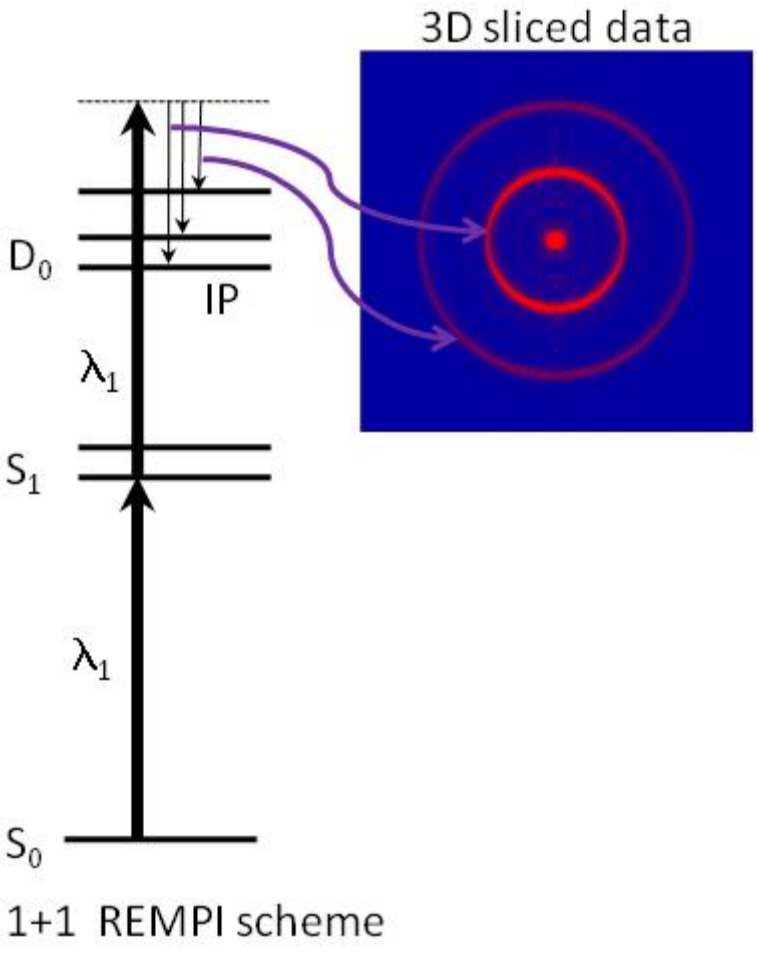

Figure 2.2: 1+1 REMPI scheme accompanied by velocity map imaging photoelectron spectroscopy. IP is the ionization potential and D_0 is the cation ground state.

2. Experimental Setup

Phenylacetylene (PA, 98%) purchased from Aldrich was used without any purification, while the experimental apparatus used for this study has been previously described [19] except for recent modifications of the ion optics for velocity map-imaging. The sample, with He as a carrier gas, was supersonically expanded through a pulsed valve (300 μm orifice diameter General Valve, Parker Corp.) running at 10 Hz. The Helium backing pressure was optimized at roughly 200 torr by optimizing the quality of the electron imaging and ensuring the absence of dimers in the TOF mass spectrum. After collimation by the skimmer with 3 mm diameter, the PA-seeded beam enters the interaction region midway between the repeller and extractor plates**.**

The ion optics setup is derived from that of Townsend et al. [20] and only mentioned briefly here. It consists of four electrode plates with inner diameter 3, 5, 10, and 15 mm. The outer diameters of these plates are 45 mm, and 1 mm thickness. Before the experiment, the electric field's flatness and focusing condition were simulated by Simion software and the resolution was limited by the pixel number. The voltage for these plates, were provided by a high voltage power supply, divided by a series of resistors to power the various electrodes. The whole ion optics and field-free time-of-flight (TOF) region was shielded by a $\mu-$metal tube, so as to avoid any distortion from background residual magnetic fields. The detector includes 75 mm chevron-type micro-channel plates (MCP, Photonis USA, INC.), a phosphor, and a video camera (XC-ST50, Sony).

A pulsed Quantel Nd:YAG laser (YG580, Quantel) was used to pump the dye laser. The output of the dye laser was doubled in a BBO crystal housed in an Inrad autotracker, and directed into the detection chamber in the oppose direction to the molecular beam. The resulting ions were projected onto the MCP detector; the fluorescence from the phosphor was captured by the

camera, and then transferred to a PC for storage and further analysis. Calibration of the fundamental wavelength was done with a wavemeter (WaveMaster, Coherent). The time sequence of the pulsed valve, laser system and camera was controlled by delay generators (DG535, Stanford Research System) and PC mounted timer cards. The data collection was programmed by LabVIEW software, using a National Instruments frame grabber.

The spectrum shown in Fig. 2.3 was recorded using a dye laser and several different dyes making complete accuracy impossible. In fact, the trace is a composite of overlapping spectra from several dyes, for each of which the dye laser changes in intensity and mode structure as it is scanned, having effects on intensities. The spectra from adjacent individual dyes were scaled by making a band appearing in both spectra have the same intensity before the spectra were spliced. However, intensities also vary across a dye range, and the splicing is therefore not necessarily a uniquely defined process.

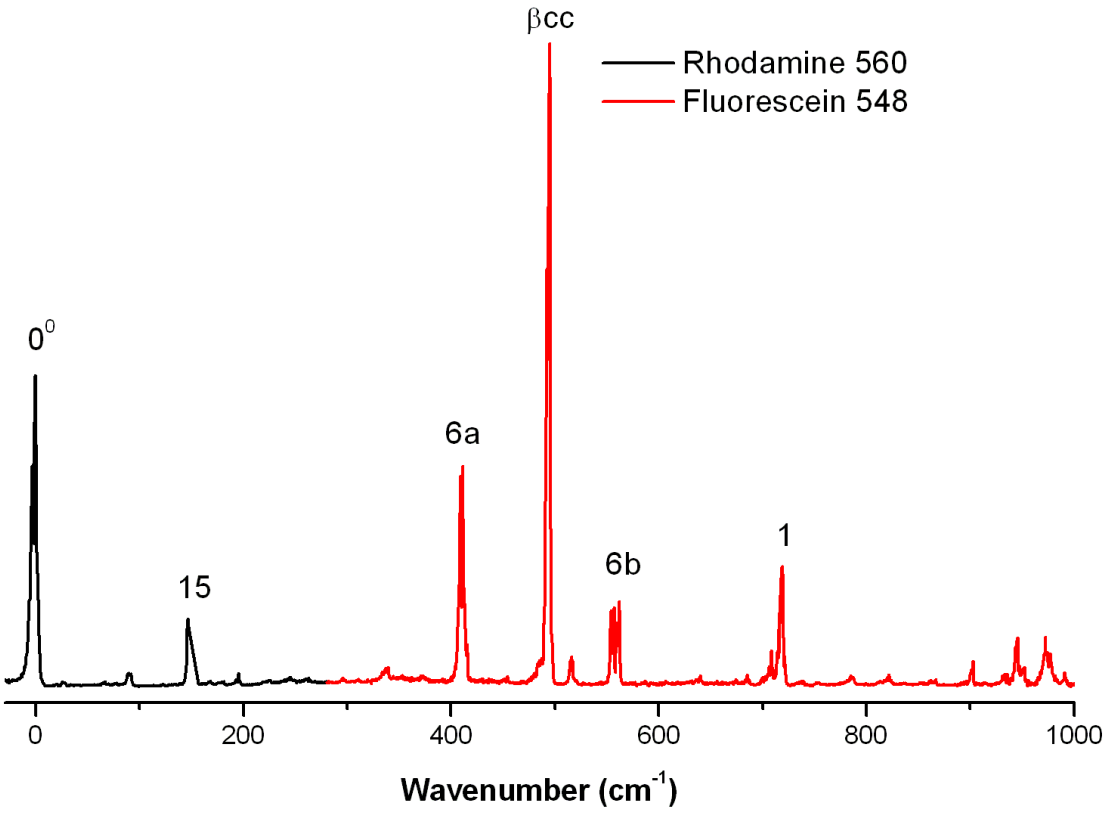

Figure 2.3: Section of the 1+1 REMPI spectrum that resulted from overlapping spectra obtained with two different dyes: Rhodamine 560 (λ range 541-583 nm, peak at 563 nm), Fluorescein 548 (λ range 540-576 nm, peak at 548 nm).

The REMPI photoelectron images were recorded while scanning a dye laser over the S_1 transition. The sensitivity of the method makes it possible to record PE spectra continuously while scanning the laser over the transition, providing a 2D spectrum shown in Fig. 2.6. The REMPI spectrum is then obtained by integrating the photoelectron imaging data set collected for each wavelength. However, for more detailed analyses of the photoelectron images, the laser was reduced in power and tuned to the center of a vibrational line, collecting roughly 5000 shots per image. Space charge effects were thereby minimized. A representative sample of photoelectron spectra from S_1 REMPI is shown in Fig. 2.5. The analysis of the photoelectron images was performed with the pBASEX [21] based on BASEX, a program developed by Dribinski et al.[22]. To display the photoelectron spectra, the radial coordinates of the images were converted to kinetic energy, integrated over the angular coordinate and corrected with a Jacobian factor.

The raw photoelectron image is a 2D image which contains the entirety of the 3D photoelectron distribution, as shown in Fig. 2.4. In order to obtain the PE spectrum from the raw image, it must be reconstructed to yield the central slice of the original 3D distribution. This step is often the drawback of imaging experiments, as the methods of this reconstruction have not yet been perfected [23]. Experimental techniques have been developed in ion imaging experiments where only the central part of the 3D distribution is imaged (slicing) [20, 24], but those methods are not applicable to PE imaging. Therefore, analytical methods to transform the image are necessary for the PE experiments. Numerous methods to that end have been developed, such as Abel inversion, "onion-peeling", back-projection, the Fourier-Hankel technique, basis set expansion (BASEX) and pBASEX methods [21-23].

The Abel inversion method is one of the most commonly used method for image transformation [22, 23]. This numerical method reconstructs the image pixel by pixel. The

forward Abel transformation projects a function with an axis of symmetry, f(r), and produces the projection that is one dimension lower, g(R), such that [21]

$$g(R) = 2\int_{R}^{\infty} \frac{f(r)rdr}{\sqrt{(r^2 - R^2)}} \quad \ldots(2.1)$$

The inverse of the Abel transformation is then capable of reconstructing the f(r) function from g(R) according to [21]:

$$f(r) = -\frac{1}{\pi}\int_{r}^{\infty} \frac{g'(R)dR}{\sqrt{(R^2 - r^2)}} \quad \ldots(2.2)$$

The Fourier-Hankel technique is based on a representation of the inverse Abel transform [22]. It is a fast technique that produces high quality images. However, this method magnifies experimental noise and generates artificial structures during the image reconstruction. In the "onion-peeling" method, the noise in the reconstructed image increases towards the center meaning that it does not handle noisy images well. The back-projection method introduced by Sato et al. [25] reduced experimental noise by filtering in the frequency domain while increasing the potential loss of information. Bordas et al. [26] developed an alternative version of the back-projection method that was too complicated, specific and time-consuming for routine applications.

BASEX, a more efficient and computationally cheap method, was developed by Dribisnki et al. [22]. This method uses basis functions to reconstruct the image and similarly to the Abel inversion method, it assumes a cylindrical symmetry which is the case of most photoelectron imaging experiments [23]. The forward Abel transformation, in this case expressed in cylindrical coordinates, is expressed as [21]

$$P(x,z) = 2\int_{|x|}^{\infty} \frac{rI(r,z)dr}{\sqrt{r^2 - x^2}} \quad \ldots(2.3)$$

where P(x,z) is the 2D projection on the detector (x,z) plane and I(r,z) represents the 3D image. The projection is the raw image in imaging experiments [23]. Thus, the projection is

$$P_{ij} = 2\int h(x - x_i, z - z_i)dxdz \int_{|xi|}^{\infty} \frac{rI(r,z)dr}{\sqrt{(r^2 - x^2)}} \quad \ldots(2.4)$$

where h(x,z) is a instrumental function. BASEX represents the original 3D distribution as an expansion of a well-behaved basis set in the (r,z) space and generates the basis in the projection space using the equation above [22, 23].

Similarly to BASEX, pBASEX instead uses basis functions in polar coordinates confining the transformation noise to the central spot instead of the center line. This method converts the Cartesian raw image to polar coordinates before transformation, meaning that any noise is removed before the inversion is done [21, 23].

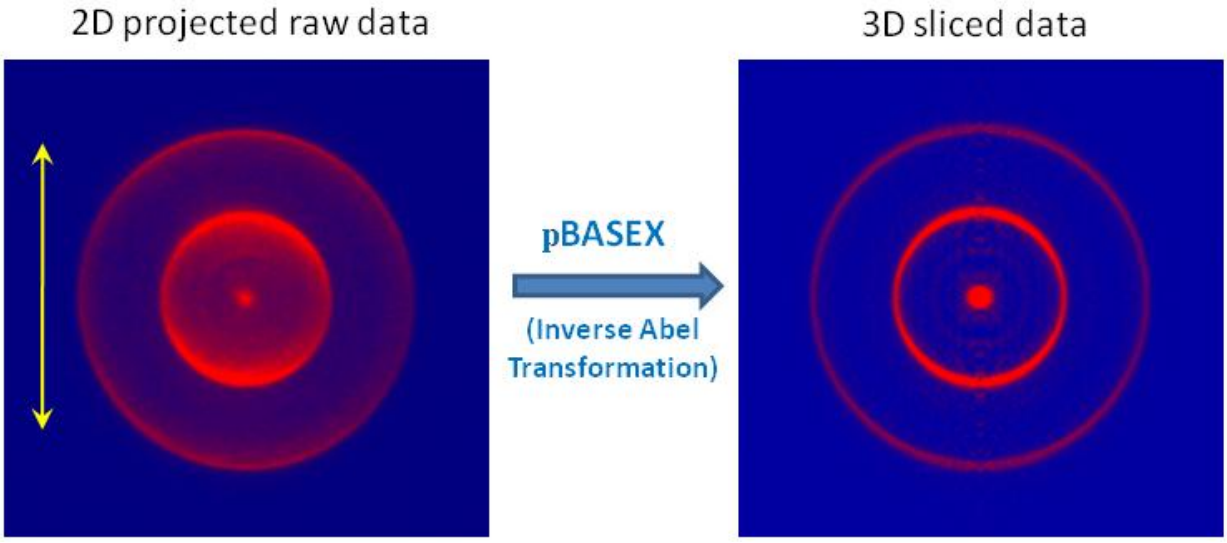

Figure 2.4: (Left) 2D projected raw data. (Right) 3D sliced data after analysis of the plot on the left with pBASEX. (yellow arrow) Laser polarization axis.

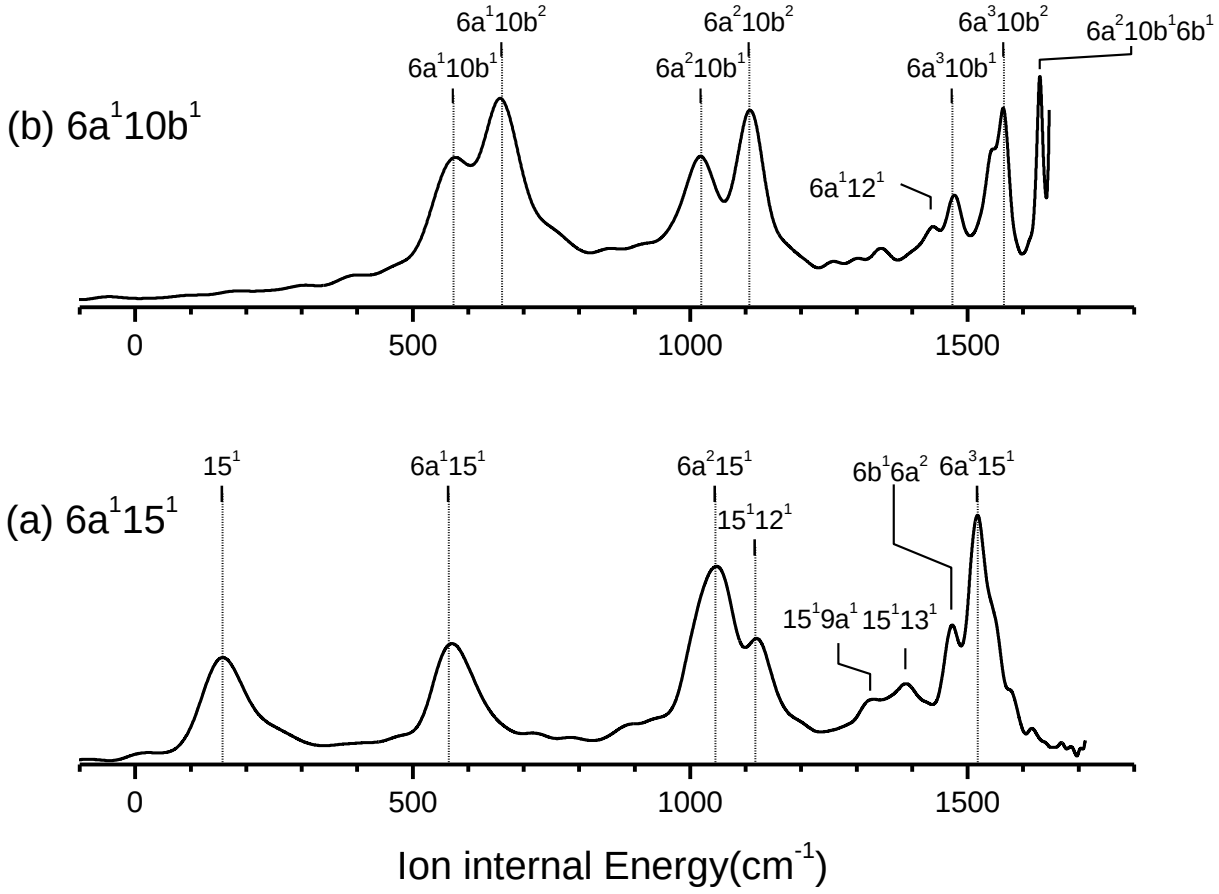

Figure 2.5: Part of the two-photon transition resonance photo-electron spectra via different vibrational states of S_1 PA. Vibrational labels are at the left of each trace while the suggested ionic vibrational assignments are at the top.

The angular distribution of electrons from a 1+1 REMPI scheme is described by [27]:

$$I(\theta) = 1 + \beta_2 \cdot P_2(\cos\theta) + \beta_4 \cdot P_4(\cos\theta) \quad \ldots(2.5)$$

In this case, the β_4 parameter, as compared to the variance in the fitting process, played a minor or very insignificant effect in the angular distribution and was constrained to zero in the final fitting process. Based on the assumption of a one photon process, the limiting values of the β_2 anisotropic parameters are $-1 \le \beta_2 \le 2$, indicating the angular distributions of the fragments in the laboratory space are perpendicular and parallel to the polarization of excitation laser field, respectively. If the fitting parameter is close to zero it means the distribution tends to be isotropic. As shown in Table 2.1, most of the values of the anisotropic parameter (β_2) range from 0.2 to 0.7 in this study, indicating weak anisotropy. The more anisotropic patterns in general occurred for higher energy electrons and for those resulting from excitation of a 6a containing mode in S_1 (shown in Fig. 2.6), but the results were not consistent enough for anisotropy to be used as a tool for state assignments.

Table 2.1: Anisotropic parameters from the fitting of the photoelectron angular distribution for each ion vibrational state, via different intermediate states. Ion energies for each ion vibrational state are also included.

$D_0(b_1)$*			$S_1(b_2)$*							
StateLabel	Symm.	E_{ion}/cm^{-1}	0	15^1	$10b^2$	$6a^1$	βCC^1	βCH^1	$6b^1$	1^1
			a_1	b_2	a_1	a_1	b_2	b_2	b_2	a_1
0	a_1	0	0.46			0.24[a]				
15^1	b_2	152						0.23	0.10	
$10b^2$	a_1	223			0.45					
15^110b^1	a_2	257		0.45						
$6a^1$	a_1	453	0.79			0.20[a]				
βCC^1	b_2	480					0.22			
$6b^1$	b_2	568						0.27	0.17	
$15^1\beta CC^1$	a_1	648		0.62						
$10b^26a^1$	a_1	685			0.53					
1^1	a_1	757				0.36				0.24
$6a^2$	a_1	910				0.57[a]				
$6b^116a^1$	a_1	913							0.30	
βCC^16a^1	b_2	939					0.27			
1^110b^2	a_1	976				0.14				
$6b^16a^1$	b_2	1034						0.55	0.35	
$6b^2$	a_1	1117						0.00	0.12	
$6a^215^2$	a_1	1185				0.60				
1^16a^1	a_1	1216								0.24
$1^1\beta CC$	b_2	1245				0.47	0.26			
βCH^2	a_1	1322						0.38	0.29	
$6a^3$	a_1	1375				0.73[a]				
βCC^16a^2	b_2	1407					0.49			
1^2	a_1	1514								0.20
$6b^112^1$	b_2	1527						0.38	0.31	
1^112^1	a_1	1734								0.26
1^26a^1	a_1	1940								0.53

* S_1: First singlet excited state, D_0: Cation ground state.
a. See Fig. 2.6

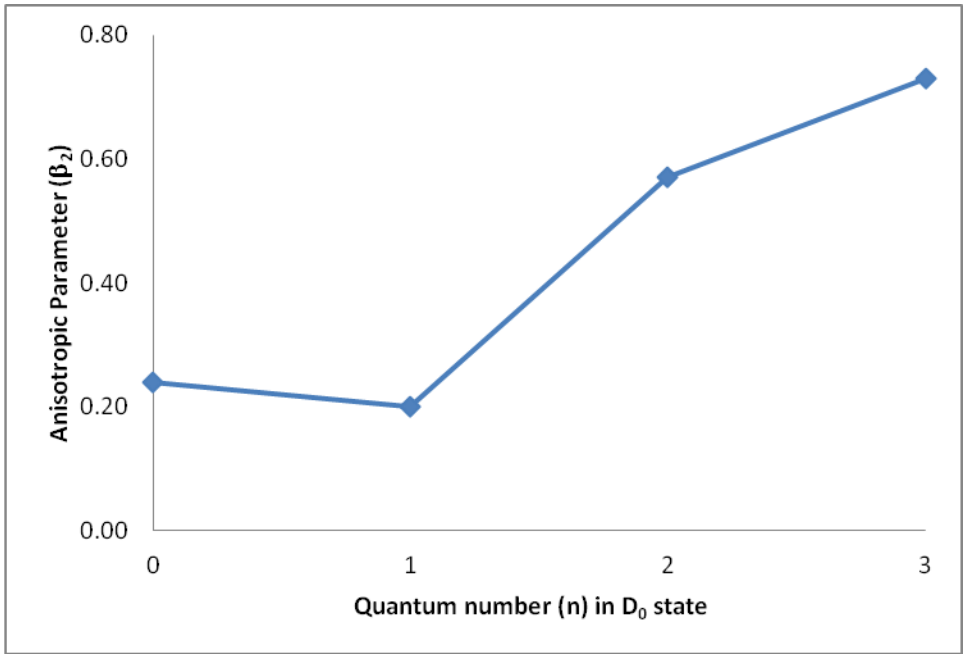

Figure 2.6: Angular distribution of the electron ionized via the 6a vibration mode at different quantum numbers in the D_0 state from Table 2.1.

3. Results and Discussions

All vibrational analysises of the S_1 spectrum of PA have been built upon the fundamental work of King and So [28, 29] who analyzed the room temperature absorption spectrum using isotopic substitution and band contour analysis. In the present study a requirement of consistency with both the vibrational structure in the photoelectron spectra and the intensities in the vibronic calculations enables a more extensive and reliable assignment of the vibrational transitions in the S_1 spectrum. 1 + 1 REMPI spectrum of PA in the range of 0-2000 cm^{-1} in Fig. 2.7, some assignments of vibrational levels in the S_1 state are also shown.

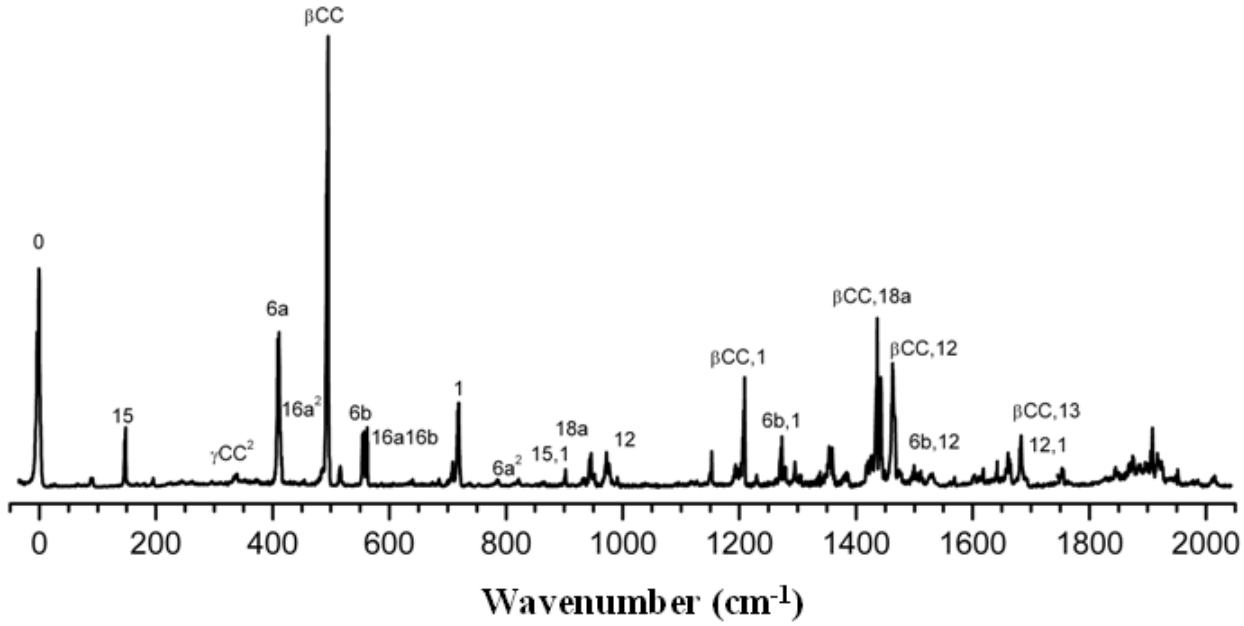

Figure 2.7: 1 + 1 REMPI spectrum of PA resonant with the S_1 state with the assignment of some vibrational levels.

Due to the low density of states, most assignments of the vibrational levels at low excitation energy are clear and unambiguous. As the excitation energy increases, more congestion appears, and in many cases it is impossible to clearly assign the features without ambiguity using only theoretical frequencies. The vibrations below 2000 cm^{-1} are all various types of CC stretching, CC bending, and ring deformation modes and their overtones and combinations. The point group of PA is C_{2V}, and there are totally 36 nondegenerate normal modes, 13 of which belong to a_1 symmetry, 3 to a_2, 8 to b_1, and 12 to b_2. The S_1 state has an electronic symmetry of B_2, resulting in $S_1 \leftarrow S_0$ having allowed transitions from the S_0 origin to a_1, a_2, and b_2 vibrations of S_1 in C_{2v}. The transition to S_1 is allowed but weak as discussed previously because it derives from the forbidden $^1B_{2u}$ state of benzene. It can gain intensity by coupling to nearby strongly allowed A_1 and B_2 states through b_2 and a_1 vibrations. The vibrations in benzene-like aromatic compounds have been described by using two conventional labeling schemes, Wilson's [30, 31] and Herzberg's [32-34]. Wilson's notation tends to be more consistent between states of the molecule and between the different substituted benzenes and has been adopted in this work. The vibrational modes and symmetries for S_1 are summarized in Table 2.2, many of them were used as the resonance intermediate levels in the photoelectron imaging experiment.

Table 2.2: 1+1 REMPI relative Intensities for the assigned vibrational features (modes) of the $S_1 \leftarrow S_0$ Transition of PA.

Freq (cm^{-1})	mode	Symm.	Exp. Intensity	Freq (cm^{-1})	mode	Symm.	Exp. Intensity
0	0		2030	1152	$9b^1$	b_2	190
97	$10b^1$	b_1	90	1193	13^1	a_1	150
146	15^1	b_2	490	1208	$\beta CC^1 1^1$	b_2	680
168	γCC^1	b_1	70	1229	$6a^3$	a_1	80
194	$10b^2$	a_1	70	1271	$6b^1 1^1$	b_2	350
225	$16a^1$	a_2	40	1296	3^1	b_2	150
245	$10b^1 15^1$	a_2	60	1352	$6a^1 12^1$	a_1	260
295	$10b^3$	b_1	50	138	$6a^1 18a^1$	a_1	120
310	γCC^2	a_1	50	1426	1^2	a_1	300
337	$10b^2 15^1$	b_2	120	1436	$\beta CC^1 12^1$	b_2	1050
373	$\gamma CC^1 16a^1$	b_2	70	1442	$19b^1$	b_2	800
409	$6a^1$	a_1	1380	1463	$\beta CC^1 18a^1$	b_2	1050
445	$16a^2$	a_1	60	1500	$6b^1 12^1$	b_2	160
493	βCC^1	b_2	3940	1530	$6b^1 18a^1$	b_2	110
516	$10b^1 6a^1$	b_1	18	1569	$9b^1 6a^1$	b_2	70
555	$15^1 6a^1$	b_2	470	1603	$13^1 6a^1$	a_1	110
561	$6b^1$	b_2	470	1618	$\beta CC^1 6a^1 1^1$	b_2	130
639	$\beta CC^1 15^1$	a_1	60	1641	$8b^1$	b_2	150
684	$\beta CC^1 10b^2$	b_2	70	1660	$1^1 12^1$	a_1	250
707	$6b^1 15^1$	a_1	180	1682	$\beta CC^1 13^1$	b_2	410
719	1^1	a_1	760	1754	$13^1 6b^1$	b_2	80
753	$6b^1 10b^2$	b_2	20	1845	$9a^1 1^1$	a_1	40
786	βCC^1 γCC^2	b_2	70	1869	$9b^1 1^1$	b_2	50
821	$6a^2$	a_1	70	1874	$\beta CC^1 6a^1 18a^1$	b_2	70
865	$15^1 1^1$	b_2	40	1885	12^2	a_1	50
902	$\beta CC^1 6a^1$	b_2	110	1908	$13^1 1^1$	a_1	100
945	12^1	a_1	290	1916	$\beta CC^1 1^2$	b_2	70
954	$18a^1$	a_1	260	1924	$18a^1 12^1$	a_1	50
990	$18b^1$	b_2	70	195	$18a^2$	a_1	30
1096	$15^1 12^1$	b_2	40	2013	$3^1 1^1$	a_1	20
1119	$18a^1 15^1$	b_2	50				
1126	$9a^1$	a_1	50				

The electronic origin of the S_1 state in this work was measured to be 35 875 cm^{-1}, close to the 35 877.18 cm^{-1} determined by Ribblett et al.[35] in their high-resolution rotationally resolved spectrum. This difference is reasonable because here the rotational structure is not resolved and the position of the peak intensity is reported, corresponding to a band head, not the actual band origin.

The vibrational modes involved in the transitions below 800 cm^{-1} are dominated by the modes 15, 6a, βCC, 6b, and 1, with vibrational energies 147, 409, 494, 561, and 719 cm^{-1}, respectively. Most strong transitions involving these modes have been assigned in previous studies, and they need not be discussed further. The symbol β indicates in-plane oscillation of the atoms in the acetylene group, and βCC primarily involves motion of the carbon nearest the ring. This vibration has the most vibronic intensity and thus shows most strongly in the spectrum.

The lower intensity bands are much more of a challenge to our understanding and modeling, and Fig. 2.8 shows an expanded version of the experimental spectrum so the weak bands can be seen. For the upper, lower energy trace the vertical axis is expanded by a factor of 10, and for the higher energy portion of the spectrum the scale is expanded 3-fold.

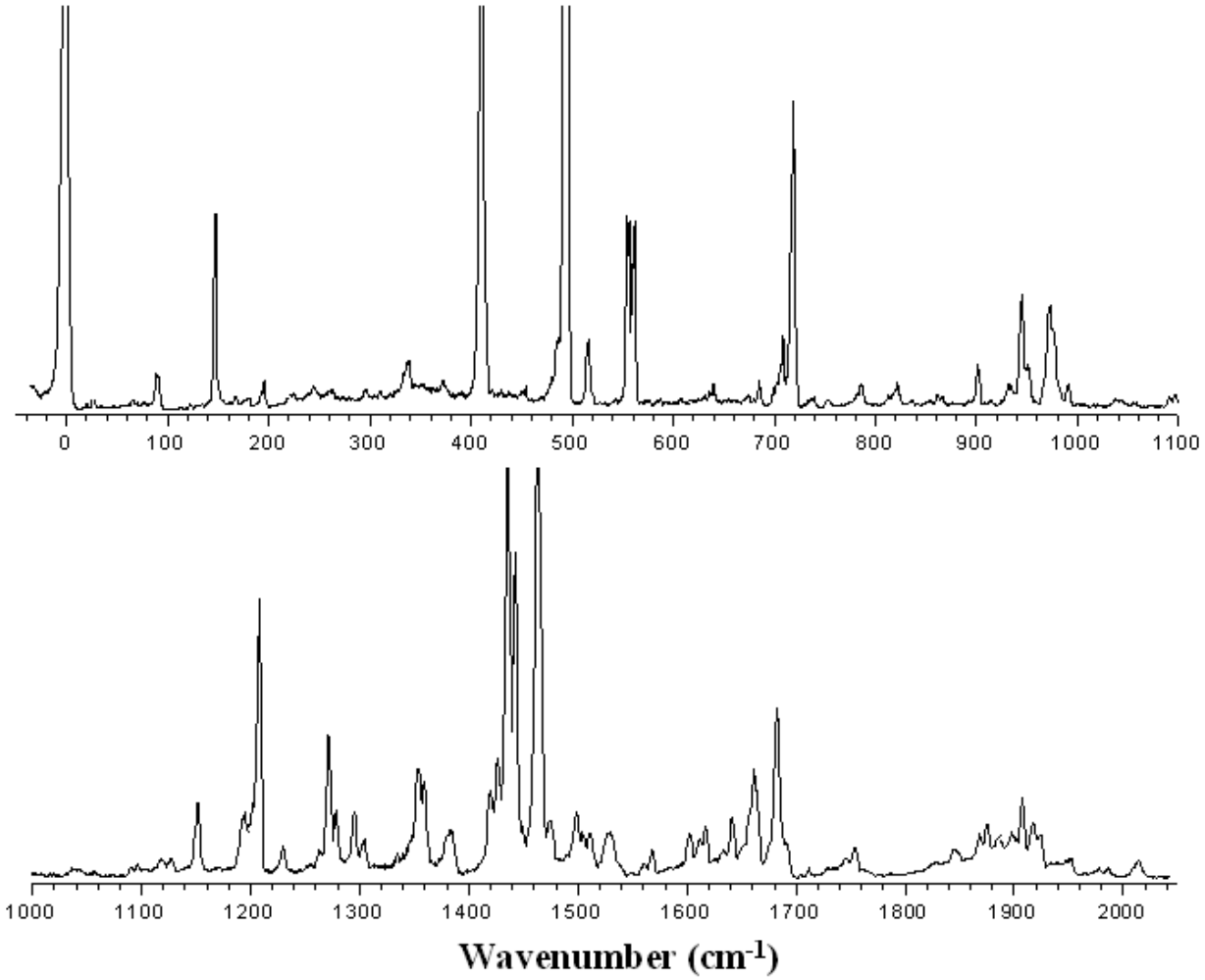

Figure 2.8: Spectrum of the S_1–S_0 transition expanded to show weak transitions in the fundamental region (upper panel) where the bands can be clearly assigned, and a more complicated higher energy part (lower panel).

One of the more interesting weak bands in the lower part of the spectrum is the first one seen with significant intensity at 97 cm^{-1}. This fundamental frequency was ascribed to the 10b vibration by Narayanan et al. [8] by virtue of their vibrational calculations and the appearance of the $10b^2$ band in the spectrum. The problem with its appearance as $10b^1$ in the REMPI spectrum is that its symmetry is b_1, so it should be forbidden even vibronically. This vibration is an out-of-plane acetylene-phenyl bend, so it should participate in torsional motion in company with mode 15, the in-plane bend. Coriolis coupling calculations, reported by Chang et al. [27], make it clear that the appearance of $10b^1$ is primarily made possible by its borrowing intensity from this nearby mode, and its appearance in several combination bands arises from the same effect. 10b also shows a broadened rotational contour consistent with its Coriolis origins. However, the intensity of the 10b band is apparently still too large relative to the 15 band intensity to be explained by the calculated coefficient. Whether this is due to nonlinearities in the multiphoton ionization process and detection or deficiencies in the calculations is not presently clear.

One set of low-energy bands with significant intensity seem to still be in question. Two closely spaced transitions are clearly observed at 555 and 561 cm^{-1}. Powers et al. [36] assigned the lower peak to βCH and the upper one to 6b, both b_2 vibrations (they stated that they followed King and So [3] but the latter never reported a βCH band for protonated PA). However, Narayanan et al. [8] assigned the lower transition to 6b and the upper to mode 4, a b_1 vibration. Various theoretical calculations, including our own, indicate that one of the peaks must be the 6b mode, but indicate the energy for the βCH mode is in the 700-800 cm^{-1} region, making it a less likely candidate. As for mode 4, a $b_1$vibration is unlikely to be as strong as the observed feature, since it would have to be induced by Coriolis coupling calculated to be at least an order of magnitude smaller than that of the weak 10b transition [27].

Photoelectron images enabled checking some of assignments for consistency with the vibrational structures of the cation. The upper panel in Fig 2.9 shows the sliced 3D Abel transform images for different vibrational modes of PA cation and the lower the ion internal energy of PA cation via different vibration energy levels in the S_1 state. Table 2.2 gives the vibrational levels and frequencies of PA cation in the $^2B_1$ ground state. In the PES spectrum shown in Fig. 2.6a, a series of combination bands involving 15 and 6a modes as well as the 15 mode alone are observed. On the basis of the propensity rule of ionization, if the intermediate level were the βCH mode, then the ionization would result in a series of excitations of the βCH mode in the cation state, but they are not seen in the photoelectron data. From the theoretical vibronic calculations that will be described more in detail in section III of this chapter, the intensity for the $6a^115^1$ (b_2) level should be non-negligible, and 555 cm^{-1} is the sum of the experimental values observed for the components. The $6a^115^1$ combination band is therefore believed to be the corresponding S_1 mode at 555 cm^{-1}, gaining intensity by Fermi resonance with the nearby 6b state at 561 cm^{-1}.

A moderate peak at 515 cm^{-1} not previously reported also requires further consideration. The simulation spectrum (including only the symmetry-allowed transitions) does not show this peak. From vibrational energies this peak could be assigned to either $6a^110b^1$ (b_1, 506 cm^{-1}) or $10b^2\gamma CC^2$ (a_1, 504 cm^{-1}). The choice of $10b^2\gamma CC^2$ would be favored by considerations of symmetry, but in the photoelectron imaging spectrum shown in Fig. 2.5b we observed the series $10b_16a^n$ and $10b_26a^n$ (n: vibrational quantum number in the cation state), with no significant sign of an excitation of the γCC mode in the cation state. This then appears to be another case where the 10b mode is acquiring intensity by Coriolis coupling. A similar unexpected combination, $10b^11^1$, appears at 821 cm^{-1}.

When the intensity scale is expanded in the REMPI spectrum, there appear many weak transitions in the region of 150-400 cm^{-1}. Fundamental bands or combination bands of the low frequency modes are possible, including 10b (97 cm^{-1}), 15 (147 cm^{-1}), γCC (155 cm^{-1}), 16a (224 cm^{-1}), and 16b (277 cm^{-1}). It is also possible that some peaks may be due to hot bands, some of which involve torsional motion of the acetylene moiety. With much less confidence because the transitions are so weak, we have assigned most of these peaks and listed them in Table 2.2. Moreover, Table 2.4 gives these band positions with their relatives intensities and compare them with the ones obtained in a previous study using 1+1 REMPI [27].

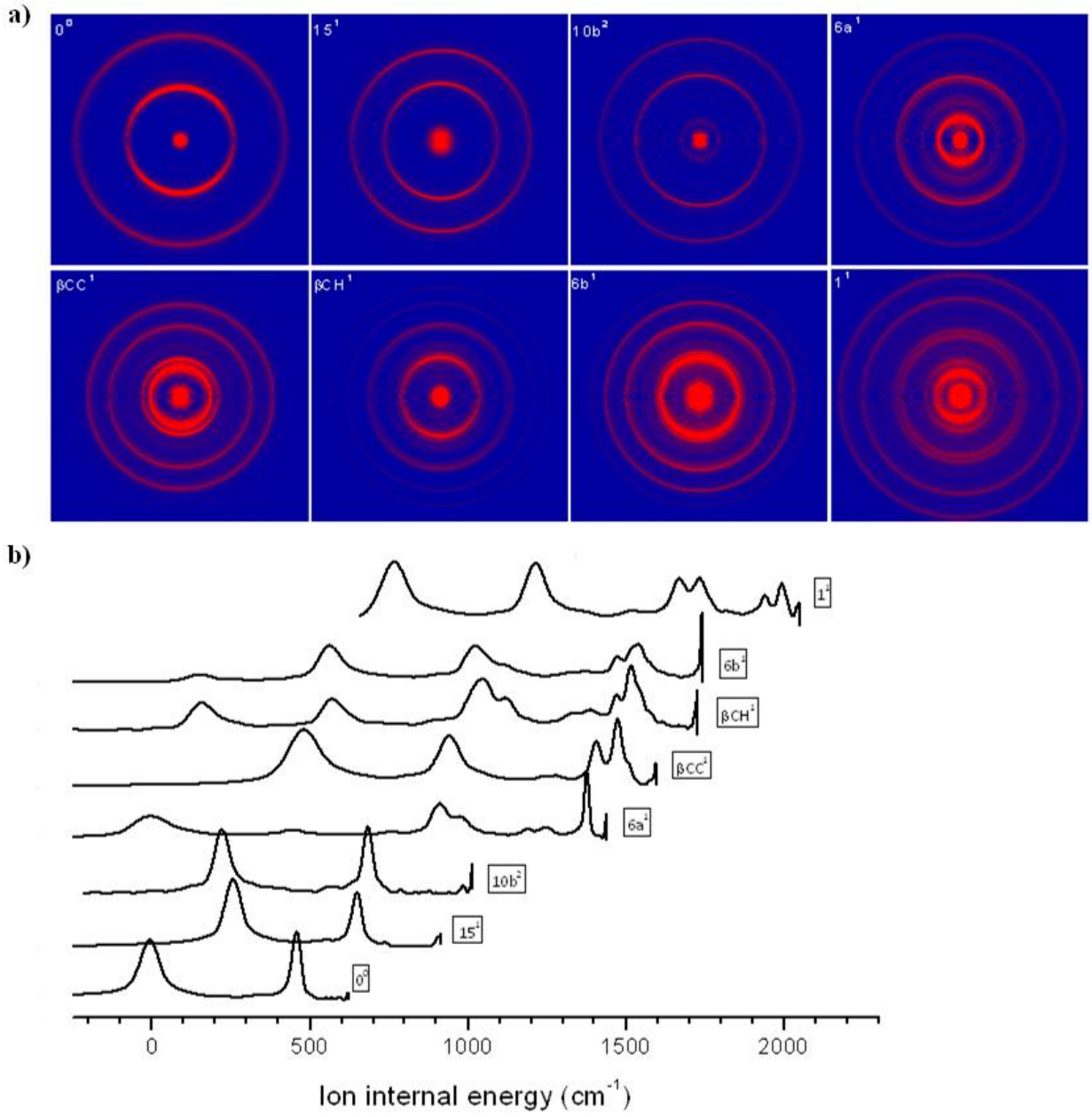

Figure 2.9: a) Sliced 3D Abel transform images for different vibrational modes of PA cation. b) Ion internal energy of PA cation via different vibration energy levels in the S_1 state.

Table 2.3: Vibrational levels and frequencies of PA cation in the $^2B_1$ ground state.

Vibrational mode	This work[a]	Kwon et al. [37]	Lin and Tzeng [38]	Dyke et al. [39]
15^1	152	143		
$10b^2$	223	221		
$15^1 10b^1$	257			
$16a^1$	346	346		
$6a^1$	453	458	439	460
βCC^1	480	499		
$6b^1$	568	561	560	
$15^1 \beta CC^1$	648			
$6a^1 10b^2$	685			
1^1	757	747		759
$6a^2$	910	914	921	
$6a^1 \beta CC^1$	939			
$1^1 10b^2$	976			
$6a^1 6b^1$	1034			
$6b^2$	1117			
$6a^2 15^2$	1185			
$1^1 6a^1$	1216	1205		
$1^1 \beta CC^1$	1245			
$10a^1 \beta CC^1$	1287			
βCH^2	1322			
$6a^3$	1375	1370	1372	
$6a^2 \beta CC^1$	1407			
$12^1 \beta CC^1$	1473	1465		
1^2	1514			
$6b^1 12^1$	1527			
$1^1 6a^2$	1668			
$1^1 12^1$	1734			
$1^2 6a^1$	1940			

[a] Energy level derived from the photoelectron imaging and the uncertainty is estimated 15 cm^{-1}.

Table 2.4: Comparison between our 1+1 REMPI results for the fundamental vibrational frequencies of PA in the S_1 state and other references.

Symmetry	Mulliken	Wilson[a]	Present Expt.	King and So[b]	Chia and Goodma	Mode Description[c]
a_1	ν_1	νCH				C_8H_8 stretch
	ν_2	2				CH stretch
	ν_3	20*a*				CH stretch
	ν_4	7*a*				CH stretch
	ν_5	νCC		2061		$C_7{\equiv}C_8$ stretch
	ν_6	8*a*				CCH bend
	ν_7	19*a*	1419			CCH bend
	ν_8	13	1191	1191	1200	C_1C_7 stretch, CCH bend
	ν_9	9*a*	1126	1057		CCH bend
	ν_{10}	18*a*	954	951	954	Ring deformation
	ν_{11}	12	945	944	944	Ring deformation
	ν_{12}	1	719	717	722	Ring breath
	ν_{13}	6*a*	409	409	409	$C_7C_8H_8$-ring breath
a_2	ν_{14}	17*a*		728		OP CCH-ring breath
	ν_{15}	10*a*		656		OP CCH bend
	ν_{16}	16*a*	224	220		OP CCH bend
b_1	ν_{17}	5		731		OP CCH bend
	ν_{18}	17*b*		710		OP CCH bend
	ν_{19}	11		586		OP CCH bend
	ν_{20}	4		470		OP CCH bend
	ν_{21}	γCH				OP ring deformation
	ν_{22}	16*b*		362		OP ring def, $C_7C_8H_8$
	ν_{23}	γCC	168			OP ring def, $C_7C_8H_8$
	ν_{24}	10*b*	97	163		OP ring def, $C_7C_8H_8$
b_2	ν_{25}	7*b*				CH stretch
	ν_{26}	20*b*		3079		CH stretch
	ν_{27}	8*b*	1642			Ring deformation
	ν_{28}	19*b*	1442			Ring deformation
	ν_{29}	14			1575	CCH bend
	ν_{30}	3	1296			CCH bend
	ν_{31}	9*b*	1152	1075		CCH bend
	ν_{32}	18*b*	990	972		CCH bend
	ν_{33}	βCH				$C_7C_8H_8$ bend
	ν_{34}	6*b*	561	560		Ring deformation
	ν_{35}	βCC	493	492		$C_1C_7C_8$ bend
	ν_{36}	15	146	322		CCH, $C_7C_8H_8$ bend

[a.] The symbol ν indicates a stretch, β means an in-plane bend, and γ means an out-of-plane bend [30].
[b.] G. W. King and S. P. So.[1]; C. L. Chia and L. Goodman [5].
[c.] Serrano-Andres et.al. [2]. The descriptions are the main contributions to the normal modes. The acetylene carbons are 7 and 8, C_7 is attached to the ring at C_1, while a lack of atom numbering indicates the H or C belongs to the phenyl ring.

In the 600-1000 cm^{-1} region, the weaker peaks can also be completely assigned. Very weak peaks at 639, 684, 707, 739, 753, 786, 821, and 865 cm^{-1} are $10a^1$, $10b^2\beta CC^1$, $6b^115^1$, $10a^110b^1$, $6a^2$, 1^110b^1, and 1^115^1 levels, respectively. The peaks at 902, 945, 970, and 990 cm^{-1} are $6a^1\beta CC^1$, $18a^1$, 12^1, and $18b^1$, respectively. The ordering of the equal-intensity $18a^1$ and 12^1 bands is somewhat arbitrary. Calculations put the lower energy as ν_{12}, so we have followed that lead, but they are probably strongly mixed by Fermi resonance, so there is unlikely to be much meaning to that choice.

With increasing excitation energy, the features of the spectrum display more complications that do not allow the facile assignment of transitions using only symmetry arguments and vibrational energies. Even for a single peak, there are often multiple choices of vibrational levels that could be associated with this transition, but with the help of vibronic intensities, most candidates can be eliminated. The assignments in Table 2.4 list the strongest calculated transition near the energy of the peak in question, using experimentally assigned mode frequencies. Several weak shoulders were not assigned since Fermi resonance would render the intensities unreliable as an indicator of the mode assignment. Also, photoelectron images were not recorded in the upper energy region as line overlaps make them difficult to interpret.

4. Conclusions

For some isolated lines, photoelectron imaging spectroscopy gave some valuable additional information to aid in assignments. There are some indications of nonlinearities in the resonance ionization process, in that some of the weak lines show up with unexpected strength.

B. Cavity Ringdown (CRD) Spectroscopy

1. Background

Absorption spectroscopy is a very important analytical technique in science. Optical absorption studies of isolated molecules or bulk systems have resulted in greater understanding of their geometrical and electronic structures, particularly in the case of large polyatomic systems where fluorescence of the excited upper state formed from the absorption of a photon is weak or non-existant.

Most absorption spectroscopy techniques follow some basic principles. The sample is illuminated by a light source of known intensity and the amount of light transmitted through the sample to a detector is measured. Equation 2.5 shows the absorbed light resulting from the difference in intensity between the incident light (I_0) and the transmitted light, $I(d,\lambda)$ [40] .

$$\Delta I = I_0 - I(d,\lambda) \quad \ldots(2.5)$$

The transmitted intensity follows the Beer-Lambert law shown in Equation 2.6 [40]

$$I = I_0 \, e^{[-\alpha(\lambda)cd]} \quad \ldots(2.6)$$

where d, α and c are the length of the cell , absorption coefficient and concentration of the sample, respectively.

One of the simplest techniques in absorption spectroscopy is Direct Absorption (DA) which allows information like quantitative concentrations and absolute frequency dependent cross sections on species in any phase (gas, liquid or solid) to be determined. The biggest disadvantage of DA spectroscopy is that it relies on a measurement of a small change in power from a high level; any noise introduced by the light source or the transmission through the

optical system will deteriorate the sensitivity of the technique. This detection limit is insufficient for many types of applications.

Improvements in the reflectivity of dielectric mirror coatings allowed O'Keefe and Deacon [41] to develop a new technique based on the measurement of the decay of absorption of a sample in a closed cavity following pulsed laser excitation. In fact, O'Keefe and Deacon [41] were the first to obtain a spectrum by using the technique which they called Cavity ringdown (CRD) spectroscopy. In a review, Paldus and Kachanov [40] give a well-detailed historical overview of direct absorption methods and CRD spectroscopy to 2005.

CRD spectroscopy measures the rate of decay of light intensity in a stable optical cavity. Briefly, light coming out from the laser is focused into an optical cavity that has two concave mirrors. The length of the cavity and the radius of curvature of the mirrors are important and determine whether a stable optical resonator is formed. The pulses of the laser circulate backwards and forwards between the mirrors and light is scattered and transmitted on every round-trip. The light transmitted by the back mirror is detected by a photodetector, usually a photomultiplier tube (PMT), and a spectrum of the cavity loss is obtained from the measurement of the decay constant or cavity ring-down time (τ) as a function of laser wavelength. Therefore, the difference in cavity loss, $(1/c\tau)$, between an empty cavity and a cavity containing a sample at a wavelength that is in resonance with an absorption of the sample gives the absolute absorption coefficient (α) of the sample. Fig. 2.10 illustrates the schemes for CRD spectroscopy.

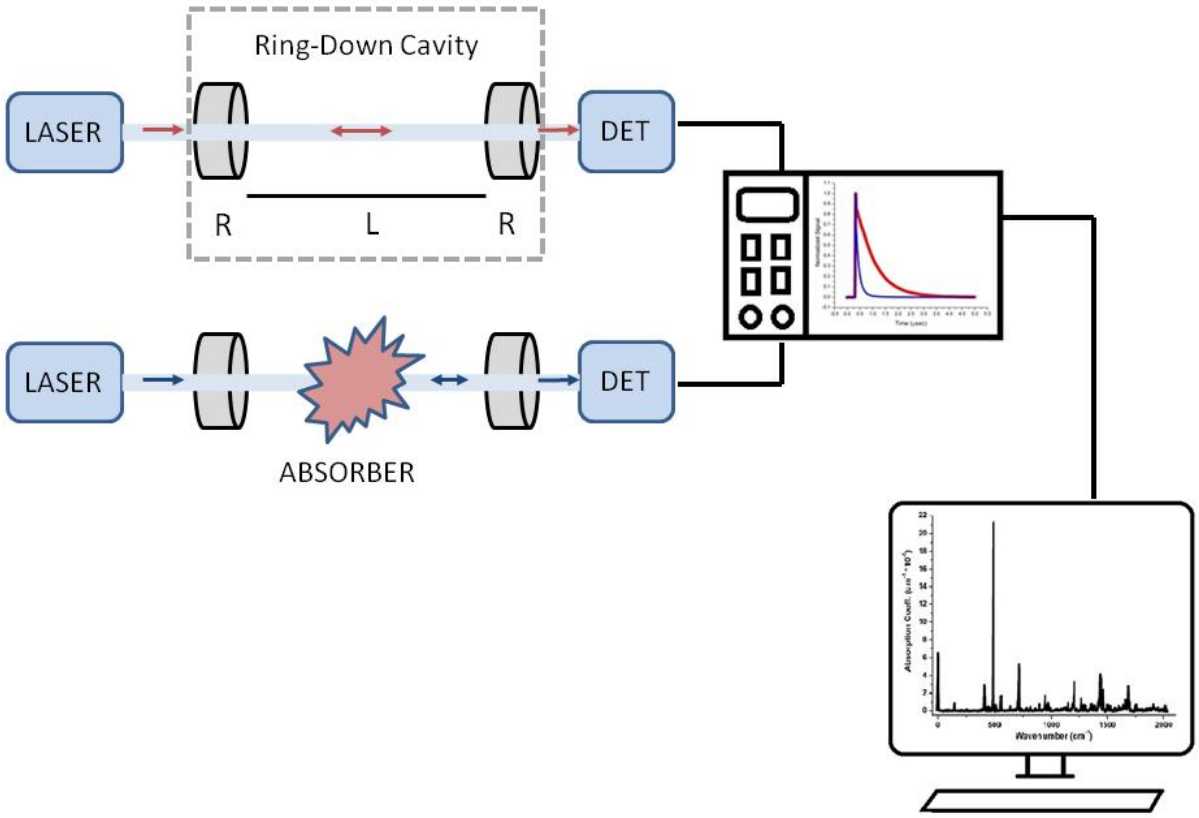

Figure 2.10: Scheme of the experimental setup for CRD spectroscopy. The sample is contained in the ring-down cavity with length L consisting of two mirrors with reflectivity R. The decay time of a light pulse trapped in the ringdown cavity is measured as a function of wavelength and compared for the cases when the sample is, or is not, present.

The intensity of the pulse decreases exponentially in time with a rate determined by the reflectivity of the mirrors, the length of the cavity and any scattering or absorption by material in the cavity. In the case when there is no sample in the cavity, the ring-down time is defined by equation 2.7 [42].

$$\tau = \frac{L}{c(\ln R + A)} = \frac{L}{c[(1-R)+A]} \quad \ldots(2.7)$$

where τ is the ring-down of the cavity, L is the distance between the mirrors, c is the speed of light and R is the reflectivity of the mirrors and A represents losses of the cavity due to absorption, scattering and diffraction that are not related to the sample. Since CRD spectroscopy systems use high reflectivity mirrors, R is typically on the order of 0.99 and can be approximated by ln R = (1- R).

The light in a cavity filled with an absorbing sample decays exponentially with the ring-down time (τ_1) given by equation 2.8 [42].

$$\tau_1 = \frac{L}{c(\ln R + A + \alpha d)} = \frac{L}{c[(1-R)+A+\alpha d]} \quad \ldots(2.8)$$

where α is the frequency-dependent absorption coefficient of the sample and d is the length of the cavity where the sample is present.

As mentioned above, the absorption spectrum is obtained by plotting the cavity losses as a function of frequency as shown in equation 2.9 while the minimum detectable absorption will be defined by equation 2.10 [42].

$$\frac{1}{[c\,\tau(\nu)]} = \frac{(1-R)+\alpha(\nu)d}{L} \quad \ldots(2.9)$$

$$\left(\frac{\alpha(\nu)d}{L}\right)_{\min} = \frac{(1-R)}{L}\left(\frac{\Delta\tau}{\tau}\right)_{\min} \quad \ldots(2.10)$$

with $\Delta\tau = \tau_1 - \tau_;$ being τ_1 and τ, the ring-down time with and without sample, respectively. Therefore, the ring down decay is in principle not affected by the intensity noise on the excitation laser making CRDS a very useful technique for direct absorption measurements. More detailed mathematical treatments of CRD spectroscopy can be found in the literature [40-43].

In this section, we report the $S_1(A\ ^1B_2) \leftarrow S_0(X\ ^1A_1)$ absorption spectrum of room temperature and jet-cooled PA measured with CRD spectroscopy in the 279 nm region

2. Experimental Setup

An optical parametric oscillator (Spectra-Physics MOPO-HF) was pumped by the 355-nm third harmonic wavelength from an Nd-YAG (Spectra-Physics - Pro 290) pulsed laser operating at 10 Hz. The horizontally polarized MOPO output beam (~30 mJ/pulse) typically ranged from 500 to 570 nm, and was directed via a flat dielectric mirror into a second harmonic generation (SHG) system where the polarization of the beam was rotated by a Fresnel Half-Wave Rhomb prior to passing through a type I BBO SHG crystal and a compensator crystal. The back-reflection from the Fresnel half-wave rhomb was sent to a wavemeter (Coherent WaveMaster) through a fiber optic cable for wavenumber calibration (estimated within 0.1 cm^{-1} accuracy, 0.03 cm^{-1} precision). The collinear fundamental and second harmonic beams were separated in a 4-Pellin-Broca prism separator (Lumonics, HT-75). Quartz prisms were used to direct the SHG beam onto a quartz window (45˚ to beam), and the attenuated partial reflection (several hundred μJ) from the quartz window was steered into the ringdown cavity. Irises were mounted along the beam path for day-to-day alignment, as well as to restrict the cross-sectional area of the beam.

The 92.5 cm long ring-down cavity comprised two highly reflective concave mirrors covering the 267-287 nm spectral range (AT Films), 3 m radius of curvature; 1-inch diameter, R=0.998 reflectivity at 277 nm as estimated from the ring-down decay lifetime. A photomultiplier tube (PMT, Hamamatsu 1P28) was positioned behind the exit mirror to monitor the light leaking out of the cavity. A quartz diffuser plate was introduced between the exit mirror and the PMT to ensure uniform illumination of the PMT. A delay generator (Stanford Research Systems DG535) provided timing pulses for the Nd-YAG flash lamp and Q-switch, pulsed nozzle, and triggered the oscilloscope. For each laser pulse, the cavity ring-down signal decay curve was measured and stored on a 300 MHz oscilloscope (LeCroy 9310M), and the averaged (typically from 35 to 200 shots per waveform) 500 point waveform was then transferred to the computer (running LabView) at each wavelength 0.05 cm^{-1} step of the absorbance scan.

The ringdown cavity spanned a vacuum chamber evacuated with a rough pump. Each mirror was positioned at the end of an arm connected to the central vacuum chamber. 98% pure PA (Farchan Division Chemsampco, Inc.) was used without any further purification. Argon (Ar) gas was bubbled through a liquid PA sample in a gas handling manifold, and for absorbance scans a small amount of this mixture was introduced into the central portion of the vacuum chamber. The argon backing pressure was optimized at roughly 400 Torr. The chamber was sealed for absorbance scans, while empty cavity background scans were recorded with a slow flow of argon through the chamber to eliminate any back-flow from the rough pump. For experiments using a sample, a pulsed slit valve (1 cm long slit parallel to beam, General Valve Corporation, Model 99), and two turbomolecular pumps (Edwards) were used to evacuate the chamber to pressures less than 10^{-6} torr. The slit-jet aperture was held approximately 2 cm above

the laser beam axis. Chamber pressure during operation of the nozzle was typically 4×10^{-5} torr. Fig. 2.11 describes the setup of the system used to do high resolution measurements.

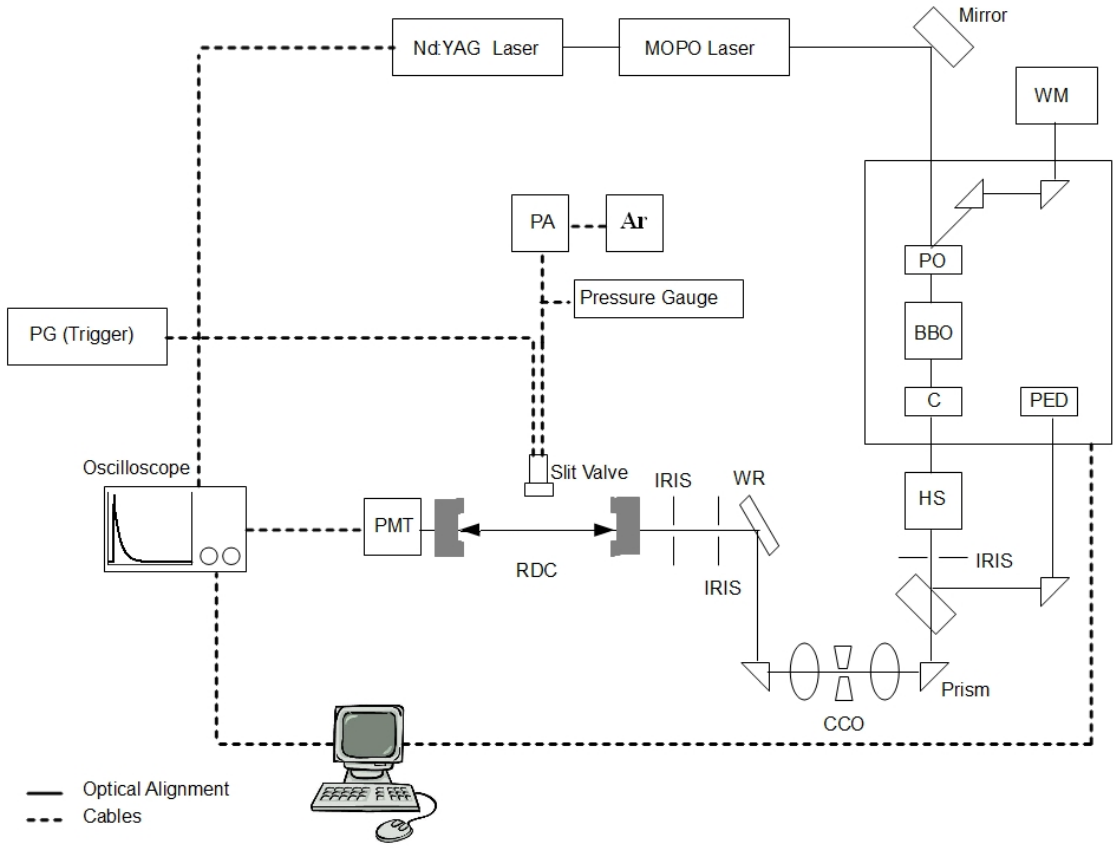

Figure 2.11: Setup of the system used to do jet-cooled measurements. WM: Wavelength Meter, PO: Polarization Rotator, C: Compensator, HS: Harmonic Separator, PED: Pyroelectric detector, CCO: Cavity Coupling Optics, WR: Wedged reflector, RDC; Ringdown Cavity, PMT: Photo-multiplier Tube, PG: Pulse Generator, Ar; Argon as carrier gas with backing pressure 400 Torr).

3. Results and Discussions

Before recording a spectrum with our cavity ring-down system, we first characterized the cavity mirrors and detection system. Fig. 2.12 shows two different decay waveforms: the 680 ns decay corresponds to an empty cavity, while the 240 ns decay corresponds to that recorded with the laser on a PA absorption line. The 680 ns decay curve was recorded by averaging 200 waveforms on the oscilloscope, and the 240 ns decay corresponded to a 50 shot average. Neglecting the first few points that typically contained some systematic radio-frequency noise, the signals were fit using a nonlinear least-squares Levenberg–Marquardt fitting algorithm and with analytical derivatives to the formula [40]:

$$V(t) = V_0 e^{-t/\tau} \quad \ldots(2.11)$$

to extract the ring-down time, τ.

The general equation to convert a measured ring-down decay time (τ) to an absorption coefficient (α) is [42]:

$$\alpha = N\sigma = \frac{1}{c}\left(\frac{1}{\tau} - \frac{1}{\tau_0}\right) \quad \ldots(2.12)$$

where c is the speed of light, τ_0 corresponds to the empty cavity decay lifetime, τ corresponds to the ring-down time when an absorbing species is present, σ is the absorption cross-section in cm^2, and N is the number density in molecules cm^{-3}. A major attribute of CRD spectroscopy is that the ring-down time, and thus the absorption coefficient, should be invariant with respect to fluctuation in, as well as average, laser intensity. Tests showed that PMT saturation could lead to apparent systematic changes in measure ring-down times and the system was operated with low intensities to avoid this regime.

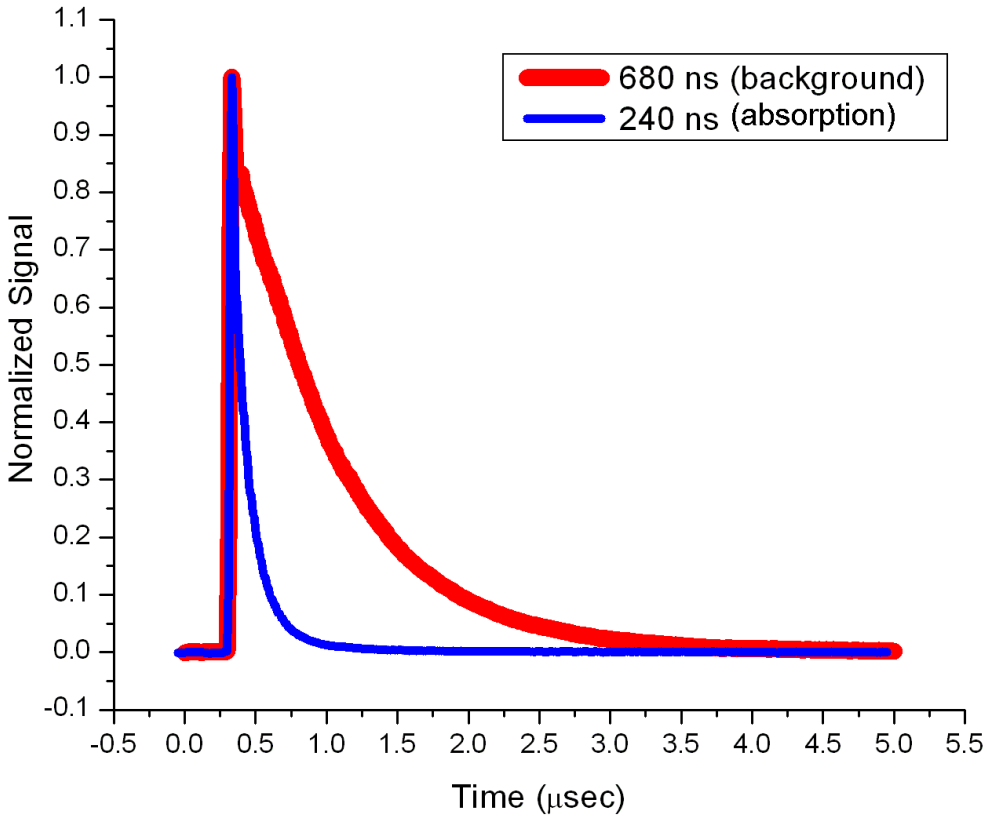

Figure 2.12: CRD signals for the empty cell (background) and with sample (absorption).

For a typical room temperature scan, we positioned the laser at the peak of the ambient temperature PA $S_1 \leftarrow S_0$ band origin, approximately 35 878 cm^{-1} and introduced an argon-PA gas mixture until the ring-down lifetime dropped by a factor of 2. We then proceeded to record a spectral region. Next, we recorded a background scan by evacuating the chamber.

A room temperature PA spectrum in the region near the band origin is shown in Fig. 2.13. Two separate scans were concatenated to produce the spectrum shown in Fig. 2.13. The higher wavenumber section was recorded at a 0.8 cm^{-1} step size (40 waveforms averaged per laser step), and, the origin band region below 36 000 cm^{-1} was recorded at a 0.4 cm^{-1} step size (50 waveforms averaged per laser step). The background spectrum was recorded at a lower (5 cm^{-1} per step) resolution (200 waveforms averaged per laser step point). Each CRD spectrum was subtracted from the average background signal. The data follow the published (lower resolution) classical absorption spectrum recorded by King and So [1] closely. By comparison to the King and So spectrum we estimate that the pressure of PA in the CRD experiment is less than 18 mTorr.

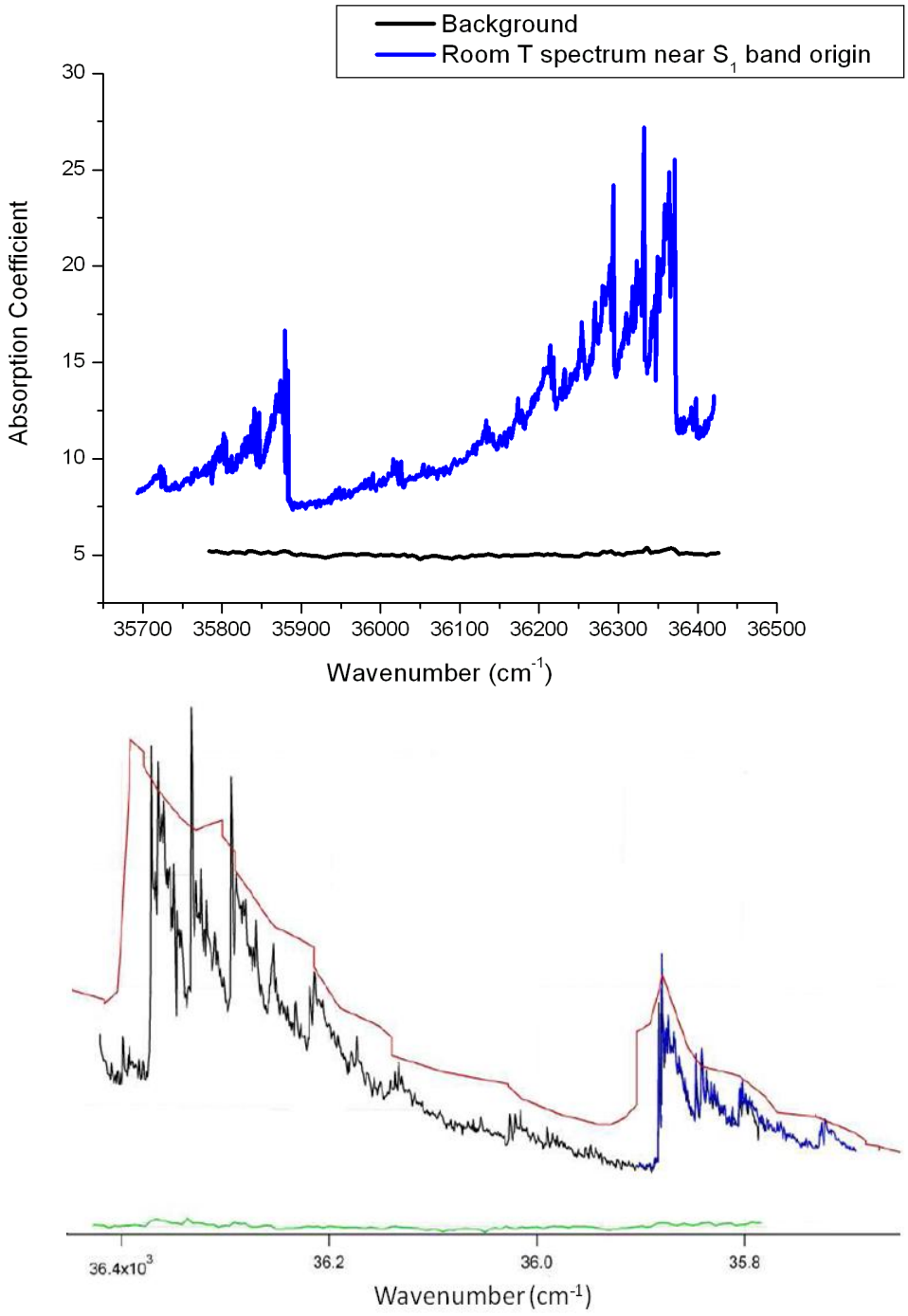

Figure 2.13: Upper and lower panels: Room temperature spectrum near band origin and background. Lower panel: Comparison between the concatenated room temperature spectrum from in this work to the low-resolution classical absorption spectrum recorded by King and So [1] (red) and the background run (green) [44].

Following initial characterization of the apparatus using the ambient temperature sample, the complete spectrum was recorded from 180 cm^{-1} below the band origin to 2000 cm^{-1} above, i.e. from approximately 35 700 cm^{-1} to 37 900 cm^{-1} using a slit-jet cooled sample. Background subtraction was performed by averaging a waveform at each laser wavenumber, at two laser time delays relative to the pulsed valve trigger. The first recorded the signal with gas pulsed present while the second corresponding to the empty chamber at the same laser wavenumber position. This method is preferable to the method used collecting the room temperature spectrum (first recording a foreground spectrum, and then later recording a background spectrum) because any long term change in the cavity (i.e. alignment) is accounted for.

The electronic band origin of the S_1 state of PA was measured at 35 878.1 cm^{-1}. This value is close to the 35 877.18 cm^{-1} measured by Ribblett et al. [35] in the fully rotationally resolved molecular beam spectrum. As noted here, one of the features in the allowed bands in the spectrum is the lack of prominent central Q-branches. The modes 15, 6a, βCC, 6b and 1, appear as the strong bands in the spectrum below 1000 cm^{-1}. The vibrational energies of these modes are 147, 410, 493, 561 and 718 cm^{-1}, respectively. In agreement with our analysis of the 1+1 REMPI spectrum reported in the previous section and already published [27], we find the vibrational mode βCC (b_2 symmetry) is the strongest band in this spectrum since it has the most vibronic strength.

Most strong transitions in this region have been assigned in previous studies, and they need not be discussed further. However, the lower intensity bands are much more of a challenge. Two weak bands appeared in the low-energy part of the spectrum above the band origin. The first one can be seen at 70 cm^{-1}; however, there is no vibrational mode at this low energy that can be assigned to this peak. Thus it must be a hot band. The second peak with significant intensity

is located at 91 cm^{-1}. This mode has also been previously observed, experimental and theoretically, and assigned as 10b [8, 27]. The vibration of this band represents an out-of-plane acetylene-phenyl bend that should be forbidden considering its b_1 symmetry. Coriolis coupling calculations by Chang et al. [27] demonstrated this mode borrows intensity from this nearby mode 15, but this effect does not completely explain its appearance in the REMPI or CRD spectrum. Another two closely spaced weak transitions can be clearly observed at 555 and 561 cm^{-1}. The lower peak was wrongly assigned to βCH by Powers et al. [36] and to 6b by Narayanan et al. [8]. However, our recent theoretical calculations, reported in the next section of this chapter and already published [27], combined with our REMPI [27] and CRD results leads us to believe that the bands at 555 cm^{-1} and 561 cm^{-1} correspond to $6a^{1}15^{1}$ and 6b, respectively. The presence of a peak at 515 cm^{-1} previously reported and assigned to a 10b mode using 1+1 REMPI by Chang et al. [27] was confirmed. The vibrational modes and symmetries for S_1 are summarized in Table 2.5.

Fundamental bands or combination bands of the low frequency modes can be found as the intensity scale is expanded in the spectrum. Most of these features have been assigned and are in good agreement our previous study using REMPI and theoretical calculations [27]. The entire CRD spectrum is shown in Fig. 2.14 and shows that the assignment of the vibrational levels at the low excitation energy is clear. However, as the excitation energy increases it becomes impossible to clearly assign any possible vibrational levels without ambiguity. Table 2.6 gives band positions and absolute intensities measured in this work and compare them with the ones obtained in a previous study using 1+1 REMPI [27] and some other references. We used Wilson's notation [30] to label the vibrational modes since it is more consistent between states of the molecule and between the various substituted benzenes.

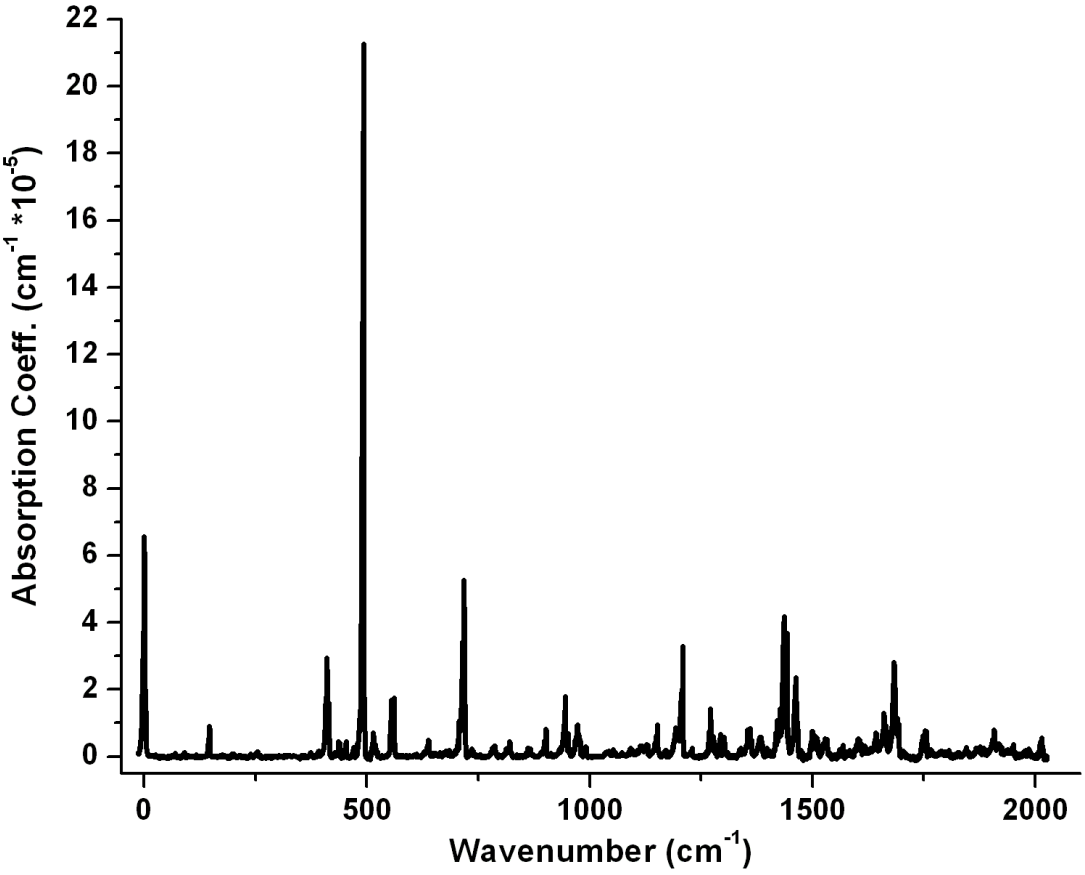

Figure 2.14: Overview of the **s**lit jet-cooled CRD spectrum of S_1 PA

Table 2.5: Direct absorption intensities from the CRD spectrum for the assigned vibrational features (modes) of the $S_1 \leftarrow S_0$ Transition of PA

Freq (cm^{-1})	mode		Exp. Intensity*	Freq (cm^{-1})	mode		Exp. Intensity*
0	0		6.55	1209	$\beta CC^1 1^1$	b_2	3.29
91	$10b^1$	b_1	0.12	1229	$6a^3$	a_1	0.24
147	15^1	b_2	0.90	1271	$6b^1 1^1$	b_2	1.42
176	γCC^1	b_1	0.07	1293	3^1	b_2	0.65
197	$10b^2$	a_1	0.08	1357	$6a^1 12^1$	a_1	0.82
240	$10b^1 15^1$	a_2	0.08	1384	$6a^1 18a^1$	a_1	0.58
374	$\gamma CC^1 16a^1$	b_2	0.11	1436	$\beta CC^1 12^1$	b_2	3.31
410	$6a^1$	a_1	2.94	1443	$19b^1$	b_2	3.69
454	$16a^2$	a_1	0.46	1463	$\beta CC^1 18a^1$	b_2	2.36
493	βCC^1	b_2	21.25	1500	$6b^1 12^1$	b_2	0.70
515	$10b^1 6a^1$	b_1	0.70	1532	$6b^1 18a^1$	b_2	0.50
556	$15^1 6a^1$	b_2	1.69	1569	$9b^1 6a^1$	b_2	0.34
561	$6b^1$	b_2	1.74	1603	$13^1 6a^1$	a_1	0.54
639	$\beta CC^1 15^1$	a_1	0.50	1618	$\beta CC^1 6a^1 1^1$	b_2	0.31
718	1^1	a_1	5.27	1643	$8b^1$	b_2	0.69
754	$6b^1 10b^2$	b_2	0.06	1660	$1^1 12^1$	a_1	1.29
787	$\beta CC^1\ \gamma CC^2$	b_2	0.32	1683	$\beta CC^1 13^1$	b_2	2.81
820	$6a^2$	a_1	0.44	1755	$13^1 6b^1$	b_2	0.61
862	$15^1 1^1$	b_2	0.26	1845	$9a^1 1^1$	a_1	0.25
902	$\beta CC^1 6a^1$	b_2	0.81	1868	$9b^1 1^1$	b_2	0.25
945	12^1	a_1	1.79	1876	$\beta CC^1 6a^1_1 18a$	b_2	0.28
954	$18a^1$	a_1	0.69	1884	12^2	a_1	0.20
990	$18b^1$	b_2	0.29	1908	$13^1 1^1$	a_1	0.80
1098	$15^1 12^1$	b_2	0.29	1916	$\beta CC^1 1^2$	b_2	0.37
1127	$9a^1$	a_1	0.36	1925	$18a^1 12^1$	a_1	0.27
1152	$9b^1$	b_2	0.93	1951	$18a^2$	a_1	0.34
1193	13^1	a_1	0.87	2014	$3^1 1^1$	a_1	0.55

* Absorption Coefficient at the peak in cm^{-1} $x10^{-5}$

Table 2.6: Comparison between our experimental results for the fundamental vibrational frequencies of PA in the S_1 state and other references.

Symmetry	Mulliken	Wilson[a]	1+1 REMPI. Exp.*	CRD Exp.*	King and So[b]	Chia and Goodman[b]	Mode Description[c]
a_1	ν_1	νCH					C_8H_8 stretch
	ν_2	2					CH stretch
	ν_3	20*a*					CH stretch
	ν_4	7*a*					CH stretch
	ν_5	νCC			2061		$C_7{\equiv}C_8$ stretch
	ν_6	8*a*					CCH bend
	ν_7	19*a*	1419				CCH bend
	ν_8	13	1191	1193	1191	1200	C_1C_7 stretch, CCH
	ν_9	9*a*	1126	1127	1057		CCH bend
	ν_{10}	18*a*	954	954	951	954	Ring deformation
	ν_{11}	12	945	945	944	944	Ring deformation
	ν_{12}	1	719	718	717	722	Ring breath
	ν_{13}	6*a*	409	410	409	409	$C_7C_8H_8$-ring breath
a_2	ν_{14}	17*a*			728		OP CCH-ring breath
	ν_{15}	10*a*			656		OP CCH bend
	ν_{16}	16*a*	224		220		OP CCH bend
b_1	ν_{17}	5			731		OP CCH bend
	ν_{18}	17*b*			710		OP CCH bend
	ν_{19}	11			586		OP CCH bend
	ν_{20}	4			470		OP CCH bend
	ν_{21}	γCH					OP ring deformation
	ν_{22}	16*b*			362		OP ring def, $C_7C_8H_8$
	ν_{23}	γCC	168	176			OP ring def, $C_7C_8H_8$
	ν_{24}	10*b*	97	91	163		OP ring def, $C_7C_8H_8$
b_2	ν_{25}	7*b*					CH stretch
	ν_{26}	20*b*			3079		CH stretch
	ν_{27}	8*b*	1642	1643			Ring deformation
	ν_{28}	19*b*	1442	1443			Ring deformation
	ν_{29}	14				1575	CCH bend
	ν_{30}	3	1296	1293			CCH bend
	ν_{31}	9*b*	1152	1152	1075		CCH bend
	ν_{32}	18*b*	990	990	972		CCH bend
	ν_{33}	βCH					$C_7C_8H_8$ bend
	ν_{34}	6*b*	561	561	560		Ring deformation
	ν_{35}	βCC	493	493	492		$C_1C_7C_8$ bend
	ν_{36}	15	146	147	322		CCH, $C_7C_8H_8$ bend

[a.] The symbol ν indicates a stretch, β means an in-plane bend, and γ means an out-of-plane bend.
[b.] G. W. King and S. P. So.[1]; C. L. Chia and L. Goodman [5].
[c.] Serrano-Andres et.al. [2]. The descriptions are the main contributions to the normal modes. The acetylene carbons are 7 and 8, C_7 is attached to the ring at C_1, while a lack of atom numbering indicates the H or C belongs to the phenyl ring.
* Freq. in cm^{-1}.

We also assigned the hot bands observed near the $S_1 \leftarrow S_0$ band origin shown in Fig. 2.15 by comparing the value obtained from subtracting known excited state from the ground state frequencies and levels to the value of the peak observed in the spectrum. The results are presented in Table 2.7, and show that there are difficulties with some previously assigned frequencies. It is likely that the S_1 176 cm^{-1} peak assigned by King and So [1] is not γCC, and the assignments of the 224 cm^{-1} and 470 cm^{-1} peaks could also bear further scrutiny.

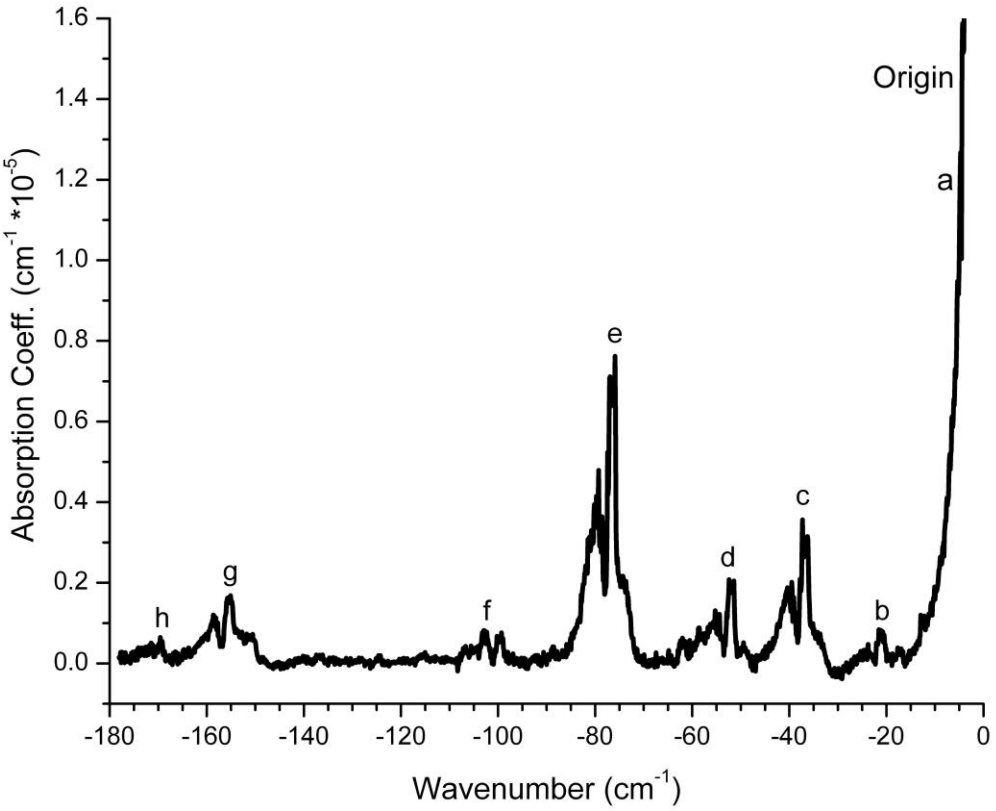

Figure 2.15: Hot band region in the slit jet CRD spectrum near the band origin of S_1 PA showing rotational band contours. See Table 2.7 for assignments.

Table 2.7: Tentative assignments of the hot bands near the band origin of S_1 PA. Experimental and calculated frequencies are in wavenumbers. Calculated frequencies were obtained with CAM-B3LYP.

	S_0				S_1				$\Delta\nu(\nu_{S1}-\nu_{S0})$			Hot bands	
		Calc. Freq.				Calc. Freq.			Calc. Freq.				Peak
Assignment	Symm.	ACCD[c]	ACCT[c]	Exp.[b]	Symm.	ACCD	ACCT	Exp.[b]	ACCD	ACCT	Exp.[b]	Freq.	Label[a]
10b	b_1	136	144	140[45][4]	b_1	98	93	91	-38	-51	-49	-37	c
15	b_2	158	162	152[45][4]	b_2	150	154	147	-8	-8	-5	~ -5	a
γCC	b_1	354	375	349[45][4]	b_1	265	292	176[1]	-89	-83	-173	-76	e
16b	b_1	555	563	530[1]	b_1	378	381	362[1]	-177	-182	-168	-169	h
16a	a_2	418	418	417[1]	a_2	264	251	224[34]	-154	-167	-193	-155	g
6a	a_1	473	477	463[45][4]	a_1	408	412	410	-65	-65	-53	-52	d
γCH	b_1	609	687	613[1]	b_1	493	508	470[1]	-116	-179	-143	-99	f
βCC	b_2	534	547	514[1]	b_2	435	448	493	-99	-99	-21	-21	b
4	b_1	718	722	689[1]	b_1	532	618	586[1]	-186	-104	-103		
11	b_1	793	797	756[1]	b_1	603	622	710[1]	-190	-175	-170		

a. See Fig. 2.14
b.Experimental Freq. from present results, King and So [1], Chang et al. [27], and Bacon et al. [46].
c. ACCD: aug-cc-pVDZ, ACCT: aug-cc-pVTZ described in section III of this chapter.

A section of the normalized CRD spectrum obtained in this work has been compared with Chang et al. normalized results with 1+1 REMPI, this comparison is shown in Fig. 2.16. It is observed that the strongest bands (βcc and 1) are attenuated in the REMPI spectrum while weaker bands (including most a_1 modes) vary somewhat randomly between techniques. The attenuation, also shown in Fig. 2.17, is related to the fact that the stronger peaks can be affected more by saturation in a nonlinear process. Also the relative intensities obtained from the REMPI experiment are affected by the laser intensity and various non-linear and saturation effects as the laser is scanned across a dye region, while in the case of CRD, laser intensity and mode structure do not influence relative absorption strengths. Table 2.8 compares the relative band intensities from the REMPI and CRD experiments, independently normalized to their origin band intensities. The last column in this table gives a different normalization of the REMPI intensities, scaled instead to match the total intensity of the CRD set. This is illustrated in Figure 2.17b.

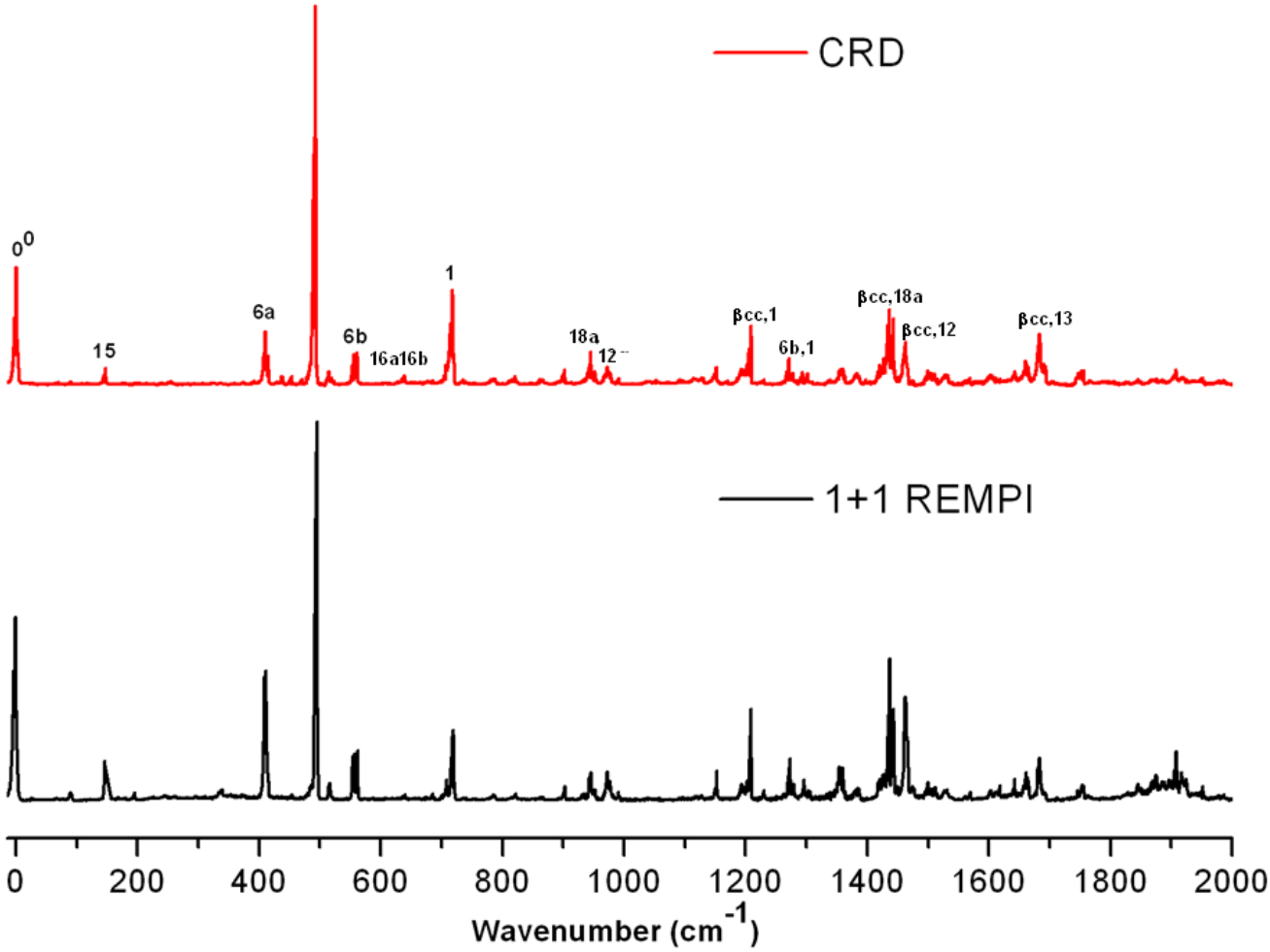

Figure 2.16: Comparison of a section of the normalized CRD and 1+1 REMPI spectra up to 2000 cm^{-1}.

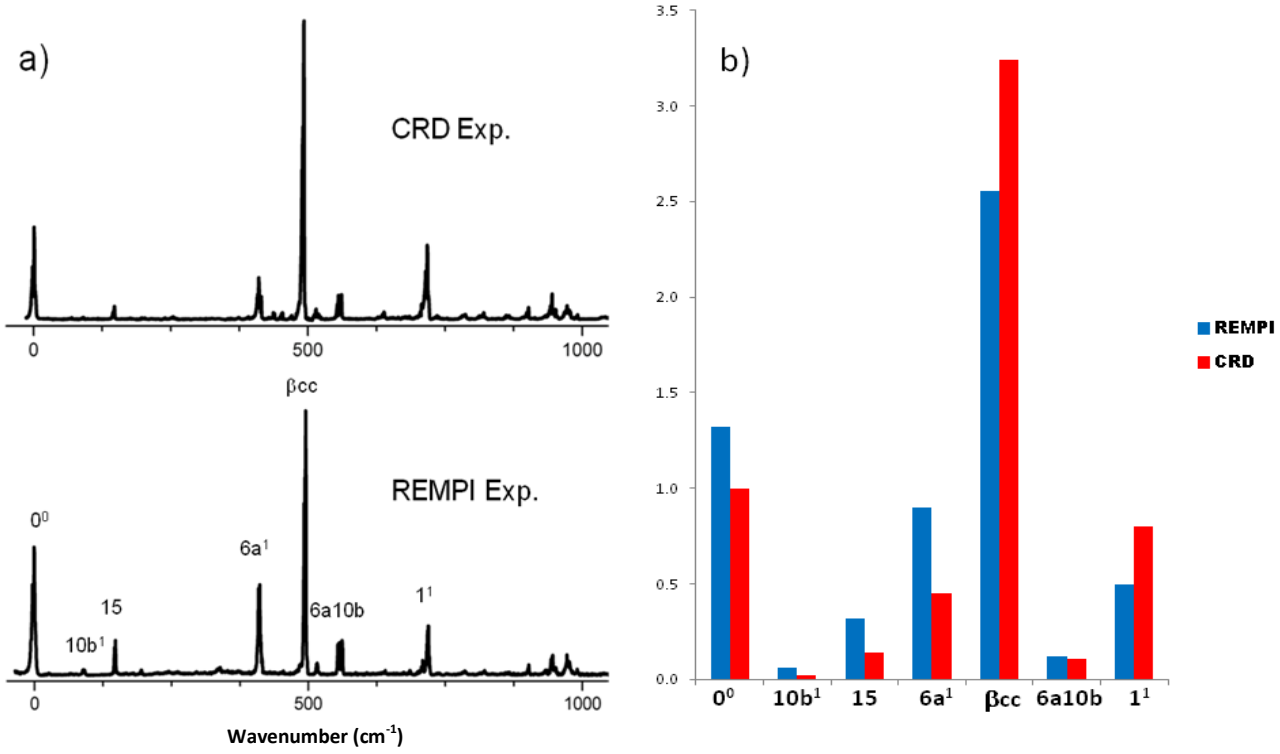

Figure 2.17: a) CRD and REMPI assignments of a few strong bands of the S_1 PA spectra up to 1000 cm^{-1} b) CRD intensities normalized to the origin band and REMPI intensities scaled to make the sum equal to the CRD intensity sum (see Table 2.8), for the bands labeled in the left hand panel.

Table 2.8: Relative intensities from the REMPI and CRD experiments normalized to the band origin intensities. REMPI intensities are also scaled to the same sum as CRD set and have been plotted in Fig. 2.17b.

	CRD	REMPI	
Band	**Intensity**$^{+}$	**Intensity**$^{+}$	**Scaled Intensity***
0	1.00	1.00	1.32
10b	0.02	0.04	0.06
15	0.14	0.24	0.32
6a	0.45	0.68	0.90
βCC	3.24	1.94	2.56
6a10b	0.11	0.09	0.12
1	0.80	0.37	0.39
Sum	5.76	4.37	

\+ normalized to band origin

* $Scaled\ \ Intensity = REMPI\ \text{int}ensity\left(\frac{\sum CRD\ \text{int}ensity}{\sum REMPI\ \text{int}ensity}\right)$

4. Conclusions

The $S_1(A\ ^1B_2) \leftarrow S_0(X\ ^1A_1)$ electronic absorption spectrum of room temperature and jet-cooled PA has been measured. The CRD spectrum was primarily recorded to check the relative vibronic band intensities in the $S_1 \leftarrow S_0$ electronic band system, previously measured [27] in a resonance enhanced multi-photon ionization (1+1 REMPI) experiment.

CRD measures the rate of decay of light intensity in a stable optical cavity and the intensity is related to the direct absorption of the species which is not affected by the laser intensity. REMPI tends to attenuate the intensity of the strong band and increase the apparent strength of weaker bands because of partial saturation. Since CRD provides a direct absorption spectrum free of laser intensity effects, results from this technique are very useful when comparing to simulated spectra as discussed below. The assignment of a number of previously unobserved vibronic hot bands has been also reported.

III. Theoretical Calculations

A. Introduction

The capability to predict optical spectra has many applications in problems associated with such areas as chemical physics, remote sensing and astronomy. To refine this predictive capacity, one needs to compare methods using the most accurate theories to accurate experimental data. A key problem in predicting the electronic spectra of molecules is calculating the interaction of the vibrational and electronic motions, i.e. Born-Oppenheimer breakdown effects. These vibronic interactions may determine the vibrational patterns of electronic

transitions that are optically weak at the equilibrium geometry. In addition to predicting spectra, vibronic calculations can serve as a sensitive test of the quality of the molecular potentials and wavefunctions produced by electronic structure calculations. Relative vibronic intensities can vary more dramatically with changes in the potential than either electronic or vibrational energies, and can indicate which parts of the potential are in need of improvement.

Calculating the intensities of the vibrational structure in weaker transitions of molecules can be difficult since many different vibrational modes can participate in providing intensity. However, increasing computational power and recent developments in electronic structure theory and methods now promise the possibility of accurate treatments of medium and large size systems. There are choices involved in doing electronic structure calculations, however, and to guide the selection of programs and methods there needs to be a careful comparison of theoretical results to experimental values. Of course, to make such a validation, the experimental data must be as accurate as possible.

Self-consistent field (SCF) quantum methods were first used to study ground state potentials. However, these methods were not accurate enough to describe large molecules, especially their excited states. Configuration interaction singles (CIS) [47] appeared to be an improved method when it successfully predicted the molecular geometries and vibrational frequencies of molecules like benzene [48], anthracene [49], styrene [50] and 3-methylstyrene [50, 51] in their excited states.

Serrano-Andres et al. [2] applied the multi-configurational complete active space self-consistent field (MCSCF) method, a high-level theoretical calculation method, to molecules like PA. This method can be considered a combination between configuration interaction, and the Hartree–Fock method. MCSCF has been used to generate qualitatively correct reference states of

molecules in cases where Hartree–Fock and density functional theory are not adequate. A particularly important MCSCF approach is the complete active space SCF method (CASSCF), where the linear combination of CSFs includes all that arises from a particular number of electrons in a particular set of orbitals. CASSCF includes all possible determinants, with the proper symmetry, that can be formed by distributing a set of active electrons among a set of active orbitals.

Density functional theory (DFT) is a popular electronic structure theory to study large ground state systems. Time-dependent density functional theory (TD-DFT), an extension of DFT for treating excited states, has also been developed to the stage where it is now very widely used [47].

Nowadays, absorption spectra and some other molecular properties can be calculated with TD-DFT. The geometry of excited states can be optimized by calculating energy gradients at low computational cost when compared to even lower-level ab initio molecular dynamics methods like configuration interaction singles (CIS) [48, 49]. However, some limitations appear when performing TD-DFT calculations. The most significant is the underestimation of the Rydberg excitation energies, oscillator strengths and the charge-transfer excitations. Rydberg excitation energies provided by TD-DFT with pure functionals such as B3LYP are usually smaller than the experimental values.

Initially, these problems were related to the incorrect far-nucleus behavior of the functional since the σ-spin exchange-correlation energy functional (Eq. 2.13) in most functionals cannot reproduce the far-nucleus asymptotic behavior as shown in Eq. 2.14 [48, 49].

$$v_{xc}^{\sigma} = \frac{\delta E_{xc}}{\delta \rho_{\sigma}} \quad \ldots(2.13)$$

$$\lim_{R\to\infty} v_{xc}^{\sigma}(R) = -\frac{1}{|R|} \quad \ldots(2.14)$$

with E_{xc} as the exchange-correlation energy functional; ρ_{σ}, the σ-spin electron density and R the distance vector from the nearest nucleus. Tozer et al. [50] proposed an asymptotic correction (AC) to improve the functional potentials (Eq. 2.15).

$$\lim_{R\to\infty} v_{xc}^{\sigma}(R) = -\frac{1}{|R|} + \varepsilon_{\sigma}^{HOMO} + I_{\sigma} \quad \ldots(2.15)$$

with $\varepsilon_{\sigma}^{HOMO}$ representing the eigenvalue of the highest occupied σ-spin molecular orbital and I_{σ} is the ionization potential of the σ-spin electron. However, Kamiya et al.'s [51] study demonstrated that the calculated dissociative energy potentials of van der Waals bonds of rare-gas dimers were improved by combining a long-range correction scheme with the van der Waals functional. Moreover, their results suggested that the poor results of B3LYP are due to the insufficient exchange interaction between distant orbitals in exchange functionals rather than incorrect far-nucleus asymptotic behavior.

Long-range correction (LRC) schemes incorporate the long-range orbital–orbital interaction part in the exchange functional by combining it with the Hartree-Fock (HF) exchange integrals. The electron repulsion operator is divided into short-range and long-range parts by using the standard error function (Eq. 2.16).

$$\frac{1}{|R|} = \frac{1-erf(\mu R)}{|R|} + \frac{erf(\mu R)}{|R|} \quad \ldots(2.16)$$

with μ as the ratio of the short-range interaction to the long-range interaction and equal to 0.33 [48]. Also, $R = r_1 - r_2 = r_{12}$. The first term accounts for short-range interaction while the second one for the long-range interaction.

Yanai et al. [52] introduced additional parameters (α, β) to the partitioning in (2.16) to increase the flexibility of the exchange term proposed by Tawada et al. [48]. This scheme is shown in Eq. 2.17.

$$\frac{1}{|R|} = \frac{1-[\alpha+\beta\cdot erf(\mu R)]}{|R|} + \frac{\alpha+\beta\cdot erf(\mu R)}{|R|} \quad \ldots(2.17)$$

This method is known as the Coulomb-attenuating method (CAM) and must satisfy $0 \le \alpha + \beta \le 1$, $0 \le \alpha \le 1$ and $0 \le \beta \le 1$ where α is the factor that allows one to incorporate the HF exchange contribution over the whole range, while β is the parameter that allows one to incorporate the DFT counterpart over the whole range by a factor of $[1 - (\alpha + \beta)]$. Yanai et al. tested the performance of this approach with $\alpha = 0.19$, $\alpha + \beta = 0.65$ and Tawada et al.'s value for μ (0.33) [48] at different generalized gradient approximation (GGA) functionals and demonstrated that CAM-B3LYP not only yielded high quality energies but excellent results predicting charge transfer excitations.

The interest on these new TD-DFT hybrid exchange–correlation functionals has increased over the past five years since their computational costs are comparable to those of the standard hybrid functionals (also known as pure functionals) [49]. Their performance has been examined in more complicated systems like medium size aromatic molecules, especially those with multiple low-lying $\pi \rightarrow \pi^*$ excited states, ^1L_a and ^1L_b, where B3LYP overestimates the energy of the ^1L_a state while the energy of the ^1L_b state is reasonable. Recent studies by Richard et al.[53] have shown that LRC-TD-DFT approaches avoid the severe underestimation of the ^1L_a

state even and results have suggested that this excited state may exhibit some charge-transfer (CT) character.

Recently, correlation-consistent polarized basis sets have become widely used and are the current state of the art for correlated or post-Hartree-Fock calculations. Some of the most widely used basis sets are those developed by Dunning and coworkers [54]. The basis sets are cc-pVNZ where N=D,T,Q,5,6,... (D=double, T=triples, etc.), the 'cc-p', stands for 'correlation-consistent polarized' and the 'V' indicates they are valence-only basis sets and they include successively larger shells of polarization (correlating) functions (d, f, g, etc.). These basis sets can be augmented with core functions for geometric and nuclear property calculations, and with diffuse functions for electronic excited-state calculations, electric field property calculations, and long-range interactions, such as Van der Waals forces.

Vibronic effects in a molecular optical transition are commonly associated with those that are forbidden by symmetry. However, vibronic activity can also occur in allowed transitions and indeed can occur in any molecular spectrum. Generally, the weak S_1 transitions in many aromatics such as substituted benzenes like PA and naphthalene provide fertile ground for the study of vibronic contributions to formally allowed transitions [27].

Our group has previously discussed the use of modern quantum mechanical programs for calculating vibronic effects (i.e. coupling) [12]. Briefly, the wave function of a particular electronic-vibrational state can be written as a product of the electronic function ψ with a vibrational function χ in the Born-Oppenheimer approximation. These functions dependent on the electronic coordinates (q) and the nuclear coordinates (Q):

$$\Psi(q,Q) = \psi(q,Q)\,\chi(Q) \quad \ldots(2.18)$$

The intensity of any particular vibronic transition is proportional to the square of the transition moment M between the upper (u) and lower (l) states:

$$M_{ul} = \langle \psi_u \, \chi_u \, | \, \mu \, | \, \psi_l \, \chi_l \rangle \quad \ldots(2.19)$$

with μ as the dipole moment operator, and the integration is over all electronic and nuclear coordinates.

The vibrations are described by expressing the nuclear coordinates in terms of vectors in the displacements of each atom from its equilibrium nuclear position, giving rise to a set of normal coordinates [55] appropriate to the nuclear force field. The vibrational wave functions are then simply the products of harmonic oscillator functions along each normal coordinate. Since the force fields and the equilibrium positions of two electronic states can be different, two different coordinate sets, Q_i' and Q_i'' for the two states have to be defined [47]. These sets are related by the Duschinsky transformation $Q' = JQ'' + K$, where J is a rotation matrix and K is a geometry displacement vector [27, 56].

A geometry dependent transition moment M(Q) is obtained by integrating over the electronic coordinates for a particular nucleus configuration and integration of this over the vibrational wave functions gives the transition moment for an individual vibronic band, M_{ul}

$$M_{ul} = \left\langle \chi_u(Q') \, | \, M(Q) \, | \, \chi_l(Q'') \right\rangle \quad \ldots(2.20)$$

The transition moment could be obtained by calculating M(Q) with an electronic structure program at various geometries on the normal coordinate hypersurface and numerically integrating over the vibrational wave functions. Since the normal coordinate space has 3N - 6 dimensions, it is more practical to express M(Q) as a Taylor expansion in the normal coordinates for each polarization direction:

$$M(Q) = M(0) + \sum_i (\frac{\partial M}{\partial Q_i})_0 Q_i + \frac{1}{2}\sum_{ij} (\frac{\partial^2 M}{\partial Q_i \partial Q_j})_0 Q_i Q_j + \frac{1}{6}\sum_{ijk} (\frac{\partial^3 M}{\partial Q_i \partial Q_j \partial Q_k})_0 Q_i Q_j Q_k + \ldots \quad \ldots(2.21)$$

The terms of the moment expansion may be reduced to sums of vibrational overlap integrals times the derivatives of the transition moments by use of the recursion relation for Hermite polynomials [12]:

$$x H_n(x) = n H_{n-1}(x) + \frac{1}{2} H_{n+1}(x) \quad \ldots(2.22)$$

When these Hermite polynomials are introduced into the harmonic oscillator wave functions, the terms of the moment expansion become sums of vibrational overlap integrals times the derivatives of the transition moments. Eq. 2.23 and 2.24 correspond to the first and second order terms of the moment expansion [12].

$$Q_i \mid i^m \rangle = \alpha_i^{1/2} \left[\left(\frac{m+1}{2} \right)^{1/2} \mid i^{m+1} \rangle + \left(\frac{m}{2} \right)^{1/2} \mid i^{m-1} \rangle \right] \quad \ldots(2.23)$$

$$Q_i Q_j \mid i^m j^n \rangle = \frac{(\alpha_i \alpha_j)^{1/2}}{2} \{ [(m+1)(n+1)]^{1/2} \mid i^{m+1} j^{n+1} \rangle + [n(m+1)]^{1/2} \mid i^{m+1} j^{n-1} \rangle + [m(n+1)]^{1/2} \mid i^{m-1} j^{n+1} \rangle + [mn]^{1/2} \mid i^{m-1} j^{n-1} \rangle \} \quad \ldots(2.24)$$

with $\langle a^x b^y \ldots \mid$ and $\mid i^m j^n \ldots \rangle$ as the generic lower and upper state vibrational wave functions, respectively. The superscripts correspond to the number of excited quanta. Also, α_i is equal to $\hbar/(2\pi c \tilde{\nu}_i)$ with $\tilde{\nu}_i$ the vibrational energy for nuclei in wavenumbers.

In the present section, the sensitivity of vibronic calculations to electronic structure methods and basis sets is explored and compared to accurate relative intensities of the vibrational bands of phenylacetylene obtained previously. We tested a group of time dependent density

density functional theory (DFT) methods including pure functionals (B3LYP) and LRC functionals (LC-BLYP and CAM-B3LYP) in the calculation of the absorption spectra involving the low lying electronic states of PA. To the best of our knowledge this is the first time that these high-level theoretical methods have been used to study this or any related system. Results are compared with calculations done using MCSCF methods.

Instead of considering only the vibrations expected to appear in the spectrum, a more general approach was taken and moment derivatives were calculated to second order (all that is needed in C_{2V} symmetry [12]) for all of the non-CH stretch vibrations. The derivatives were determined from finite differences between the electronic transition moments calculated at various points along each of the normal modes for the first derivatives and also at simultaneous excursions along each pair of normal modes for the second derivatives. A matrix of second derivatives is called a Hessian, and the moment Hessians were determined for each vibrational level.

B. Methods

To simulate the vibronic spectra of PA, the ground and excited state geometries, vibrational frequencies and transition moments had to be calculated. Currently, reliable excited state vibrations can be obtained either with CASSCF or TD-DFT theories with large basis sets (e.g. Dunning basis sets). However, the version of GAMESS [57] available at the time of doing the initial calculations did not allow the calculation of vibrational frequencies by TD-DFT. With this limitation in mind, the initial simulation of the vibronic spectra was done with two different levels of theory: MCSCF was used to obtain the optimized geometries, vibrational vectors and frequencies while TD-DFT was used to get the transition moments. Additionally, our version of

GAMESS does not perform analytic second derivatives on f-orbitals which mean that aug-cc-pVTZ cannot be used with GAMESS, aug-cc-pVDZ was used instead. On the other hand, the latest version of GAUSSIAN 09 [58], recently available in our lab, finally allowed all calculations including frequency calculations using TDDFT even in larger basis sets such as aug-cc-pVTZ.

All the ab initio calculations presented here have been carried out on a Quad-core AMD Opteron^{tm} Processor 8379 HE 2.4 GHz workstation with 16 processors using the GAUSSIAN 09 and GAMESS electronic structure packages.

PA was placed on the yz plane with z as the main symmetry axis, and was constrained to C_{2v} symmetry. The labeling of the carbon atoms is 1-6 around the ring and the acetylenic portion is numbered as -C1-C7≡C8. For simplicity, hydrogen atoms 2-6 are bonded to carbon atoms 2-6 and the 14th (H8) is bonded to carbon atom 8. Fig. 2.18 displays Molecular structure of PA with the atom labeling used in the present work.

The geometry of the ground state of PA was optimized at the B3LYP/ aug-cc-pVDZ and aug-cc-pVTZ levels of theory for Gaussian 09 and Gamess calculations, respectively. The optimized geometry of the ground state of PA was used to obtain the vertical excitation energies for the singlet states of PA. Moreover, CASSCF (eight electrons in an eight-orbital active space), B3LYP and LRC-TD-DFT (LC-BLYP and CAM-B3LYP) with the aug-cc-pVDZ and aug-cc-pVTZ basis sets were used to compute vibrational frequencies, vectors and calculated electronic transitions moments.

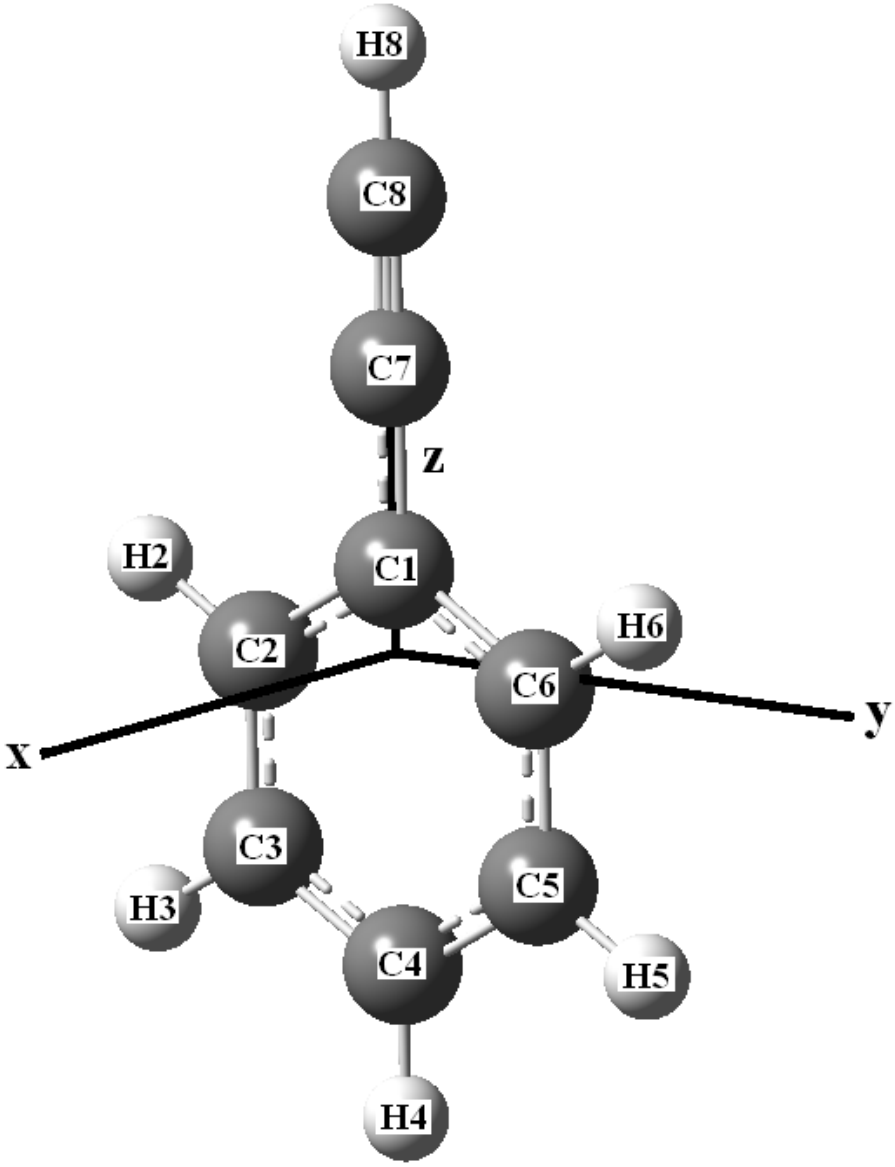

Figure 2.18: Molecular structure of PA with the atom labeling used in the present work.

In order to get the derivatives of the transition moments with respect to the vibrational mode (in Eq. 2.21), the moment components at several values along each of the normal mode coordinates $\{Q_i\}$ were calculated. Vertical excitation energies and transition moments for the singlet states of PA at a geometry displaced along the desired normal mode direction have been obtained, taking into account that the Cartesian displacement of an individual atom "j" in a mass-weighted normal mode "i" is obtained by [12]

$$x_{ij} = \left[\frac{\hbar (\nu_i + 0.5)}{\pi c \tilde{\nu}_i m_j} \right]^{1/2} q_{ij} \quad \ldots(2.25)$$

with ν_i as the vibrational quantum number, $\tilde{\nu}_i$ is the vibrational energy in wave numbers m_j is the atomic mass, and q_{ij} a Cartesian atomic displacement component of the mass-weighted normal mode vector.

To get accurate first and second derivatives of the transitions, at least two points in addition to the common point at the equilibrium geometry have to be obtained. Calculations at q_{ij} equal to +0.5 and -0.25 Bohr have been done in this work. Since different vibrational symmetries give vibronic activities along different moment directions (X, Y, Z or forbidden), it is possible to know which symmetries have all of the activity and limit the calculations to those. In the case of PA, a C_{2v} symmetry molecule, the calculations can be reduced to the analysis of the in-plane vibrations which have the strong vibronic activity. Additionally, hydrogen vibrational modes have been excluded because they do not show strong activity with the observed spectra.

Calculating points only along the fundamental vibrational coordinates should be enough in calculating the first order vibronic effects. However, the transition moments obtained present a sign ambiguity since there is arbitrariness in the sign of the wavefunctions. To overcome this problem, combination bands are necessary and have been done. The strategy for determining signs is to assume the two dimensional surface of the moments $M(Q_a, Q_b)$ for coordinates *a* and *b* is continuous as it goes through both axes, and the active moments vary almost linearly along any coordinate parallel to a principal axis. This means that if one moves Q = 0.5 away from the origin on coordinate *a*, the active moment component increases to M(0.5, 0) and then one looks at various moments along the direction parallel to the *b* axis such as M(0.5, 0.5) and M(0.5, -0.25), a straight line with a slope the same sign as the one at $Q_b = 0$ should be observed. Thus, the sign of the slope of the moment along *b* can be determined. The slope along *a* is arbitrarily set and all of the other vibrations are determined relative to it. Therefore, calculations along each of the active vibrational components and along each vibrational axis offset along the chosen reference vibration have to be done. In the case of second order effects, moment Hessian matrices (second derivatives) should be obtained and the quadratic components of the moment variations along each normal coordinate and along the diagonals between each pair of normal coordinates have to be computed using Eq. 2.21 and 2.24.

A very large number of calculations are needed for a complete spectra simulation, particularly in the case of the vibronic spectra since second order effects were included. In order to automate the process, the input files for each calculation were generated by Labview-based computer programs that wrote them in bulk and these were run with bash scripts (ziprungms2 and ziprunG09-GOOD for GAMESS and GAUSSIAN 09 jobs, respectively, and provided in Appendix A) that submitted them to the multiprocessor linux-based machine.

Intensities were calculated for every symmetry-viable vibrational level for the modes considered (in-plane, a_1 and b_2) up to about 2000 cm^{-1} (~15 000 states) for both the GAMESS and G09 simulations, respectively. This step required $\sim 10^7$ Franck-Condon factors that were provided by the MolFC program, developed and distributed by R. Borrelli and A. Poluso [59].

The amounts of CPU time required for the geometry optimizations, frequency and transition moment calculations, and the vibronic simulations of the different levels of theory and basis sets are reported in Table 2.9 and were obtained with the workstation previously described. Although the geometry and frequency calculations in this work were performed using 16 processors, the CPU timings obtained from the Gaussian 09 output files (listed in Table 2.9) are based on single processor calculations. The total CPU time required to run all the transition moment calculations at different geometries and the CPU time required to do the vibronic spectrum simulation depend on the order of vibronic effects, the number of Frank-Condon integrals and the number of frequencies calculated. In this work, the vibronic simulation up to the first order vibronic effects and to a range of 2000 cm^{-1} required 104 transition moment calculations while a simulation up to the second order required 1456 calculations.

The rotational temperature of the jet-cooled spectrum was estimated by simulating the origin and βcc band rotational contours using a Labview-based program developed in our group that used a Fortran library back end [60, 61]. Calculations were done using the rotational constants determined from fits of the rotationally resolved $S_1 \leftarrow S_0$ fluorescence excitation spectra of the 0^0 and 0^0 + 493 cm^{-1} bands of PA obtained by Ribblett et al. [35] and shown in Table 2.10.

Table 2.9: CPU time required for the geometry optimizations, frequency and transition moment calculations, and the vibronic simulations of the different levels of theory and basis sets.

State	Type of calculation		CPU Time (min)[a]					
			B3LYP		LC-BLYP		CAM-B3LYP	
			aug-cc-pVDZ	aug-cc-pVTZ	aug-cc-pVDZ	aug-cc-pVTZ	aug-cc-pVDZ	aug-cc-pVTZ
S_0	Geometry optimization		43	577	53	547	52	674
	Frequency calculation		51	1038	112	1400	109	1698
S_1	Geometry optimization		747	5650	878	10905	774	11359
	Frequency calculation		7952	61852	10208	84857	9801	97378
	Transition Moment calculation/geometry		89	849	169	1327	151	1281
	Transition Moment calculation/total number of geometries	1^{st} order vibronic effects[b]	9256	88296	17576	138008	15704	133224
		2^{nd} order vibronic effects[b]	129584	1236144	246064	1932112	219856	1865136
	Vibronic spectrum simulation		4320	5760	4320	5760	4320	5760
Total CPU time[c] (days)			6	60	12	94	11	92

a. Based on single processor calculations.

b. 1^{st} and 2^{nd} order vibronic effects required transition moments at 104 and 1456 geometries, respectively.

c. The total CPU time was calculated considering 16 processors used for each Geom. Optimization and Freq. calculation and 1 processor for each Transition moment/geometry calculation. However, 16 independent Transition moments/geometry calculations could be done since we had 16 processors available.

Table 2.10: Rotational constants determined from fits of the rotationally resolved $S_1 \leftarrow S_0$ fluorescence excitation spectra of the 0^0 and 0^0 + 493 cm^{-1} bands of PA. (S_0: ground state, S_1: first excited state).

	Ribblett et al.[35]			
	Band Origin (0^0)		**βcc band (0^0+ 493 cm^{-1})**	
Rotational Constant (cm^{-1})	**S_0**	**S_1**	**S_0**	**S_1**
A	0.1895	0.1821	0.1896	0.1835
B	0.0510	0.0502	0.0510	0.0502
C	0.0401	0.0394	0.0402	0.0394

C. Results and Discussions

The optimized molecular geometry parameters of PA in the S_0 and S_1 states calculated using various levels of the theory and basis sets are shown in Tables 2.11 and 2.12.

PA is found to be planar in both states with a symmetry point group of C_{2v}. No noticeable change is observed in any C-H bond lengths when the ground state (S_0) is excited to the S_1 state. However, increments in the C1-C2, C2-C3 and C3-C4 bond lengths have been noted. The same behavior has been observed in the calculated bond lengths in benzene and monosubstituted benzenes C_6H_5X (where X is CN, OH or NH_2) [8, 62]. As far as the acetylenic substituent is concerned, the C1-C7 bond becomes shorter and the C7≡C8 bond becomes longer in the S_1 state. It should be noted that the angle C6C1C2 decreases while all the other angles change very little. Table 2.13 gives the changes in the bond lengths and the C6C1C2 angle between the ground and S_1 states. The decrease in the substituent-sensitive C1-C7 bond length and the angle C6C1C2 plus an increase in the C1-C2 bond length in this molecule is usually attributed to increased conjugation between the C≡CH substituent and the ring.

The distance between the ring atoms C1 and C4 in the respective ground and S_1 states are also shown in Table 2.13. The increment in this distance indicates that the ring is lengthened along the C_2 symmetry axis. This feature results from the strong σ and π electron interactions between the -C≡CH and the ring and has also been observed in styrene [8]. On the other hand, the S_1 state in aniline contracts along the in-plane axis due to the strong interactions between the π electrons of the ring and the lone pair electrons of the amino group [8]. In the case of PA, the CASSCF calculations show an increased C1-C4 bond over the results of TD-DFT with the same basis set (aug-cc-pVDZ). No difference was observed when comparing the TD-functionals using aug-cc-pVDZ or aug-cc-pVTZ basis sets.

Generally, the population of antibonding orbitals causes the ring expansion in monosubstituted benzenes (C_6H_5X) when a $\pi - \pi^*$ excitation occurs, leading to some degree of ring distortion and changes in the C1-C7 bond length. This behavior can be explained by the interaction between the substituent and the π–electrons in the ring and has been confirmed by our results where the symmetric hexagonal character is slightly lost in the excited electronic state.

Table 2.11: Optimized molecular geometry parameters of PA in the S_0 and S_1 states at different levels of theory with aug-cc-pVDZ basis set.

Bond Lengths (Å)	Serrano-Andres et al.[2]		This Work							
	S_0	S_1	S_0				S_1			
	CASSCF (8,8)		CASSCF (8,8)*	B3LYP	LC BLYP	CAM-B3LYP	CASSCF (8,8)*	B3LYP	LC BLYP	CAM-B3LYP
	A.N.O.		aug-cc-pVDZ				aug-cc-pVDZ			
C1C2	1.400	1.443	1.404	1.409	1.391	1.401	1.441	1.438	1.419	1.431
C2C3	1.392	1.432	1.396	1.395	1.382	1.389	1.429	1.431	1.412	1.422
C3C4	1.394	1.424	1.399	1.399	1.385	1.393	1.419	1.416	1.408	1.414
C1C7	1.438	1.410	1.444	1.432	1.434	1.435	1.394	1.399	1.410	1.406
C7C8	1.197	1.203	1.203	1.215	1.199	1.208	1.227	1.229	1.205	1.217
C2H2	1.074	1.072	1.079	1.089	1.089	1.089	1.080	1.088	1.087	1.087
C3H3	1.074	1.073	1.080	1.090	1.089	1.089	1.081	1.089	1.088	1.088
C4H4	1.074	1.073	1.080	1.090	1.089	1.089	1.080	1.089	1.087	1.088
C8H8	1.054	1.054	1.061	1.069	1.071	1.069	1.063	1.069	1.071	1.069
C1C4	-	-	2.806	2.812	2.778	2.797	2.871	2.856	2.835	2.852
Bond Angles (deg.)										
(C1C2C3)	120.200	120.200	120.145	120.305	120.209	120.223	120.108	119.793	120.096	120.052
(C2C3C4)	120.200	120.400	120.219	120.303	120.189	120.243	120.443	120.152	120.303	120.299
(C3C4C5)	119.800	119.900	119.804	119.752	119.838	119.807	120.033	120.647	119.886	120.084
(C6C1C2)	119.500	118.900	119.469	120.032	119.366	119.260	118.864	119.462	119.314	119.213
(C1C2H2)	119.500	119.400	119.472	119.282	119.264	119.318	119.034	119.355	119.261	119.281
(C2C3H3)	119.700	119.400	119.676	119.625	119.692	119.670	119.453	119.642	119.581	119.568

* Done in GAMESS computational package [57], all other calculations from this work were done in GAUSSIAN 09 [58].

Table 2.12: Optimized molecular geometry parameters of PA in the S_0 and S_1 states at different levels of theory with aug-cc-pVTZ basis set.

	This Work					
Bond Lengths (Å)	**S_0**			**S_1**		
	B3LYP	**LC BLYP**	**CAM-B3LYP**	**B3LYP**	**LC BLYP**	**CAM-B3LYP**
	aug-cc-pVTZ			**aug-cc-pVTZ**		
C1C2	1.402	1.383	1.394	1.431	1.412	1.423
C2C3	1.387	1.374	1.382	1.423	1.405	1.415
C3C4	1.391	1.376	1.385	1.408	1.400	1.407
C1C7	1.426	1.428	1.429	1.391	1.404	1.399
C7C8	1.202	1.186	1.195	1.216	1.192	1.204
C2H2	1.081	1.080	1.082	1.079	1.079	1.078
C3H3	1.082	1.081	1.081	1.078	1.079	1.079
C4H4	1.081	1.081	1.081	1.081	1.079	1.079
C8H8	1.060	1.063	1.062	1.061	1.063	1.062
C1C4	2.796	2.762	2.782	2.841	2.819	2.837
Bond Angles (deg.)						
(C1C2C3)	120.332	120.217	120.259	119.797	120.135	120.078
(C2C3C4)	120.284	120.178	120.224	120.114	120.279	120.278
(C3C4C5)	119.783	119.862	119.833	120.725	119.916	120.123
(C6C1C2)	119.984	119.350	119.201	119.453	119.258	119.167
(C1C2H2)	119.207	119.261	119.242	119.287	119.217	119.223
(C2C3H3)	119.652	119.730	119.699	119.700	119.631	119.604

Table 2.13: Changes in the bond lengths and the (C6C1C2) angle between the ground and S_1 states

	S_1-S_0							
	Serrano et al.[2]	**This work**						
	CASSCF (8,8)	**CASSCF (8,8)***	**B3LYP**	**LC BLYP**	**CAM-B3LYP**	**B3LYP**	**LC BLYP**	**CAM-B3LYP**
	A.N.O.	**aug-cc-pVDZ**				**aug-cc-pVTZ**		
C1C2	0.043	0.037	0.029	0.028	0.030	0.029	0.029	0.029
C2C3	0.040	0.033	0.036	0.030	0.033	0.036	0.031	0.033
C3C4	0.030	0.020	0.017	0.023	0.021	0.017	0.024	0.022
C1C4	-	0.065	0.044	0.057	0.055	0.045	0.057	0.055
C1C7	-0.028	-0.050	-0.033	-0.024	-0.029	-0.035	-0.024	-0.030
C7C8	0.006	0.024	0.014	0.006	0.009	0.014	0.006	0.009
(C6C1C2)	-0.600	-0.605	-0.570	-0.052	-0.047	-0.531	-0.092	-0.034

An analysis of the charge distribution on different carbon atoms of the molecule provides another view of the reduction from the hexagonal ring structure on excitation. Change in charge distribution at the substituent carbon is certainly an indication of the stronger interaction between the two groups. The calculated total atomic charges on C1 and C7 are shown in Table 2.14 for the different levels of theory applied in this work. Based on Mulliken population analysis [63], the more negative character of C1 but especially on C7 of PA in S_1 indicates a strong interaction between the acetylenic group and the ring. The results obtained with aug-cc-pVTZ basis set indicate a stronger interaction than the ones obtained at aug-cc-pVDZ, This result was expected since aug-cc-pVTZ is a more polarizable basis set.

Table 2.14: Calculated total atomic charges (in atomic units) based on the Mulliken analysis [63] on C1 and C7 at different levels of theory.

		B3LYP	**LC BLYP**	**CAM-B3LYP**	**B3LYP**	**LC BLYP**	**CAM-B3LYP**
		aug-cc-pVDZ			**aug-cc-pVTZ**		
C1	S_0	1.025	1.143	1.088	2.009	2.007	2.017
	S_1	1.095	1.155	1.120	1.990	2.001	2.010
	S_1-S_0	0.070	0.012	0.032	-0.019	-0.006	-0.007
C7	S_0	0.003	-0.242	-0.079	0.484	0.478	0.484
	S_1	0.069	-0.243	-0.034	0.422	0.392	0.422
	S_1-S_0	0.066	0.001	0.045	-0.062	-0.086	-0.062

All the calculations from this work were done in GAUSSIAN 09 [58].

The rotational constants A and B are related to the moments of inertia about the in-plane long and short axes, respectively [8]. In the $S_1 \leftarrow S_0$ transition, the changes in the calculated rotational constants of PA are listed in Tables 2.15 and 2.16. Our calculations showed before that the C1-C4 length in the S_1 state is bigger than the corresponding length in the ground state indicating that the ring is elongated along the in-plane long axis (Z, as defined before) in the excited state. However, we observed that the rotational constant A is bigger in the S_0 state implying that the phenyl ring has not been distorted to a quinoid-like resonance structure. The other rotational constants barely changed. These results are in good agreement with those from the CASSCF (8,8)/A.N.O. obtained by Serrano-Andres et al. [2].

Table 2.15: Changes in the calculated rotational constants for the ground and first excited states of PA at different levels of theories with aug-cc-pVDZ basis set.

	Serrano et al.[2]			This work								
	CASSCF (8,8)			B3LYP			LC BLYP			CAM B3LYP		
	A.N.O.			aug-cc-pVDZ								
Rotational Constant (cm^{-1})	**S_0**	**S_1**	**S_1- S_0**	**S_0**	**S_1**	**S_1- S_0**	**S_0**	**S_1**	**S_1- S_0**	**S_0**	**S_1**	**S_1- S_0**
A	0.1910	0.1820	-0.0090	0.1888	0.1824	-0.0064	0.1925	0.1862	-0.0063	0.1903	0.1841	-0.0062
B	0.0510	0.0500	-0.0010	0.0507	0.0502	-0.0005	0.0515	0.0508	-0.0007	0.0509	0.0504	-0.0005
C	0.0400	0.0400	0.0000	0.0399	0.0394	-0.0005	0.0406	0.0399	-0.0007	0.0402	0.0395	-0.0007

Table 2.16: Changes in the calculated rotational constants for the ground and first excited states of PA at different levels of theories with aug-cc-pVTZ basis set.

	This work								
	B3LYP			LC BLYP			CAM B3LYP		
	aug-cc-pVTZ								
Rotational Constant (cm^{-1})	**S_0**	**S_1**	**S_1- S_0**	**S_0**	**S_1**	**S_1- S_0**	**S_0**	**S_1**	**S_1- S_0**
A	0.1910	0.1844	-0.0066	0.1949	0.1884	-0.0065	0.1925	0.1862	-0.0063
B	0.0513	0.0508	-0.0005	0.0521	0.0514	-0.0007	0.0516	0.0509	-0.0007
C	0.0404	0.0398	-0.0006	0.0411	0.0404	-0.0007	0.0407	0.0400	-0.0007

The calculated vibrational frequencies for PA in the S_0 state are summarized in Table 2.17 while Table 2.18 gives the calculated vibrational frequencies for S_1. The absence of imaginary frequencies in both cases (S_0 and S_1 states) indicates that, at these levels of calculation and for the low-lying excited states, the C_{2v} planar symmetry is maintained. Moreover, both cases (S_0 and S_1) have 25 in-plane normal vibration that correspond to 13 a_1 and 12 b_2; and 11 out-of-plane normal vibrations that correspond to 3 a_2 and 8 b_1.

No scaling factor was used in the calculated frequencies. In the case of the S_1 state, 0.92 was used for CASSCF (8,8) level of theory. The frequencies obtained with all the different functionals of TD-DFT for the S_1 state of PA were close to the experimental ones, especially in the lower energy part of the spectrum and no vibrational frequency scaling factor was needed.

In the $S_1 \leftarrow S_0$ transition, there is a reduction of the π-electron density in the excited state that reduces the force constants in most out-of-plane vibrations due to the transfer of electron density from bonding to antibonding orbitals as previously discussed. Thus, the frequency will decrease slightly more for the out-of-plane C-H bending vibrations as compared to the in-plane ones. This can be seen in the a_2 ($\nu_{14\text{-}16}$) and the b_1 ($\nu_{17\text{-}24}$) modes.

Table 2.17: Theoretical harmonic fundamental frequencies (cm^{-1}) for ground state of PA.

			Serrano et al.[b]		This Work						Mode Description[b]
			CASSCF (8,8)		CASSCF (8,8)		B3LYP		LC BLYP	CAM-B3LYP	
			A.N.O.		aug-cc-pVDZ						
Symm.	Mulliken	Wilson[a]	Freq.	Scaled Freq.*	Freq.	Scaled Freq.*	Freq.	Scaled Freq.**	Freq.	Freq.	
a_1	ν_1	νCH	3629	3339	3618	3328	3481	3377	3511	3494	C_8H_8 stretch
	ν_2	2	3357	3088	3360	3091	3205	3109	3261	3230	CH stretch
	ν_3	20*a*	3345	3077	3347	3079	3194	3098	3249	3218	CH stretch
	ν_4	7*a*	3322	3056	3325	3059	3175	3080	3232	3200	CH stretch
	ν_5	νCC	2313	2128	2310	2125	2205	2138	2016	2253	$C_7{}^oC_8$ stretch
	ν_6	8*a*	1728	1590	1734	1595	1642	1593	1736	1683	CCH bend
	ν_7	19*a*	1620	1490	1619	1490	1509	1463	1562	1532	CCH bend
	ν_8	13	1274	1172	1280	1177	1218	1182	1258	1234	C_1C_7 stretch, CCH bend
	ν_9	9*a*	1266	1165	1259	1159	1191	1155	1207	1199	CCH bend
	ν_{10}	18*a*	1095	1007	1098	1010	1045	1014	1081	1061	Ring deformation
	ν_{11}	12	1056	972	1060	976	1005	975	1033	1019	Ring deformation
	ν_{12}	1	802	738	777	715	772	749	793	781	Ring breath
	ν_{13}	6*a*	492	453	420	386	469	455	478	473	$C_7C_8H_8$-ring breath
a_2	ν_{14}	17*a*	991	912	979	900	984	955	1039	1008	OP CCH-ring breath
	ν_{15}	10*a*	865	796	856	788	846	820	887	864	OP CCH bend
	ν_{16}	16*a*	429	395	344	316	411	399	427	418	OP CCH bend
b_1	ν_{17}	5	1011	930	1000	920	1006	976	1067	1031	OP CCH bend
	ν_{18}	17*b*	938	863	928	854	930	902	984	953	OP CCH bend
	ν_{19}	11	777	715	806	741	777	754	816	793	OP CCH bend
	ν_{20}	4	717	660	768	707	706	685	733	718	OP CCH bend
	ν_{21}	γCH	534	491	665	612	575	558	665	609	OP ring deformation
	ν_{22}	16*b*	387	356	526	484	532	516	575	555	OP ring def, $C_7C_8H_8$ bend
	ν_{23}	γCC	344	316	292	269	344	333	366	354	OP ring def, $C_7C_8H_8$ bend
	ν_{24}	10*b*	138	127	122	112	132	128	140	136	OP ring def, $C_7C_8H_8$ bend
b_2	ν_{25}	7*b*	3355	3087	3356	3087	3201	3105	3256	3226	CH stretch
	ν_{26}	20*b*	3333	3066	3336	3069	3184	3088	3241	3209	CH stretch
	ν_{27}	8*b*	1698	1562	1704	1568	1608	1560	1703	1650	Ring deformation
	ν_{28}	19*b*	1563	1438	1560	1436	1459	1415	1508	1481	Ring deformation
	ν_{29}	14	1439	1324	1436	1321	1348	1308	1357	1352	CCH bend
	ν_{30}	3	1300	1196	1302	1198	1314	1275	1315	1321	CCH bend
	ν_{31}	9*b*	1185	1090	1186	1091	1173	1138	1177	1176	CCH bend
	ν_{32}	18*b*	1144	1052	1144	1053	1095	1063	1122	1108	CCH bend
	ν_{33}	βCH	798	734	708	651	650	630	738	685	$C_7C_8H_8$ bend
	ν_{34}	6*b*	666	613	572	526	630	611	643	636	Ring deformation
	ν_{35}	βCC	578	532	495	456	524	509	548	534	$C_1C_7C_8$ bend
	ν_{36}	15	168	155	174	160	154	150	164	158	CCH, $C_7C_8H_8$ bend

Table 2.17: cont'd

			This Work				
			B3LYP		LC BLYP	CAM-B3LYP	Mode Description[b]
			aug-cc-pVTZ				
Symm.	Mulliken	Wilson[a]	Freq.	Scaled Freq.**	Freq.	Freq.	
a_1	ν_1	νCH	3467	3363	3491	3478	C_8H_8 stretch
	ν_2	2	3198	3102	3250	3221	CH stretch
	ν_3	20*a*	3186	3090	3238	3209	CH stretch
	ν_4	7*a*	3167	3072	3221	3190	CH stretch
	ν_5	νCC	2205	2139	2315	2253	$C_7{}^oC_8$ stretch
	ν_6	8*a*	1640	1591	1733	1680	CCH bend
	ν_7	19*a*	1525	1480	1577	1548	CCH bend
	ν_8	13	1223	1187	1264	1239	C_1C_7 stretch, CCH bend
	ν_9	9*a*	1201	1165	1220	1210	CCH bend
	ν_{10}	18*a*	1050	1019	1086	1066	Ring deformation
	ν_{11}	12	1019	988	1052	1034	Ring deformation
	ν_{12}	1	777	753	799	786	Ring breath
	ν_{13}	6*a*	473	459	483	477	$C_7C_8H_8$-ring breath
a_2	ν_{14}	17*a*	997	967	1048	1019	OP CCH-ring breath
	ν_{15}	10*a*	863	837	901	880	OP CCH bend
	ν_{16}	16*a*	412	399	425	418	OP CCH bend
b_1	ν_{17}	5	1018	987	1070	1040	OP CCH bend
	ν_{18}	17*b*	946	917	994	966	OP CCH bend
	ν_{19}	11	782	759	816	797	OP CCH bend
	ν_{20}	4	710	689	743	722	OP CCH bend
	ν_{21}	γCH	645	626	735	687	OP ring deformation
	ν_{22}	16*b*	553	536	576	563	OP ring def, $C_7C_8H_8$ bend
	ν_{23}	γCC	368	357	384	375	OP ring def, $C_7C_8H_8$ bend
	ν_{24}	10*b*	141	137	148	144	OP ring def, $C_7C_8H_8$ bend
b_2	ν_{25}	7*b*	3193	3097	3245	3216	CH stretch
	ν_{26}	20*b*	3176	3080	3229	3199	CH stretch
	ν_{27}	8*b*	1609	1561	1702	1650	Ring deformation
	ν_{28}	19*b*	1477	1433	1525	1498	Ring deformation
	ν_{29}	14	1358	1317	1377	1367	CCH bend
	ν_{30}	3	1311	1272	1303	1312	CCH bend
	ν_{31}	9*b*	1183	1148	1184	1186	CCH bend
	ν_{32}	18*b*	1102	1069	1131	1115	CCH bend
	ν_{33}	βCH	688	668	772	723	$C_7C_8H_8$ bend
	ν_{34}	6*b*	637	618	652	644	Ring deformation
	ν_{35}	βCC	538	522	561	547	$C_1C_7C_8$ bend
	ν_{36}	15	159	155	167	162	CCH, $C_7C_8H_8$ bend

[a.] The symbol ν indicates a stretch, β means an in-plane bend, and γ means an out-of-plane bend.
[b.] Serrano-Andres et.al. [2]. The descriptions are the main contributions to the normal modes. The acetylene carbons are 7 and 8, C_7 is attached to the ring at C_1, while a lack of atom numbering indicates the H or C belongs to the phenyl ring. *Scaling Factor: 0.92 **Scaling Factor: 0.97

Table 2.18: Theoretical harmonic fundamental frequencies (cm^{-1}) for the first excited singlet state (S_1) of PA.

			Serrano et al.[b]		This Work					Mode Description[b]
			CASSCF (8,8)		CASSCF (8,8)		B3LYP	LC BLYP	CAM-B3LYP	
			A.N.O.		aug-cc-pVDZ					
Symm.	Mulliken	Wilson[a]	Freq.	Scaled Freq.*	Freq.	Scaled Freq.*	Freq.	Freq.	Freq.	
a_1	ν_1	νCH	3624	3334	3614	3325	3475	3510	3490	C_8H_8 stretch
	ν_2	2	3376	3106	3379	3109	3226	3283	3250	CH stretch
	ν_3	20*a*	3363	3094	3364	3095	3211	3270	3237	CH stretch
	ν_4	7*a*	3342	3075	3345	3078	3190	3255	3220	CH stretch
	ν_5	νCC	2213	2036	2208	2032	2115	2270	2187	$C_7{}^oC_8$ stretch
	ν_6	8*a*	1666	1533	1672	1539	1543	1672	1609	CCH bend
	ν_7	19*a*	1535	1412	1531	1408	1453	1502	1473	CCH bend
	ν_8	13	1253	1153	1251	1151	1223	1255	1237	C_1C_7 stretch, CCH bend
	ν_9	9*a*	1230	1132	1226	1128	1163	1188	1177	CCH bend
	ν_{10}	18*a*	1019	937	1022	940	996	1031	1008	Ring deformation
	ν_{11}	12	972	894	976	898	973	1005	988	Ring deformation
	ν_{12}	1	750	690	752	692	740	754	745	Ring breath
	ν_{13}	6*a*	449	413	449	413	399	417	408	$C_7C_8H_8$-ring breath
a_2	ν_{14}	17*a*	697	641	678	624	747	842	794	OP CCH-ring breath
	ν_{15}	10*a*	615	566	602	554	609	672	643	OP CCH bend
	ν_{16}	16*a*	296	272	288	265	240	267	264	OP CCH bend
b_1	ν_{17}	5	739	680	724	666	852	893	856	OP CCH bend
	ν_{18}	17*b*	656	604	639	588	740	797	762	OP CCH bend
	ν_{19}	11	586	539	573	527	586	625	603	OP CCH bend
	ν_{20}	4	522	480	504	464	501	616	532	OP CCH bend
	ν_{21}	γCH	435	400	422	388	420	521	493	OP ring deformation
	ν_{22}	16*b*	321	295	301	277	399	368	378	OP ring def, $C_7C_8H_8$ bend
	ν_{23}	γCC	286	263	174	160	263	273	265	OP ring def, $C_7C_8H_8$ bend
	ν_{24}	10*b*	119	109	100	92	96	102	98	OP ring def, $C_7C_8H_8$ bend
b_2	ν_{25}	7*b*	3372	3102	3373	3103	3221	3277	3244	CH stretch
	ν_{26}	20*b*	3352	3084	3354	3085	3199	3257	3224	CH stretch
	ν_{27}	8*b*	1824	1678	1830	1684	1508	1759	1589	Ring deformation
	ν_{28}	19*b*	1612	1483	1619	1490	1432	1631	1543	Ring deformation
	ν_{29}	14	1490	1371	1485	1366	1389	1436	1411	CCH bend
	ν_{30}	3	1391	1280	1386	1275	1292	1327	1312	CCH bend
	ν_{31}	9*b*	1242	1143	1233	1134	1159	1181	1171	CCH bend
	ν_{32}	18*b*	1007	926	1012	931	1006	1067	1037	CCH bend
	ν_{33}	βCH	782	719	769	708	622	730	670	$C_7C_8H_8$ bend
	ν_{34}	6*b*	607	558	608	559	569	583	575	Ring deformation
	ν_{35}	βCC	558	513	556	511	453	456	436	$C_1C_7C_8$ bend
	ν_{36}	15	156	144	173	160	150	153	150	CCH, $C_7C_8H_8$ bend

Table 2.18: cont'd

			Serrano et al.[b]		This Work					
			CASSCF (8,8)		MCSCF (8,8)		B3LYP	LC BLYP	CAM-B3LYP	Mode Description[b]
			A.N.O.		aug-cc-pVTZ					
Symm.	Mulliken	Wilson[a]	Freq.	Scaled Freq.*	Freq.	Scaled Freq.*	Freq.	Freq.	Freq.	
a_1	ν_1	νCH	3624	3334	3614	3325	3461	3488	3474	C_8H_8 stretch
	ν_2	2	3376	3106	3379	3109	3219	3270	3241	CH stretch
	ν_3	20*a*	3363	3094	3364	3095	3204	3258	3229	CH stretch
	ν_4	7*a*	3342	3075	3345	3078	3183	3242	3211	CH stretch
	ν_5	νCC	2213	2036	2208	2032	2111	2267	2184	$C_7{}^oC_8$ stretch
	ν_6	8*a*	1666	1533	1672	1539	1543	1668	1607	CCH bend
	ν_7	19*a*	1535	1412	1531	1408	1471	1517	1490	CCH bend
	ν_8	13	1253	1153	1251	1151	1228	1260	1242	C_1C_7 stretch, CCH bend
	ν_9	9*a*	1230	1132	1226	1128	1172	1201	1188	CCH bend
	ν_{10}	18*a*	1019	937	1022	940	1001	1035	1014	Ring deformation
	ν_{11}	12	972	894	976	898	982	1020	998	Ring deformation
	ν_{12}	1	750	690	752	692	744	759	748	Ring breath
	ν_{13}	6*a*	449	413	449	413	403	421	412	$C_7C_8H_8$-ring breath
a_2	ν_{14}	17*a*	697	641	678	624	752	842	806	OP CCH-ring breath
	ν_{15}	10*a*	615	566	602	554	635	688	654	OP CCH bend
	ν_{16}	16*a*	296	272	288	265	240	271	251	OP CCH bend
b_1	ν_{17}	5	739	680	724	666	860	895	856	OP CCH bend
	ν_{18}	17*b*	656	604	639	588	749	806	773	OP CCH bend
	ν_{19}	11	586	539	573	527	604	702	622	OP CCH bend
	ν_{20}	4	522	480	504	464	531	630	618	OP CCH bend
	ν_{21}	γCH	435	400	422	388	505	524	508	OP ring deformation
	ν_{22}	16*b*	321	295	301	277	405	373	381	OP ring def, $C_7C_8H_8$ bend
	ν_{23}	γCC	286	263	174	160	302	296	292	OP ring def, $C_7C_8H_8$ bend
	ν_{24}	10*b*	119	109	100	92	99	109	93	OP ring def, $C_7C_8H_8$ bend
b_2	ν_{25}	7*b*	3372	3102	3373	3103	3214	3264	3236	CH stretch
	ν_{26}	20*b*	3352	3084	3354	3085	3193	3245	3215	CH stretch
	ν_{27}	8*b*	1824	1678	1830	1684	1504	1743	1580	Ring deformation
	ν_{28}	19*b*	1612	1483	1619	1490	1430	1630	1536	Ring deformation
	ν_{29}	14	1490	1371	1485	1366	1409	1457	1434	CCH bend
	ν_{30}	3	1391	1280	1386	1275	1308	1349	1331	CCH bend
	ν_{31}	9*b*	1242	1143	1233	1134	1171	1196	1185	CCH bend
	ν_{32}	18*b*	1007	926	1012	931	1008	1072	1041	CCH bend
	ν_{33}	βCH	782	719	769	708	661	764	708	$C_7C_8H_8$ bend
	ν_{34}	6*b*	607	558	608	559	578	593	583	Ring deformation
	ν_{35}	βCC	558	513	556	511	464	470	448	$C_1C_7C_8$ bend
	ν_{36}	15	156	144	173	160	155	157	154	CCH, $C_7C_8H_8$ bend

[a.] The symbol ν indicates a stretch, β means an in-plane bend, and γ means an out-of-plane bend.
[b.] Serrano-Andres et.al. [2]. The descriptions are the main contributions to the normal modes. The acetylene carbons are 7 and 8, C_7 is attached to the ring at C_1, while a lack of atom numbering indicates the H or C belongs to the phenyl ring. *Scaling Factor: 0.92

Table 2.19 shows the equilibrium transition moments for the $S_1 \leftarrow S_0$ transition of PA using the different LRC-TD-DFT functionals and basis sets used in this work and compares them with those previously obtained [27]. Of particular note, it is seen that the LRC functional CAM-B3LYP calculated an equilibrium transition moment five times larger than B3LYP while LC-BLYP calculated an equilibrium transition moment twice bigger than CAM-B3LYP. This has a big effect in the calculated intensity of the a_1 vibrations, including the band origin, since the Franck-Condon factors (FCF) partition this value into the strength of all of them, as shown in Eqs. 2.20 and 2.25 for these bands. This change between using the normal and the LRC functionals has the largest effect on the quality of the simulated spectrum, even though it has nothing to do with vibronic coupling. Although the vibrational vectors from the MCSCF(8,8) calculations were used in our previous work [27], the electronic transition moments were obtained with TD-DFT and the value of the equilibrium transition moment is, not surprisingly, close to our recent TD-DFT (B3LYP) value.

$$I_{ul} \sim | M_{ul} |^2 \quad \ldots(2.25)$$

$$I_{nl}^{a_1} = ((Equilibrium T.M.)(FCIntegral_{nl}) + vibronic effects)^2 \ldots(2.26)$$

where n is the number of quanta in the lower (l) state.

The variations of the y-polarized (in-plane, perpendicular to the acetylene axis) transition moments along some of the normal coordinates are displayed in Fig. 2.19. This is the active polarization for the allowed component of the electronic transition. All the curves are found to be approximately linear for the a_1 vibrations and parabolic for all others and they cross the equilibrium geometry at an offset that is the purely allowed value since a_1 is the inducing symmetry for this polarization. The derivatives of the transition moments along these vibrational

modes are obtained by fitting the curves to a second order polynomial function and determining the sign of the derivatives of these moments is straight forward since there is an offset at the origin. Similarly to the case of the a_1 vibrations, the z-polarized curves for the b_2 vibrations are found to be linear since b_2 is the inducing symmetry for this polarization. The fact that significant parabolic curvature appears, illustrates why first and second order effects are comparable for some bands and thus the need to go to second order in vibronic treatment. Indeed, the derivatives are also obtained fitting the curves to a second order polynomial function. However, determining the sign of the slope of these vibrations requires the analysis of combination bands. The strategy to do this calculation was explained in part B of this section.

Table 2.19: Equilibrium transition moments for the $S_1 \leftarrow S_0$ transition of PA at the different functionals and basis sets used in this work, with comparison to previous work [27].

Level of theory		**Basis set**	**Equilibrium Transition Moment**
CASSCF/TD-DFT(B3LYP)[a]		aug-cc-pVDZ	0.0119
TD-DFT	B3LYP		0.0140
	LC-BLYP		0.0907
	CAM-B3LYP		0.0669
	B3LYP	aug-cc-pVTZ	0.0113
	LC-BLYP		0.0888
	CAM-B3LYP		0.0651

[a.] Ref. [27]

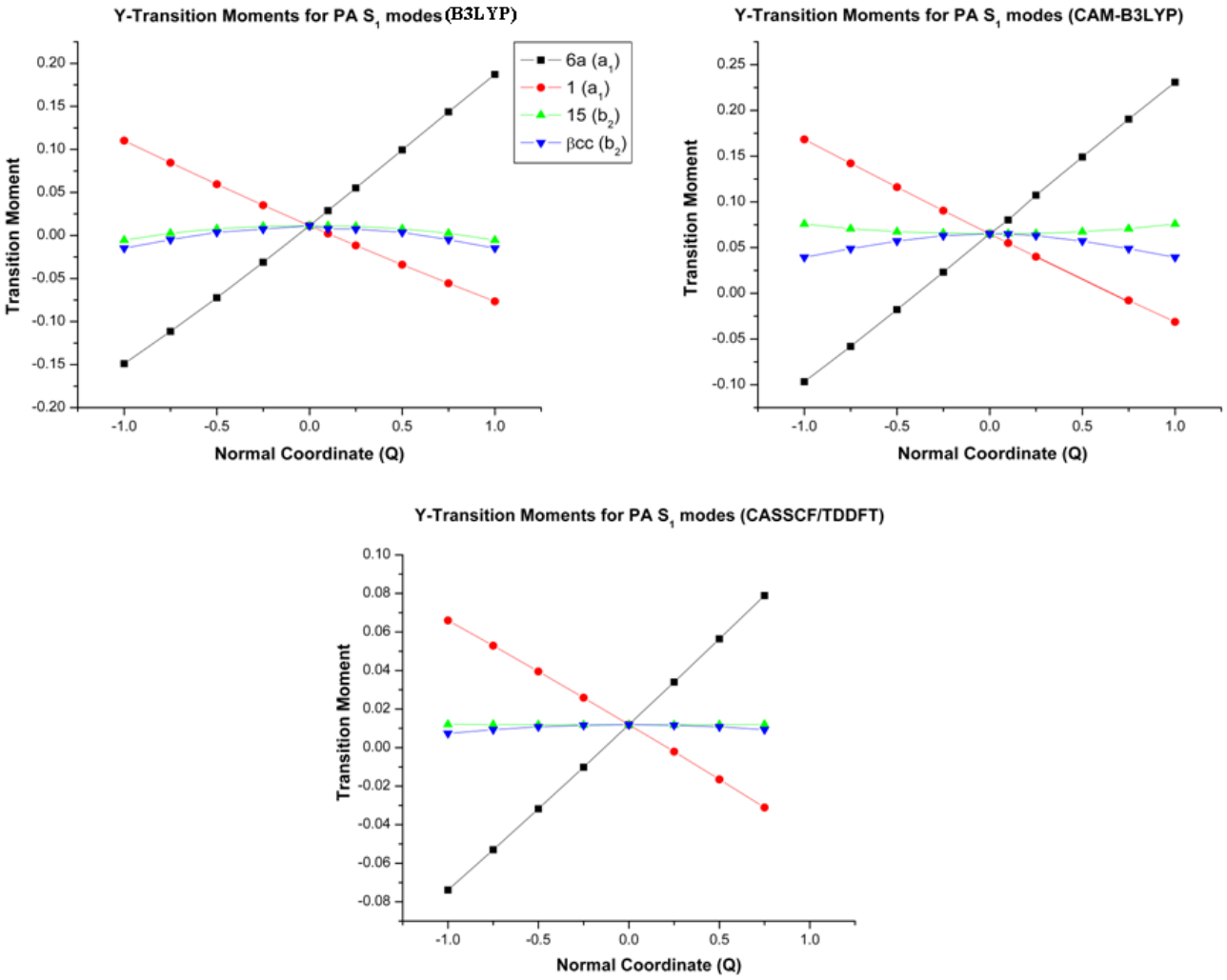

Figure 2.19: y-transition moments for various vibrational modes at the different levels of theory as a function of the normal coordinate position. a_1 symmetry modes are linear, while the b_2 have a quadratic dependence on Q. (B3LYP: is in the time dependent approach)

Table 2.20 gives the values of the first derivatives obtained for different a_1 and b_2 vibrational modes. From our results up to the first order terms of the Taylor's expansion of the transition moment shown in Fig. 2.20, it is clear after a visual inspection that CAM-B3LYP provided a more accurate prediction of the spectrum than LC-BLYP and B3LYP, especially in the calculation of the band origin intensity. Because of this, and for the purposes of this work, it was decided to include the second order terms only in the calculations done at CAM-B3LYP.

Fig. 2.21 (a, b) compares the results from the simulations done including first and second order vibronic effects for CAM-B3LYP/aug-cc-pVDZ and aug-cc-pVTZ, respectively. Apparently, the second order vibronic effects do not equally affect the different modes in the transition. Contrary to previous observations [27], it can be seen that the second order contribution decreased the intensity of the band origin, probably due to the big difference in the calculation of the equilibrium transition moment.

Table 2.20: First derivatives for a_1 (y-polarized) and b_2 (z-polarized) vibrational modes.

	Band	CASSCF-TDDFT[27]	TD-DFT				
			B3LYP	LC-BLYP	CAM-B3LYP	B3LYP	CAM-B3LYP
			aug-cc-pVDZ			aug-cc-pVTZ	
Symm.		**Y-polarized Transition Moment Derivatives**					
a_1	6a	0.0880	0.1721	0.1591	0.1668	0.1693	0.1656
	1	-0.0560	-0.0926	-0.1001	-0.0985	-0.0934	-0.0999
	12	-0.0056	-0.0067	-0.0052	-0.0064	-0.0054	-0.0053
	18a	-0.0115	-0.0101	-0.0061	-0.0080	-0.0136	-0.0113
	9a	0.0044	0.0221	0.0139	0.0159	0.0240	0.0152
	13	0.0226	0.0318	0.0283	0.0279	0.0318	0.0274
	19a	-0.0050	-0.0117	-0.0140	-0.0106	-0.0107	-0.0094
	8a	0.0262	0.0458	0.1814	0.0217	0.0454	0.0228
		Z-polarized Transition Moment Derivatives					
b_2	15	0.0623	0.1135	0.3225	0.2456	0.1340	0.2288
	βCC	0.3452	0.7463	0.7519	0.8598	0.6637	0.8376
	6b	0.1520	0.1630	0.3017	0.1757	-0.1318	-0.1296
	βCH	0.0111	0.0260	0.2975	0.1527	0.0389	0.0236
	18b	0.0477	0.0682	0.3006	0.1576	-0.0751	-0.0480
	9b	0.1180	0.2018	0.3009	0.1562	-0.2148	-0.1033
	3	0.0823	0.1513	0.3035	0.1612	0.1730	0.0265
	14	0.0116	0.0836	0.3043	0.1616	-0.1320	0.0600
	19b	0.2680	0.2233	0.2989	0.1515	0.1161	0.0794
	8b	0.0445	0.4014	0.2977	0.2561	-0.4012	-0.2675

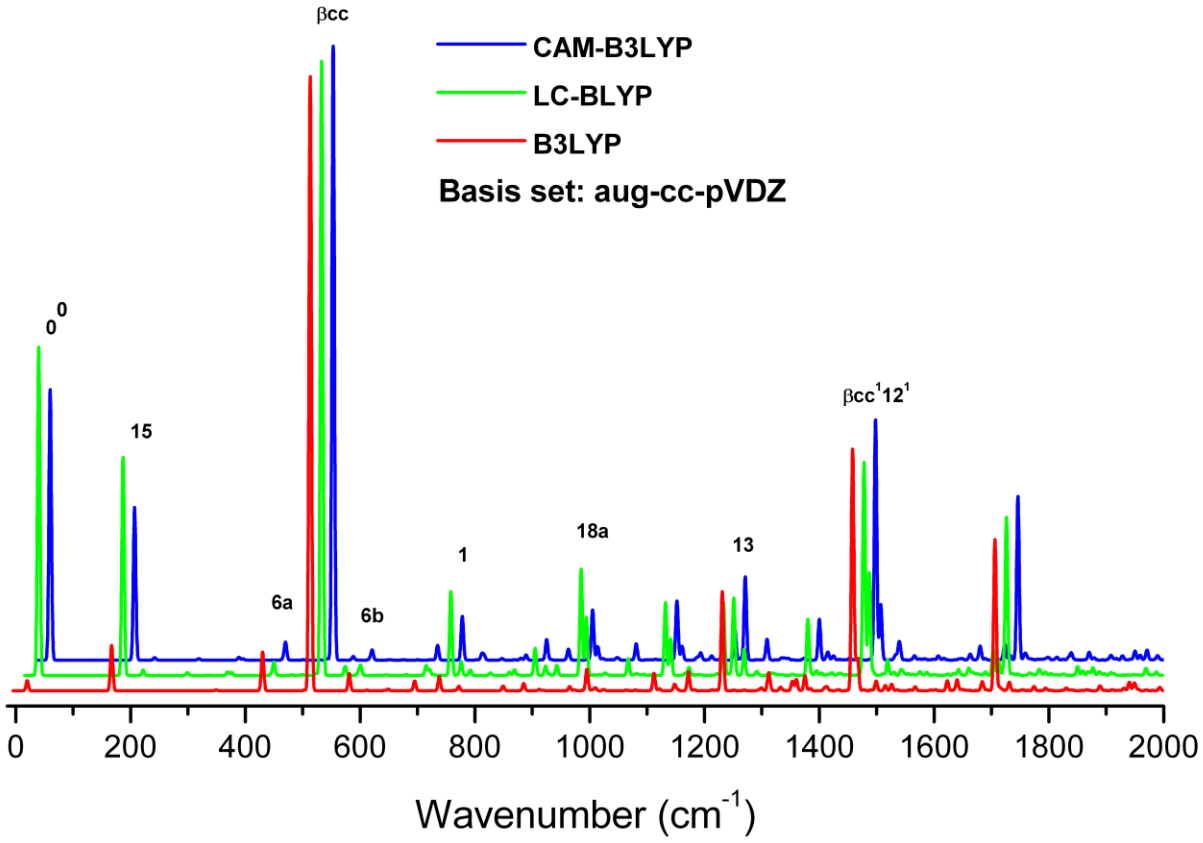

Figure 2.20: Simulation of the S_1 spectrum of PA up to the first order term of the Taylor's expansion of the transition moment done with the functionals of TD-DFT at aug-cc-pVDZ basis set. Spectra are scaled to make the βcc bands equal in height.

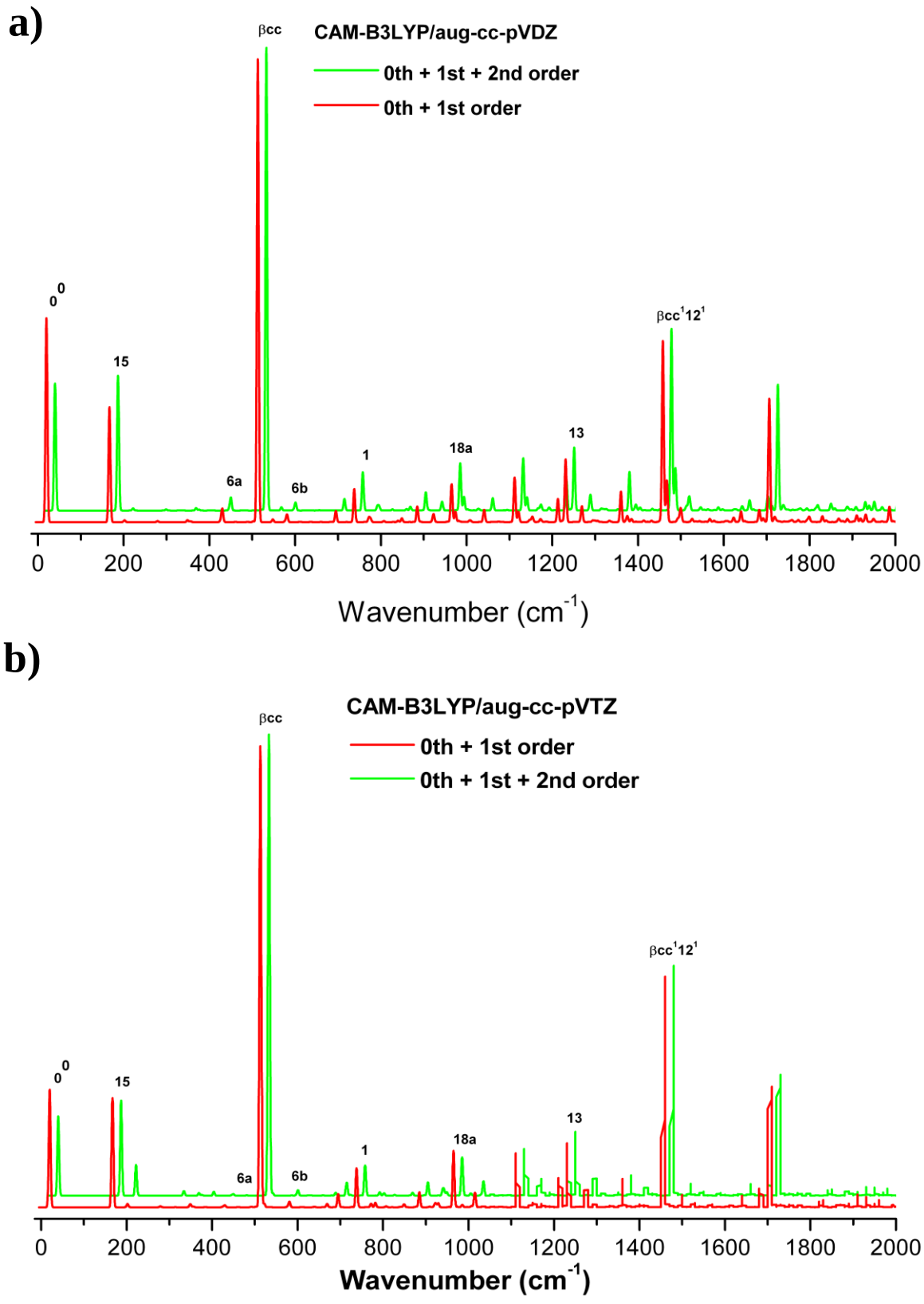

Figure 2.21: Comparison between simulated spectra done including (a) CAM-B3LYP/aug-cc-pVDZ. (b) CAM-B3LYP/aug-cc-pVTZ. Spectra are scaled to make the βcc bands equal in height.

IV. Comparison between experimental and theoretical results

Calculated bond lengths and angles for the optimized geometries of the S_0 state are in good agreement with experimental values [19], shown in Tables 2.21 and 2.22.

Table 2.21: Experimental and Theoretical geometrical parameters for the S_0 and S_1 states of PA obtained with aug-cc-pVDZ basis set.

	Experiment	**Theory**									
	Cox et al.[64]	Serrano-Andres et al. [2]		This Work							
Bond Lengths (Å)	S_0	S_0	S_1	S_0				S_1			
		CASSCF (8,8)		CASSCF (8,8)*	B3LYP	LC BLYP	CAM-B3LYP	CASSCF (8,8)*	B3LYP	LC BLYP	CAM-B3LYP
C1C2	1.388	1.400	1.443	1.404	1.409	1.391	1.401	1.441	1.438	1.419	1.431
C2C3	1.396	1.392	1.432	1.396	1.395	1.382	1.389	1.429	1.431	1.412	1.422
C3C4	1.398	1.394	1.424	1.399	1.399	1.385	1.393	1.419	1.416	1.408	1.414
C1C7	1.448	1.438	1.410	1.444	1.432	1.434	1.435	1.394	1.399	1.410	1.406
C7C8	1.208	1.197	1.203	1.203	1.215	1.199	1.208	1.227	1.229	1.205	1.217
C2H2		1.074	1.072	1.079	1.089	1.089	1.089	1.080	1.088	1.087	1.087
C3H3		1.074	1.073	1.080	1.090	1.089	1.089	1.081	1.089	1.088	1.088
C4H4		1.074	1.073	1.080	1.090	1.089	1.089	1.080	1.089	1.087	1.088
C8H8	1.055	1.054	1.054	1.061	1.069	1.071	1.069	1.063	1.069	1.071	1.069
C1C4		-	-	2.806	2.812	2.778	2.797	2.871	2.856	2.835	2.852
Bond Angles (deg.)											
(C1C2C3)	119.8	120.200	120.200	120.145	120.305	120.209	120.223	120.108	119.793	120.096	120.052
(C2C3C4)	119.9	120.200	120.400	120.219	120.303	120.189	120.243	120.443	120.152	120.303	120.299
(C3C4C5)	119.9	119.800	119.900	119.804	119.752	119.838	119.807	120.033	120.647	119.886	120.084
(C6C1C2)	119.8	119.500	118.900	119.469	120.032	119.366	119.260	118.864	119.462	119.314	119.213
(C1C2H2)	-	119.500	119.400	119.472	119.282	119.282	119.318	119.034	119.355	119.261	119.281
(C2C3H3)	-	119.700	119.400	119.676	119.625	119.692	119.670	119.453	119.642	119.581	119.568

* Done in GAMESS computational package [57], all other calculations were done in GAUSSIAN 09 [58]

Table 2.22: Experimental and Theoretical geometrical parameters for the S_0 and S_1 states of PA obtained with aug-cc-pVTZ basis set.

	Experiment	**Theory**									
	Cox et al.[64]	Serrano-Andres et al. [2]		This Work							
Bond Lengths (Å)	S_0	S_0	S_1	S_0				S_1			
		CASSCF (8,8)		CASSCF (8,8)*	B3LYP	LC BLYP	CAM-B3LYP	CASSCF (8,8)*	B3LYP	LC BLYP	CAM-B3LYP
C1C2	1.388	1.400	1.443	1.404	1.402	1.383	1.394	1.441	1.431	1.412	1.423
C2C3	1.396	1.392	1.432	1.396	1.387	1.374	1.382	1.429	1.423	1.405	1.415
C3C4	1.398	1.394	1.424	1.399	1.391	1.376	1.385	1.419	1.408	1.400	1.407
C1C7	1.448	1.438	1.410	1.444	1.426	1.428	1.429	1.394	1.391	1.404	1.399
C7C8	1.208	1.197	1.203	1.203	1.202	1.186	1.195	1.227	1.216	1.192	1.204
C2H2		1.074	1.072	1.079	1.081	1.080	1.082	1.080	1.079	1.079	1.078
C3H3		1.074	1.073	1.080	1.082	1.081	1.081	1.081	1.078	1.079	1.079
C4H4		1.074	1.073	1.080	1.081	1.081	1.081	1.080	1.081	1.079	1.079
C8H8	1.055	1.054	1.054	1.061	1.060	1.063	1.062	1.063	1.061	1.063	1.062
C1C4		-	-	2.806	2.796	2.762	2.782	2.871	2.841	2.819	2.837
Bond Angles (deg.)											
(C1C2C3)	119.8	120.200	120.200	120.145	120.332	120.217	120.259	120.108	119.797	120.135	120.078
(C2C3C4)	119.9	120.200	120.400	120.219	120.284	120.178	120.224	120.443	120.114	120.279	120.278
(C3C4C5)	119.9	119.800	119.900	119.804	119.783	119.862	119.833	120.033	120.725	119.916	120.123
(C6C1C2)	119.8	119.500	118.900	119.469	119.984	119.350	119.201	118.864	119.453	119.258	119.167
(C1C2H2)		119.500	119.400	119.472	119.207	119.261	119.242	119.034	119.287	119.217	119.223
(C2C3H3)		119.700	119.400	119.676	119.652	119.730	119.699	119.453	119.700	119.631	119.604

* Done in GAMESS computational package [57], all other calculations were done in GAUSSIAN 09 [58]

This is the most thorough vibronic calculation that has been done for a medium-sized aromatic molecule and it has been compared to the experimental spectrum in detail. While the agreement between the experimental and theoretical intensities are not perfect, it is quite reasonable given the uncertainties in both and allows vibrational assignments for the higher energy part of the spectrum to be made with much more confidence.

Experimentally, for more isolated lines, photoelectron imaging spectroscopy gave some valuable additional information to aid in assignments. There are also, not surprisingly, some indications of nonlinearities in the resonance ionization experiment, in that some of the weak lines show up with unexpected strength in the REMPI spectrum. CRD spectroscopy overcomes this deficiency and the experimental and theoretical spectra are compared below.

For the calculation of individual peak intensities of an allowed transition with vibronic character, the results showed that including second-order terms has a significant effect. Further improvements in the usefulness of the calculations could be made by incorporating the effects of Fermi resonance, anharmonicity, and Born-Oppenheimer state coupling. It is also clear that if one wishes to reproduce the intensity of the weaker bands, Coriolis effects should be taken into account when appropriate.

The rotational contour simulation of the origin leads to an estimate of 35 878.1 cm^{-1} for the electronic band origin. This value is close to the 35 877.18 cm^{-1} measured by Ribblett et al.[35] and to the 35 875 cm^{-1} obtained by Chang et al. [27].

As noted, one of the features in the allowed bands in the spectrum is the lack of prominent central Q-branches. The modes 15, 6a, βCC, 6b and 1, appear as the strong bands in the spectrum below 1000 cm^{-1}. The vibrational energies of these modes are 147, 410, 493, 561 and 718 cm^{-1}, respectively. In agreement with Chang et al.'s measurements [27] using 1+1

REMPI, we find the vibrational mode βCC (b_2 symmetry) is the strongest band in this spectrum since it has the most vibronic intensity. The results presented here show that, even for the allowed a_1 vibrations, most of the intensity comes from vibronic coupling. This is most likely the case for many other monosubstituted benzenes as well, indicating that Franck-Condon factors and calculated oscillator strengths are not useful by themselves for determining the optical spectra of this class of compounds.

Fig. 2.22 (a, b) shows a comparison of a section of the CRD spectrum, the computed spectrum obtained with CAM-B3LYP/aug-cc-pVDZ including second order vibronic effects in this work and Chang et al.'s simulated spectrum that also included second order vibronic effects [27]. As shown in Fig. 2.21b, the comparison of the vibronic results from Chang et al.'s to the CRD spectrum was satisfactory for most part when the a_1 modes were scaled up by an arbitrary factor of 3.5, the same factor used to get a good agreement with the 1+1 REMPI spectrum. The need for a correction factor may be related to the fact that the wave-functions of the S_1 and S_2 states obtained with the regular functional of TD-DFT (B3LYP) are not reliable since this functional gives serious errors both in the energy calculations of these states and their vibronic interactions. To take into account these possible artifacts, we recently simulated the vibronic spectrum of the S_1 state of PA and found that the spectrum obtained with TD-DFT functional/aug-cc-pVDZ was similar to Chang et al.'s spectrum. However, using CAM-B3LYP (a long-range corrected functional in TD-DFT) gives a more accurate result without the need for any correction factor.

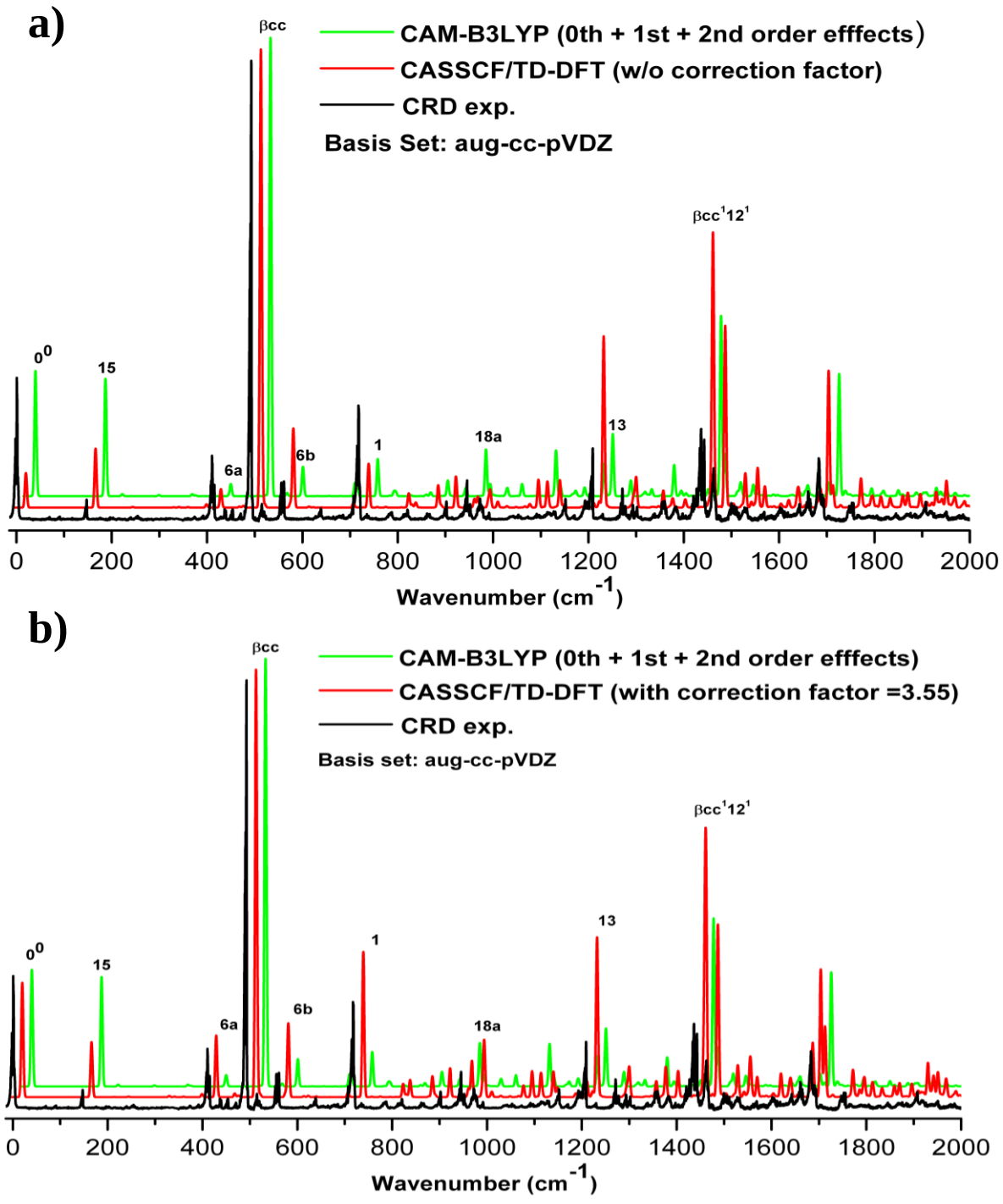

Figure 2.22: a) Comparison of a section of the CRD and calculated spectra up to 2000 cm^{-1}, the computed spectrum obtained with CAM-B3LYP/aug-cc-pVDZ including second order vibronic effects in this work and Chang et al.'s simulated spectrum that also included second order vibronic effects [27]. b) Similar to (a) but Chang et al.'s simulated spectrum includes a correction factor (3.55) applied to the a_1 modes in this case. Spectra are scaled to make the βcc bands equal in height.

Comparing our results done up to the first order terms of the Taylor's expansion of the transition moment at different TD-DFT functionals but with the same basis set (aug-cc-pVDZ) to our CRD results (Fig. 2.23), it is visually clear that CAM-B3LYP provided a more accurate prediction of the spectrum than B3LYP or LC-BLYP, especially in the calculation of the band origin intensity, and as mentioned in the previous section, for this reason, we decided to include the second order terms only in the calculations done at CAM-B3LYP. Moreover, when the two different basis sets used in this work with CAM-B3LYP up to the second order vibronic effects where compared to the CRD spectrum (Fig. 2.24), we realized that using a large basis set like aug-cc-pVTZ did not significantly improve our results but does make the calculations much more expensive and time consuming.

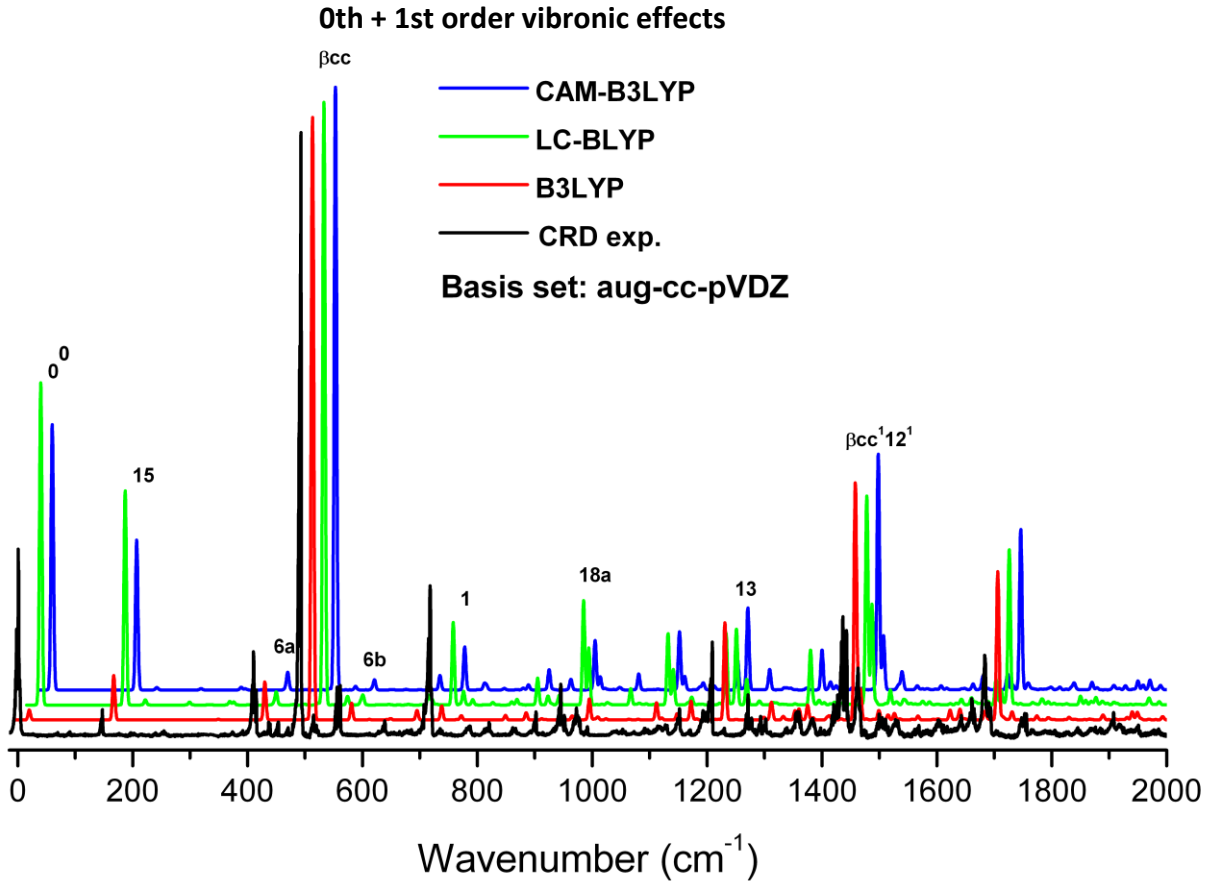

Figure 2.23: Simulation of the S_1 spectrum of PA up to the first order term of the Taylor's expansion of the transition moment done with the functionals of TD-DFT at aug-cc-pVDZ basis set. Spectra are scaled to make the βcc bands equal in height.

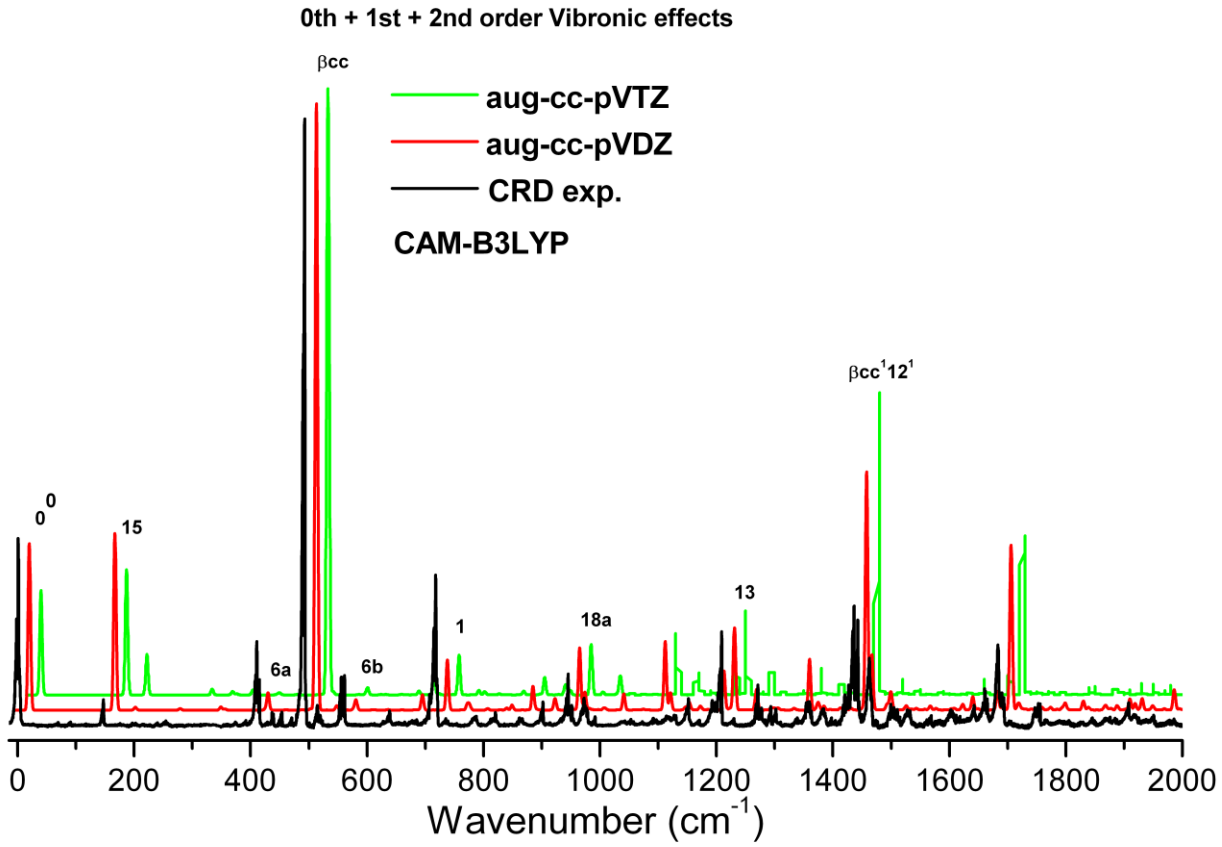

Figure 2.24: Comparison between the simulated spectrum of the S_1 spectrum of PA up to the second order term of the Taylor's expansion of the transition moment done with CAM-B3LYP at two different basis sets: aug-cc-pVDZ and aug-cc-pVTZ with the CRD spectrum. Spectra are scaled to make the βcc bands equal in height.

Fig. 2.25 shows the comparison of our simulated spectra to the CRD spectra including first (in red) and first plus second vibronic effects (in green) calculated with CAM-B3LYP/aug-cc-pVDZ to the CRD spectrum. Since a visual comparison depends entirely on peak heights, but the calculated vibronic intensity represent the peak area, for a proper visual examination the calculated peaks must be adjusted for the peak-to-area ratio of the rotational contours.

The temperature of the slit jet-cooled PA has been predicted by comparing rotational contour simulations previously described with our CRD spectrum. The temperature was found to be in the range of 30 ± 5K and the appearance of multiple hot-bands to the red of the band origin showed that the vibrational cooling is much less than the rotational cooling. Fig. 2.26 shows the comparison between PA spectra in the region near the band origin (a_1 symmetry vibration leading to type-b rotational selection rules) and the strong βCC band at ν^0_0 + 493 cm^{-1} (b_2 symmetry band leading to type-a rotational selection rules) simulated at different temperatures with the rotational constants reported previously in Table 2.10.

From 30K rotational simulations (Fig. 2.27) , it is found that the peak-to-area ratio of the b_2 bands is 1.47 times the a_1 bands, so the simulated spectrum was corrected by multiplying the a_1 y-polarized modes by the area correction factor of 1.47 (Fig. 2.25, blue line). This substantially improves the visual agreement between the experimental and simulated spectra as shown in Fig. 2.25 and 2.28.

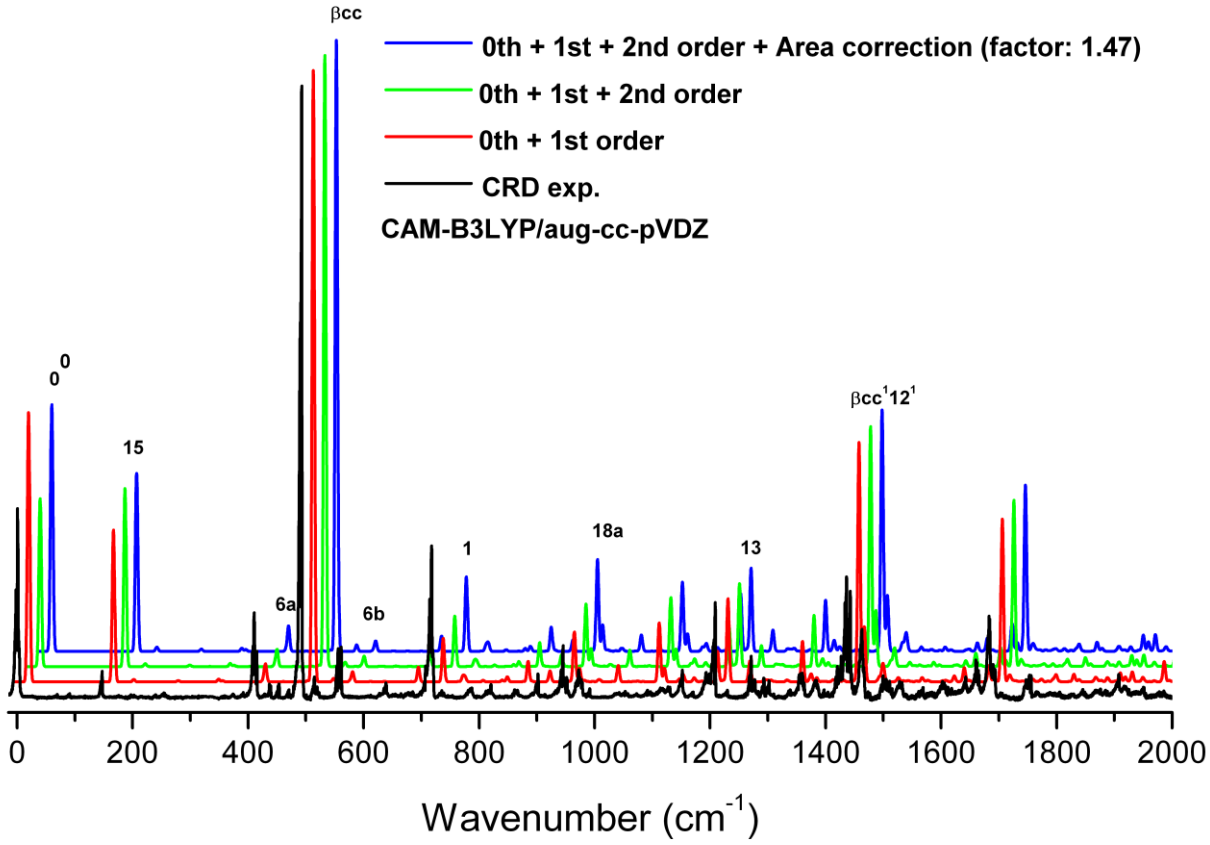

Figure 2.25: Comparison between the CRD spectrum (black) and the simulations done including first (red) and second order (green) vibronic effects done with CAM-B3LYP/aug-cc-pVDZ. (Blue) includes also the area correction factor to the a_1 y-polarized modes. Spectra are scaled to make the βcc bands equal in height.

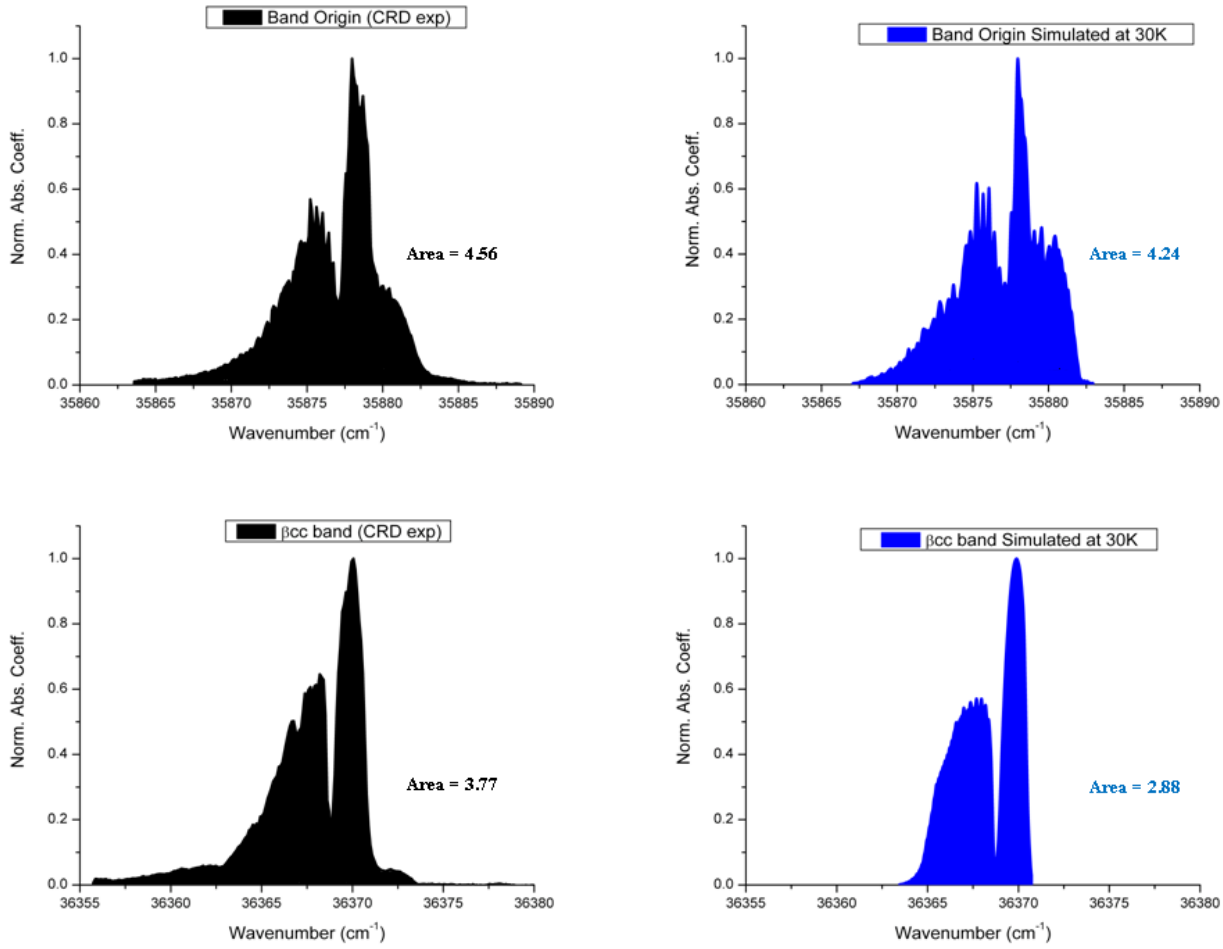

Figure 2.26: Area under the curve of the experimental and simulated (at 30K) band origin and the strongest band (βcc) in the lower part of the spectra of S_1 PA.

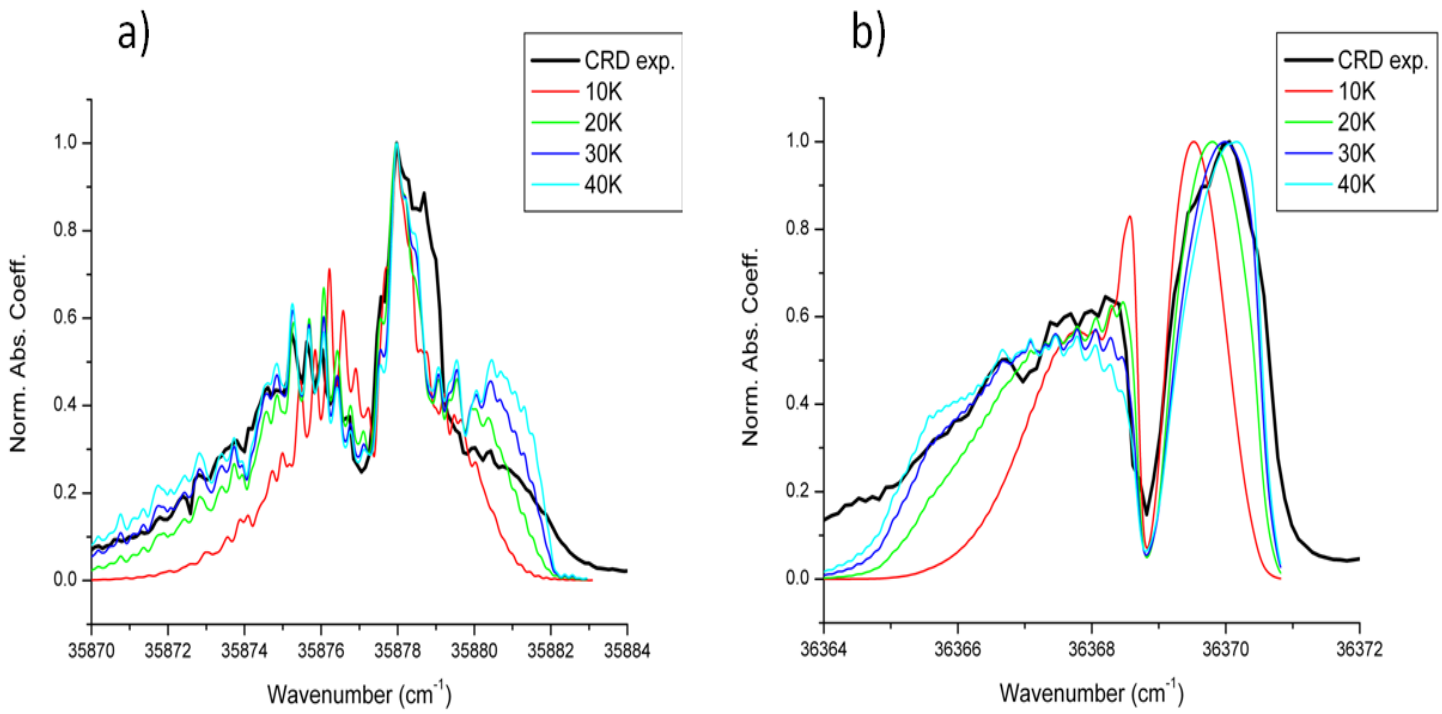

Figure 2.27: Comparison between the rotational band contours simulated at different temperatures and the experimental a) band origin and b) βCC band.

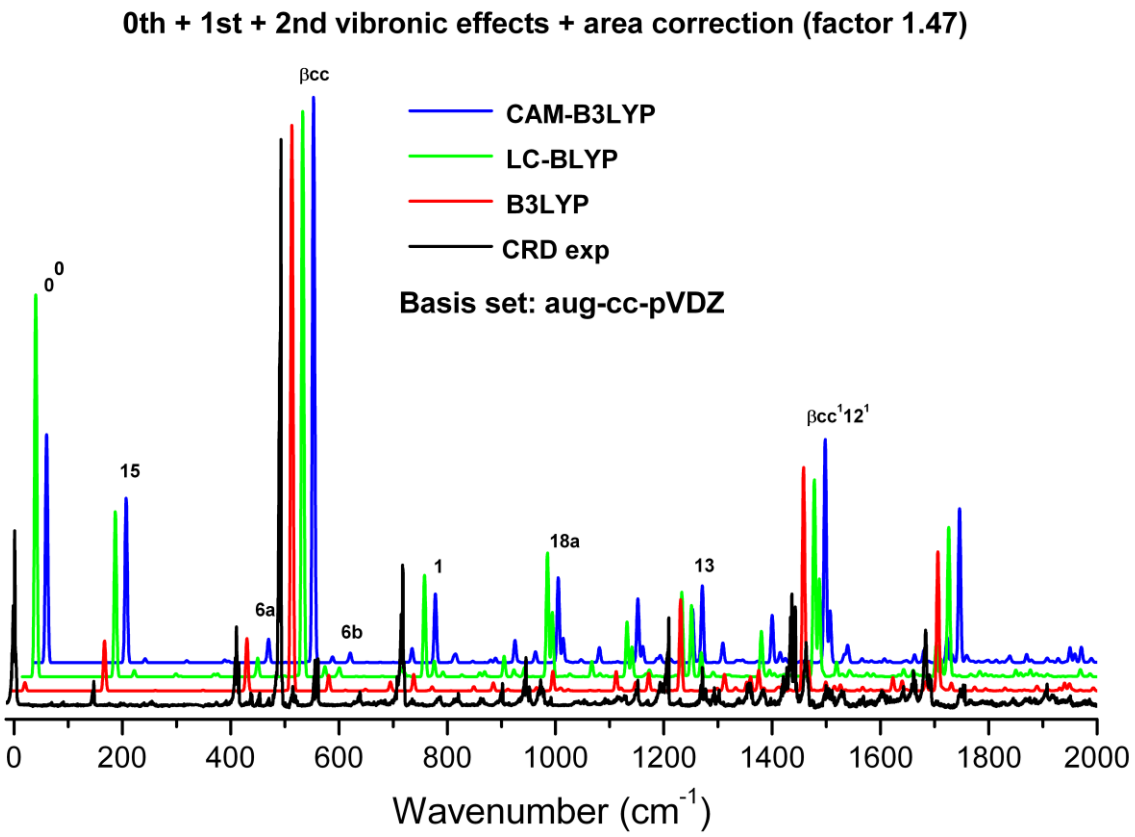

Figure 2.28: Simulation of the S_1 spectrum of PA up to the second order vibronic effects, including the area correction factor to the a_1 y-polarized modes. Spectra are scaled to make the βcc bands equal in height.

A more quantitative sense of the quality of the simulated spectra using various functionals and different effects (i.e. including first and second order vibronic effects and area correction) can be obtained by examining the differences between the calculated intensities of a selected set of the more intense vibrational peaks and their respective CRD intensities, but a direct comparison is not possible because of the lack of absolute CRD absorbances. Because of effects such as Fermi resonance and Coriolis coupling, one should not expect exact agreement between experimental and calculated vibronic intensities. These perturbations affect the lower intensity peaks more than the larger ones, so it is convenient to weight the percent errors of the bands by the fractional intensity of the transition with respect to the summed intensities of the set. To establish a value representing the quality of the calculations, we proceeded as follows:

1. The sums of the calculated line intensities (CI_i) and the CRD peak values (EX_i) are set equal:

$$\sum_i CI_i = \sum_i EX_i \quad \ldots(2.27)$$

2. The % errors are taken for each line:

$$Err_i = 100\left(\frac{|CI_i - EX_i|}{EX_i}\right) \quad \ldots(2.28)$$

3. The errors are weighted by the fractional line intensities:

$$W_i = \left(\frac{EX_i}{\sum_i EX_i}\right) \quad \ldots(2.29)$$

4. The weighted mean of the percent error set is:

$$\overline{Err_w} = \sum_i W_i Err_i \quad \ldots(2.30)$$

where summations are over the total number of vibronic bands reported in Tables 2.23-2.25. The weighted mean of the percent errors is a useful measure of the quality of the fit.

It is clear from Tables 2.23-2.25 that none of the simulations using the various functionals provide a high quality match throughout. The major reasons for the discrepancies vary between the functional used, however. From the weighted mean of the percent error analysis of the calculations done up to the first order effects (Table 2.23), it is clear that LRC functionals provided a more accurate over-all prediction of the spectrum than B3LYP. Including second order vibronic effects (Table 2.24) improved the calculation with B3LYP, but the calculations with CAM-B3LYP remained the same. Calculations done up to the second order vibronic effects where the y-polarized intensities (a_1 modes) were scaled up by the area correction factor (1.47, obtained above) significantly improved when using LRC functionals where CAM-B3LYP appears to give a more accurate simulation (Table 2.25). For B3LYP calculations, the primary fault lies in the value of equilibrium geometry transition moment (0.014 ea_0), with the low value producing a lack of intensity in the a_1 modes, as seen previously [27].

Table 2.23: Percent errors and weighted mean percent errors of the calculated intensities of a selected set of the stronger vibrational peaks with respect to the CRD intensities Calculated intensities were obtained including the calculations done up to first order vibronic effects.

Vibronic band	Symm	Freq	Wi[a]	% errors[a] (0^{th} + 1^{st} Order)		
				B3LYP	LC-BLYP	CAM-B3LYP
0-0	a_1	0	0.099	92	55	4
15^1	b_2	146	0.013	171	651	708
$6a^1$	a_1	409	0.044	29	86	76
βCC^1	b_2	493	0.318	56	10	17
βCH^1	b_2	561	0.026	99	84	90
1^1	a_1	719	0.079	85	94	92
$6a^2$	a_1	821	0.007	99	489	367
$\beta CC^1 6a^1$	b_2	902	0.012	100	88	90
12^1	a_1	945	0.027	90	83	73
$18a^1$	a_1	954	0.010	93	375	267
βCC^2	a_1	971	0.014	100	89	22
$9a^1$	a_1	1152	0.014	96	92	90
13^1	a_1	1191	0.012	94	68	59
$\beta CC^1 1^1$	b_2	1208	0.049	62	31	51
$6b^1 1^1$	b_2	1271	0.021	90	69	139
$\beta CC^1 12^1$	b_2	1436	0.063	207	81	80
1^2	a_1	1442	0.055	96	98	97
$\beta CC^1 18b^1$	a_1	1463	0.035	100	181	316
$18a^1 6b^1$	b_2	1529	0.007	91	556	371
$\beta CC^1 9a^1$	b_2	1641	0.010	49	93	11
$1^1 12^1$	a_1	1660	0.018	77	90	85
$\beta CC^1 13^1$	b_2	1682	0.042	188	98	98
$13^1 6b^1$	b_2	1754	0.011	70	7	1
$18a^2$	a_1	1908	0.012	100	517	76
Weighted mean % error[a]				88	82	75

a.See text for details.

Table 2.24: Percent errors and weighted mean percent errors of the calculated intensities of a selected set of the stronger vibrational peaks with respect to the CRD intensities Calculated intensities were obtained including the calculations done up to second order vibronic effects.

Vibronic band	Symm	Freq	Wi[a]	% errors[a] (0^{th} + 1^{st} +2^{nd} Order)		
				B3LYP	LC-BLYP	CAM-B3LYP
0-0	a_1	0	0.099	95	41	4
15^1	b_2	146	0.013	197	557	708
$6a^1$	a_1	409	0.044	35	84	76
βCC^1	b_2	493	0.318	42	5	17
βCH^1	b_2	561	0.026	52	86	90
1^1	a_1	719	0.079	98	94	92
$6a^2$	a_1	821	0.007	37	460	367
$\beta CC^1 6a^1$	b_2	902	0.012	72	88	90
12^1	a_1	945	0.027	96	82	73
$18a^1$	a_1	954	0.010	80	334	267
βCC^2	a_1	971	0.014	11	67	22
$9a^1$	a_1	1152	0.014	1	92	90
13^1	a_1	1191	0.012	98	69	59
$\beta CC^1 1^1$	b_2	1208	0.049	49	37	51
$6b^1 1^1$	b_2	1271	0.021	90	80	139
$\beta CC^1 12^1$	b_2	1436	0.063	185	79	80
1^2	a_1	1442	0.055	57	98	97
$\beta CC^1 18b^1$	a_1	1463	0.035	80	197	316
$18a^1 6b^1$	b_2	1529	0.007	32	623	371
$\beta CC^1 9a^1$	b_2	1641	0.010	90	94	11
$1^1 12^1$	a_1	1660	0.018	65	89	85
$\beta CC^1 13^1$	b_2	1682	0.042	164	98	98
$13^1 6b^1$	b_2	1754	0.011	72	2	1
$18a^2$	a_1	1908	0.012	86	568	76
Weighted mean % error[a]				75	78	75

a.See text for details.

Table 2.25: Percent errors of the calculated intensities for a selected set of the stronger vibrational peaks, with respect to the CRD intensities, for the different DFT functionals. Also given are fractional line intensities, weighted mean of the absolute percent errors, and equilibrium transition moments.

Vibronic band	Symm.	Freq.	Wi[a]	% errors[a]			
				B3LYP	B3LYP*	LC-BLYP	CAM-B3LYP
0-0	a_1	0	0.099	93	39	98	39
15^1	b_2	146	0.013	188	127	525	636
$6a^1$	a_1	409	0.044	8	28	78	68
βCC^1	b_2	493	0.318	38	9	9	7
βCH^1	b_2	561	0.026	53	63	82	78
1^1	a_1	719	0.079	98	39	34	47
$6a^2$	a_1	821	0.007	95	92	68	76
$\beta CC^1 6a^1$	b_2	902	0.012	73	100	61	46
12^1	a_1	945	0.027	95	89	135	90
$18a^1$	a_1	954	0.010	74	25	216	42
βCC^2	a_1	971	0.014	8	90	89	87
$9a^1$	a_1	1152	0.014	2	81	75	68
13^1	a_1	1191	0.012	41	132	267	174
$\beta CC^1 1^1$	b_2	1208	0.049	44	13	26	6
$6b^1 1^1$	b_2	1271	0.021	90	93	95	93
$\beta CC^1 12^1$	b_2	1436	0.063	177	115	60	114
1^2	a_1	1442	0.055	58	89	8	43
$\beta CC^1 18b^1$	a_1	1463	0.035	80	100	98	70
$18a^1 6b^1$	b_2	1529	0.007	34	94	74	68
$\beta CC^1 9a^1$	b_2	1641	0.010	88	65	93	91
$1^1 12^1$	a_1	1660	0.018	59	2	9	14
$\beta CC^1 13^1$	b_2	1682	0.042	156	101	97	94
$13^1 6b^1$	b_2	1754	0.011	73	79	86	86
$18a^2$	a_1	1908	0.012	81	100	69	78
Equil. Trans. Mom.				0.0140	0.0669	0.0907	0.0669
Weighted mean % error[a]				71	49	59	53

a.See text for details.

Examination of the calculated vibrational intensities compared to the experiment can indicate potential problem areas in the molecular potential energy surface. For the CAM-B3LYP and LC-BLYP results, the most obvious source of error is the low energy mode 15. This is the in-plane trans-bending motion of the acetylene group where the terminal carbon has the greatest excursion and the ring undergoes a rotation. The intensity of this mode appears about six times as large as it should in the LRC simulations, while it is only twice as big in the B3LYP simulations. This happens because the 1st order derivatives for mode 15 (Table 2.20) have increased in the LRC calculations (while the βCC moment derivatives and the vibrational vectors are about the same). In the perturbation theory picture of vibronic coupling, this b_2 vibration is mixing in a nearby A_1 electronic state, and is apparently over estimated with the LRC functionals. If mode 15 is removed from the analysis, all the functionals have approximately the same average error, with CAM-B3LYP being lowest by a small amount. At higher energy, mode 13 in the LRC calculations and the combination band $\beta CC^1 12^1$ in all the methods are also anomalously strong.

From the above considerations, it appears that B3LYP generates a poor equilibrium moment but better moment derivatives, while the LRC functionals are just the opposite. Since the equilibrium transition moment enters the vibronic calculations in a simple enough way, it is possible to use the equilibrium moment from one calculation along with the moment derivatives from another to produce a hybrid spectrum. Table 2.25 therefore contains a column that contains the results of a calculation using the moment derivatives from B3LYP and the equilibrium moment from CAM-B3LYP (referred to as B3LYP* in Table 2.25 and Fig. 2.29). This results in a considerably improved mean percent error. The B3LYP* vibronic simulation is compared to the CRD and CAM-B3LYP spectra in Fig. 2.29.

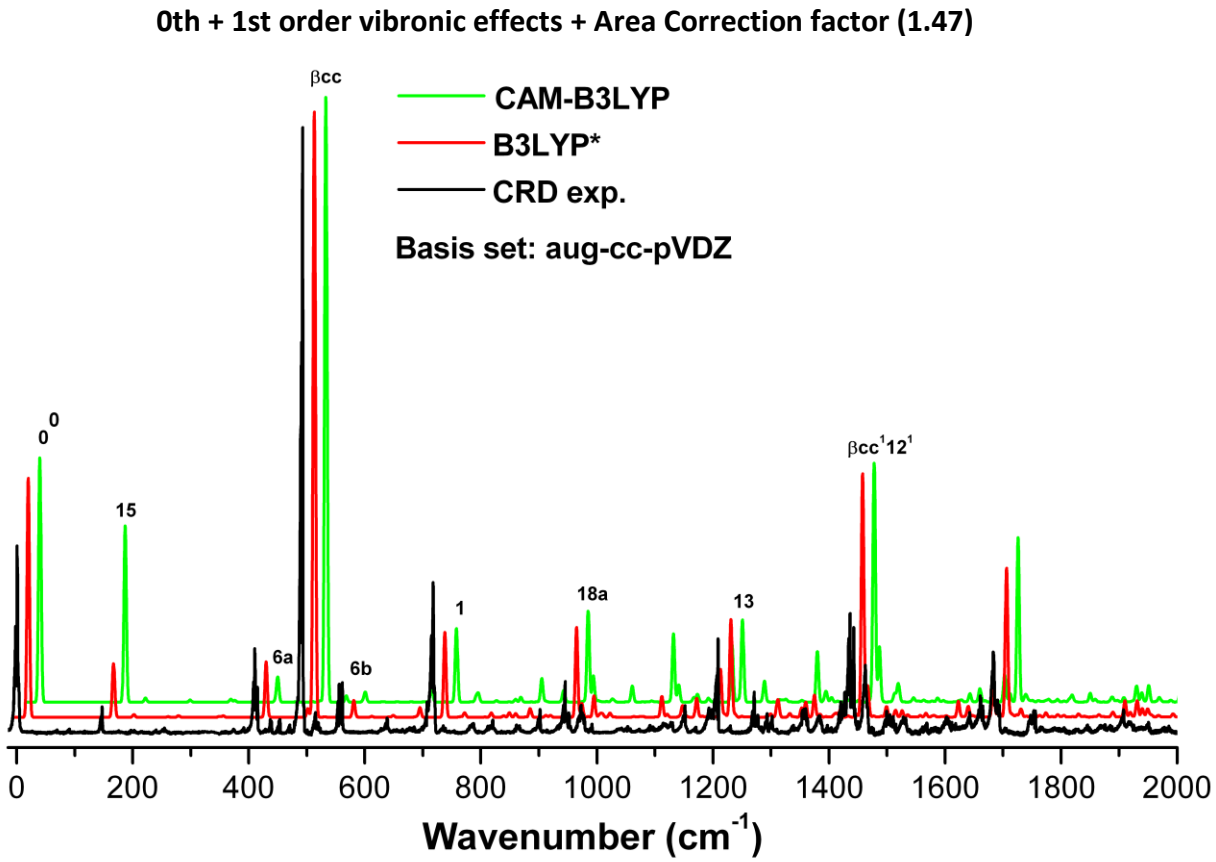

Figure 2.29: Comparison between the CRD spectrum and the simulated $S_1 \leftarrow S_0$ absorption spectra of PA with CAM-B3LYP and B3LYP* (where the intensities were calculated using B3LYP transition moment derivatives and the CAM-B3LYP equilibrium transition moment).

V. Conclusions

Using any of the functionals, the vibrational structure in the electronic spectra could be fairly accurately simulated for PA, a low symmetry and medium-sized molecule. The long-range corrected functional CAM-B3LYP provides a 5 times bigger equilibrium transition moment than B3LYP, while the equilibrium transition moment calculated with LC-BLYP higher yet by 36%, increasing the intensities of the a_1 modes in both cases. The increased a_1 intensities are a distinct improvement over our previous calculation [27] using B3LYP moments and MCSCF vibrations, but the relative intensities of certain b_2 vibrations using LRC functionals are less favorable. This may indicate that the LRC functionals do not get the state coupling quite right, or that the vibrational vectors are less than optimal. None of the functionals were without faults. For vibronic calculations on transitions completely forbidden by symmetry, and where the equilibrium moment is not an issue, it would appear that B3LYP would be the best choice. For weak allowed transitions, either B3LYP with an optimized equilibrium moment or CAM-B3LYP could be used.

The temperature in the argon slit-jet was found to be in the range of 30 ± 5K and the appearance of multiple hot-bands to the red of the band origin showed that the vibrational cooling is much less than the rotational cooling. Many of the hot bands observed near the band origin of this transition were assigned.

VI. References

1. King G. W., So S. P., *"Ethynylbenzene Analysis of 2790 a Absorption System"*. Journal of Molecular Spectroscopy **37**, 543 (1971).

2. Serrano-Andres L., Merchan M., Jablonski M., *"The electronic spectra of aryl olefins: A theoretical study of phenylacetylene"*. J Chem Phys **119**, 4294 (2003).

3. King G. W., So S. P., *"Ethynylbenzene Calculations of Energies of Electronic States"*. Journal of Molecular Spectroscopy **37**, 535 (1971).

4. Leopold D. G., Hemley R. J., Vaida V., Roebber J. L., *"Direct Absorption-Spectra of Higher Excited-States of Jet-Cooled Monosubstituted Benzenes - Phenylacetylene, Styrene, Benzaldehyde, and Acetophenone"*. J Chem Phys **75**, 4758 (1981).

5. Chia L., Goodman L., *"2-Photon Spectrum of Phenylacetylene"*. J Chem Phys **76**, 4745 (1982).

6. Platt J. R., *"Classification of Spectra of Cata-Condensed Hydrocarbons"*. J Chem Phys **17**, 484 (1949).

7. Philis J. G., Drougas E., Kosmas A. M., *"The (L-b)S-1 <- S-0 transition of phenylpropyne and phenylacetylene: an experimental and ab initio study"*. Chemical Physics **306**, 253 (2004).

8. Narayanan K., Chang G. C., Shieh K. C., Tung C. C., *"S-1<-S-0 transition of phenylacetylene: Ab initio and resonant two-photon ionization studies"*. Spectrochimica Acta Part a-Molecular and Biomolecular Spectroscopy **52**, 1703 (1996).

9. Amatatsu Y., Hasebe Y., *"Ab initio study on phenylacetylene in S-1 and S-2"*. Journal of Physical Chemistry A **107**, 11169 (2003).

10. Swiderek P., Gootz B., Winterling H., *"Electron-energy-loss spectroscopy of solid phenylacetylene"*. Chemical Physics Letters **285**, 246 (1998).

11. Swiderek P., Gootz B., *"The low-lying singlet-triplet transitions of phenylacetylene and styrene: Analysis of the vibronic structure"*. Berichte Der Bunsen-Gesellschaft-Physical Chemistry Chemical Physics **102**, 882 (1998).

12. Johnson P. M., Xu H. F., Sears T. J., *"The calculation of vibrational intensities in forbidden electronic transitions"*. J Chem Phys **125**, (2006).

13. Maiman T. H., *"Stimulated Optical Radiation in Ruby"*. Nature **187**, (1960).

14. Johnson P. M., *"Molecular Multi-Photon Ionization Spectroscopy"*. Accounts of Chemical Research **13**, 20 (1980).

15. Taylor D. P., "*REMPI-PES Studies of Some Rydberg States of CO_2*". Doctoral Thesis, State University of New York at Stony Brook (1993).

16. Dixit S. N., McKoy V., *"Theory of resonantly enhanced multiphoton processes in molecules"*. J. Chemical Physics **8**, (1985).

17. Verges J., Effantin C., D'Incan D., Cooper D. L., Barrow R. F., *"Double-minimun (2)1Σu+ state of sodium dimer"*. Physical Review Letters **53**, (1984).

18. Hurst G. S., *"Resonance Ionization Spectroscopy"*. Analytical Chemistry **53(13)**, (1981).

19. Hofstein J., Xu H. F., Sears T., Johnson P. M., *"Fate of excited states in jet-cooled aromatic molecules: Bifurcating pathways and very long lived species from the S-1 excitation of phenylacetylene and benzonitrile"*. Journal of Physical Chemistry A **112**, 1195 (2008).

20. Townsend D., Minitti M. P., Suits A. G., *"Direct current slice imaging"*. Review of Scientific Instruments **74**, (2003).

21. Garcia G. A., Nahon L., Powis I., *"Two-dimensional charged particle image inversion using a polar basis function expansion"*. Rev Sci Instrum **75**, (2004).

22. Dribinski V., Ossadtchi A., Mandelshtam V. A., Reisler H., *"Reconstruction of Abel-transdormable images: The Gaussian basis-set expansion Abel transform method"*. Review of Scientific Instruments **73**, (2002).

23. Zhou J., "*Slow Electron Velocity-map Imaging Spectroscopy of small radicals and infrared multiphoton dissociation study of solvated systems.*". University of California, Berkeley (2008).

24. Chestakov D. A., Wu S. M., Parker D. H., Eppink A., Kitsopoulos T. N., *"Slicing Using a Conventional Velocity Map Imaging Setup: O2, I2, and I2+ Photodissociation"*. J Phys Chem A **108**, (2004).

25. Sato Y., Matsumi Y., Kawasaki M., Tsukiyama K., Bersohn R., *"Ion Imaging of the Photodissociation of OCS near 217 and 230 nm"*. J Phys Chem-Us **99**, (1995).

26. Bordas C., Paulig F., Helm H., Huestis D. L., *"Photoelectron imaging spectroscopy: Principle and inversion method"*. Rev Sci Instrum **67**, (1996).

27. Chang C. H., Lopez G., Sears T. J., Johnson P. M., *"Vibronic Analysis of the S(1)-S(0) Transition of Phenylacetylene Using Photoelectron Imaging and Spectral Intensities Derived from Electronic Structure Calculations"*. Journal of Physical Chemistry A **114**, 8262 (2010).

28. King G. W., So S. P., *"Ethynylbenzene - Vibrational Spectra of Some Deuterated Isomers"*. Journal of Molecular Spectroscopy **36**, 468 (1970).

29. King G. W., So S. P., *"Allowed and Forbidden Components in 2790 a System of Ethynylbenzene"*. Journal of Molecular Spectroscopy **33**, 376 (1970).

30. Wilson E. B., *"The Normal Modes and Frequencies of Vibrations of the Regular Plane Hexagon Model of the Benzene Molecule"*. Physical Review **45**, (1934).

31. Schutte C. J. H., Bertie J. E., Bunker P. R., Hougen J. T., Mills I. M., Watson J. K. G., Winnerwisser B. P., *"Notations and Conventions in Molecular Spectroscopy: Part 2. Symmetry Notation"*. International Union of Pure and Applied Chemistry **69**, (1977).

32. Schutte C. J. H., Bertie J. E., Bunker P. R., Hougen J. T., Mills I. M., Watson J. K. G., Winnerwisser B. P., *"Notations and Convenctions in Molecular Spectroscopy: Part 2. Symmetry Notation"*. International Union of Pure and Applied Chemistry **69**, (1997).

33. Herzberg G., *Molecular Spectra and Molecular Structure: II. Infrared and Raman Spectra of Ployatomic Molecules*. (D. Van Nostrand Company, Inc., Princenton ed., 1945).

34. Herzberg G., *Molecular Spectra and Molecular Structure: III. Electronic Spectra and Electronic Structure of Polyatomic Molecules*. (D. Van Nostrand Company, Inc., Princeton ed., 1966).

35. Ribblett J. W., Borst D. R., Pratt D. W., *"Styrene and phenylacetylene: Electronic effects of conjugating substituents "off" and "on" the axis of a benzene ring"*. Journal of Chemical Physics **111**, 8454 (1999).

36. Powers D. E., Hopkins J. B., Smalley R. E., *"Vibrational-Relaxation in Jet-Cooled Phenylalkynes"*. J Chem Phys **74**, 5971 (1981).

37. Kim M. S., Kwon C. H., Kim H. L., *"Vibrational analysis of vacuum ultraviolet mass-analyzed threshold ionization spectra of phenylacetylene and benzonitrile"*. Journal of Physical Chemistry A **107**, 10969 (2003).

38. Lin J. L., Tzeng W. B., *"Identification of impurities in phenylacetylene by species-selected mass-analyzed threshold ionization spectroscopy"*. Applied Spectroscopy **57**, 1178 (2003).

39. Dyke J. M., Ozeki H., Takahashi M., Cockett M. C. R., Kimura K., *"A Study of Phenylacetylene and Styrene, and Their Argon Complexes Pa-Ar and St-Ar with Laser Threshold Photoelectron-Spectroscopy"*. J Chem Phys **97**, 8926 (1992).

40. Paldus B. A., Kachanov A. A., *"An historical overview of cavity-enhaced methods"*. Canadian Journal of Physics **83**, (2005).

41. O'Keefe A., Deacon D. A. G., *"Cavity ring-down optical spectrometer for absorption measurements using pulsed laser sources"*. Review of Scientific Instruments **59**, (1988).

42. Berden G., Peeters R., Meijer G., *"Cavity-ring-down spectroscopy: experimental schemes and applications"*. International Reviews in Physical Chemistry **19**, (2000).

43. Lehmann K., Berden G., Engeln R., in *Book "An introduction to Cavity Ring-Down Spectroscopy"*. (Blackwell Publishing, Ltd., 2009).

44. Markiewicz B., Milan M., Teslja A., Chang C. H., Hall G. (To Be Published).

45. Bacon A. R., Hollas J. M., Ridley T., *"Herzberg Teller Intensity Stealing in the 279-Nm System of Phenylacetylene - Evidence from Single Vibronic Level Fluorescence-Spectra"*. Can J Phys **62**, 1254 (1984).

46. Bacon A. R., Hollas J. M., Ridley T., *"Herzberg-Teller intensity stealing in the 279-nm system of phenylacetylene: Evidence from single vibronic level fluorescence spectra"*. Canadian Journal of Physics **62**, (1984).

47. Hohenberg P., Kohn W., *"Inhomogeneous Electron Gas"*. Physical Review **136**, B864 (1964).

48. Tawada Y., Tsuneda T., Yanagisawa S., Yanai T., Hirao K., *"A long-range-corrected time-dependent density functional theory"*. J Chem Phys **120**, 8425 (2004).

49. Chai J. D., Head-Gordon M., *"Long-range corrected hybrid density functionals with damped atom-atom dispersion corrections"*. Physical Chemistry Chemical Physics **10**, 6615 (2008).

50. Tozer D. J., Handy N. C., *"Improving virtual Kohn-Sham orbitals and eigenvalues: Application to excitation energies and static polarizabilities"*. J Chem Phys **109**, 10180 (1998).

51. Kamiya M., Tsuneda T., Hirao K., *"A density functional study of van der Waals interactions"*. J Chem Phys **117**, 6010 (2002).

52. Yanai T., Tew D. P., Handy N. C., *"A new hybrid exchange-correlation functional using the Coulomb-attenuating method (CAM-B3LYP)"*. Chemical Physics Letters **393**, 51 (2004).

53. Richard R. M., Herbert J. M., *"Time-Dependent Density-Functional Description of the (1)L(a) State in Polycyclic Aromatic Hydrocarbons: Charge-Transfer Character in Disguise?"*. Journal of Chemical Theory and Computation **7**, 1296 (2011).

54. Dunning T. H., *"Gaussian-Basis Sets for Use in Correlated Molecular Calculations .1. The Atoms Boron through Neon and Hydrogen"*. J Chem Phys **90**, 1007 (1989).

55. Tang B. Z., Law C. C. W., Lam J. W. Y., Qin A. J., Dong Y. Q., Kwok H. S., *"Synthesis, thermal stability, light emission, and fluorescent photopatterning of poly (diphenylacetylene)s carrying naphthalene pendant groups"*. Polymer **47**, 6642 (2006).

56. Duschinsky F., *"On the interpretation of electronic spectra of polyatomic molecules"*. Acta Physico-Chimica U.R.S.S. **7**, (1937).

57. *"Gamess Version 11 Aug. 2011 (R1) and Version 11 Apr. 2008 (R1)"*, Schmidt M. W., Baldridge K. K., Boatz J. A., Elbert S. T., Gordon M. S., Jensen J. H., Koseki S., Matsunaga N., Anguyen K. A., Su S. J., Windus T. L., Dupuis M., Montgomery J. A. (J. Comp. Chem. 14, 1347-1363(1993), 2010, 2011)

58. *"Gaussian 09, Revision B.01"*, Frisch M. J., Trucks G. W., Schlegel H. B., Scuseria G. E., Robb M. A., Cheeseman J. R., Scalmani G., Barone V., Mennucci B., Petersson G. A., Nakatsuji H., Caricato M., Li X., Hratchian H. P., Izmaylov A. F., Bloino J., Zheng G., Sonnenberg J. L., Hada M., Ehara M., Toyota K., Fukuda R., Hasegawa J., Ishida M., Nakajima T., Honda Y., Kitao O., Nakai H., Vreven T., Montgomery J., J. A., Peralta J. E., Ogliaro F., Bearpark M., Heyd J. J., Brothers E., Kudin K. N., Staroverov V. N., Kobayashi R., Normand J., Raghavachari K., Rendell A., Burant J. C., Iyengar S. S., Tomasi J., Cossi M., Rega N., Millam N. J., Klene M., Knox J. E., Cross J. B., Bakken V., Adamo C., Jaramillo J., Gomperts R., Stratmann R. E., Yazyev O., Austin A. J., Cammi R., Pomelli C., Ochterski J. W., Martin R. L., Morokuma K., Zakrzewski V. G., Voth G. A., Salvador P., Dannenberg J. J., Dapprich S., Daniels A. D., Farkas Ö., Foresman J. B., Ortiz J. V., Cioslowski J., Fox D. J. (Gaussian, Inc., Wallingford, CT., 2010)

59. Borrelli R., Peluso A., *"Dynamics of radiationless transitions in large molecular systems: A Franck-Condon-based method accounting for displacements and rotations of all the normal coordinates"*. J Chem Phys **119**, 8437 (2003).

60. Sears T. J., *"The calculation of the energy levels of an asymmetric top free radical in a magnetic field"*. Computer Physics Reports **2**, (1984).

61. Sears T. J., *"ASYTOP - A program for detailed analysis of gas phase magnetic resonance spectra of asymmetric top molecules"*. Computer Physics Communications **34**, (1984).

62. Csaszar A. G., Fogarasi G., Boggs J. E., *"Theoretical Prediction of the Vibrational-Spectrum, Geometry, and Scaled Quantum-Mechanical Force-Field for Phenylacetylene"*. Journal of Physical Chemistry **93**, 7644 (1989).

63. Mulliken R. S., *"Electronic Population Analysis on LCAO-MO Molecular Wave Functions. I "*. J Chem Phys **23**, (1955).

64. Cox A. P., Ewart I. C., Stigliani W. M., *"Microwave-Spectrum, Structure and Dipole-Moment of Phenylacetylene"*. Journal of the Chemical Society-Faraday Transactions Ii **71**, 504 (1975).

CHAPTER 3

STUDY OF THE LONG-LIVED SPECIES FROM THE S_1 EXCITATION OF PHENYLACETYLENE

I. Introduction

When aromatic molecules are excited to their lowest singlet state (S_1), the excited state can decay by fluorescence or non-fluorescent pathways to excited vibrational levels of S_0 or an excited triplet state, normally T_1, in some excited vibrational level. The distribution among these derives from the kinetic competition of the pathways created by the non-stationary state that contains the oscillator strength of the transition. This behavior can be observed in most benzene-based aromatic molecule; however, not all of them follow the same pattern, as has been reported by Hofstein et al. (from now on refer as HXSJ) [1], for example.

The fact that the fluorescence quantum yield after the absorption of light is less than unity in this kind of molecule demonstrates that radiationless transitions play an important role in the decay of their excited states. Radiationless transitions are defined as the change in the electronic state of the molecule that occurs when no radiation is absorbed or emitted. Usually, these transitions are divided into two types: internal conversion (IC) and intersystem crossing (ISC) processes. IC is related to a transition between states of the same multiplicity while ISC is a transition between states of different multiplicity [2].

Intersystem crossing forms species with short lifetimes and occurs between the first singlet excited state (S_1) and the lowest triplet state (T_1). The energy gap between S_1 and T_1 for substituted benzenes is around 6000-8000 cm^{-1} which means that the triplet state produced in collision-less environment experiments contains a large amount of vibrational energy because of the energy gap. The large amount of vibrational energy accelerates the radiationless process of

returning hot triplet molecules to their ground state and explains the fact that the lifetime of hot triplet molecules is shorter than the lifetime of cold triplet molecules in a collision-free environment [3-7].

In recent experiments on phenylacetylene and benzonitrile, HXSJ [1] reported that some of the initially excited S_1 state of these molecules evolve into a very long-lived species with a lifetime of longer than 100 microseconds. However, the identity of this long-lived species was not determined but the possibility of an isomer with low ionization potential or cold triplet states relaxing from a hot triplet state was suggested.

The mechanism that can produce such a stable excited state in a collisionless environment is not immediately obvious, and various possibilities have been previously explored [1]. The possible mechanisms include:

1. Intersystem crossing into an isoenergetic set of states in the triplet manifold.

   From previous molecular studies [1, 8] by pump-probe ionization, the signal remaining after the singlet decay has always been ascribed to the ionization of hot triplet levels isoenergetic to the initial S_1 level with vibrational energy equal to S_1-T_1. PES [8] and MATI [9, 10] experiments on pyrazine have confirmed the previous observations. This could also be the case for PA, but it is difficult to imagine why a triplet state with almost 11 000cm^{-1} of vibrational energy would have such a long lifetime. The previous record is held by aniline at 5.6μs [11] (S_1-T_1 gap, at 7200cm^{-1}).PES experiments by Hofstein et al. [1] reported that the peak representing the long-lived species does not change with the laser delay while the singlet is decaying. This means that the entity produced does not depend on the singlet state during the laser pulse and is not a product of this state.

2. Internal conversion into highly excited vibrational levels of the molecular ground state.

   Internal conversion of S_1 to high vibrational levels of S_0 would create a state that has an indefinitely long lifetime. However, the ionization of a state with 38000cm^{-1} of vibrational energy would be insignificantly small because Franck-Condon factors for excitation to energetically accessible ion states are very small. There is no evidence from the study on other molecules of any ionization signal from the hot ground state [4, 6, 11].

   The 193nm photon from the probe laser could also cause a transition to a hot neutral excited state that then autoionize [12], a process that usually takes a long time. Using a high voltage to field ionize then accelerate the electrons to the detector after the primary pulse; HXSJ [1] observed that the signal from the delayed electrons represented less than 1% of the total signal. Hence, the evidence so far suggests that highly vibrational excited S_0 state molecules are out of the source of the long-lived species.

3. Intersystem crossing followed by near-IR emission to low vibrational levels of the lowest triplet state that is known to be long-lived in related species.

   Another possible way to quench PA monomers from S_1 to a low vibrational level of the triplet state (T_1) in a collisionless environment in a supersonic molecular beam is by radiative emission. HXSJ [1] did an exhaustive search for IR emission but did not observed any. Moreover, while measurements show both the S1 state with its 75 ns lifetime and the long-lived species are formed simultaneously on the time scale of the

10 ns laser pulses used in the experiments, one would expect the production of long-lived species as the singlet state decays, similar to the PES observations by HXSJ [1].

4. Isomerization.

   There are many ways in which PA can form isomers. Schroeter et al.[13] proposed some possible isomers while HXSJ [1] suggested that the isomer should have a low ionization potential (IP). However, a definite structure for any possible isomer has not been reported.

Several experiments were conducted with the aim of identifying the mechanism of formation of the long-lived species. The decay curve for the strongest bands in the $S_1 \leftarrow S_0$ transition of the molecule were measured in order to shed light on whether particular normal modes promote or inhibit that the formation of the long lived species. Another approach involves theoretical calculations of the absolute energies and ionization potentials (IP) of various structural isomers. Details of investigations along these lines are described below.

II. Experiments

A. Pump-Probe Photoionization

1. Background

The interaction between the excited electronic states of aromatic molecules and particularly the time evolution of a non-stationary state created in a pulsed laser excitation can be studied by pump-probe ionization spectroscopy. [1, 6, 8].

A variant of this technique, the two-color pump-probe photoionization, uses one laser to resonantly excite the molecules to the singlet (S_1) vibronic level which may in time cross over to an isoenergetic point in the triplet manifold and a second laser that has short enough wavelength and sufficient intensity to overcome the Franck-Condon factor differences and ionize both singlet and triplet manifolds with almost the same efficiency. Molecules going on the ground state surface are very difficult to ionize since the Franck-Condon region for that ionization is above the laser photon energy. The evolution of the excited states can be followed by delaying the time between the ionization laser (probe) and the excitation laser (pump) and since photoionization is not limited by the spin selection rules (the ionic state is a doublet), the evolution in time of both excited singlet and triplet states can be studied by detecting the species present at varying times following S_1 excitation.

2. Experimental Setup

The experimental setup used in this work resulted from a combination of the setups previously described by HXSJ [1] and CLSJ [14]. Fig. 3.1 shows a schematic. Phenylacetylene (PA, 98%) was purchased from Aldrich and used without further purification.

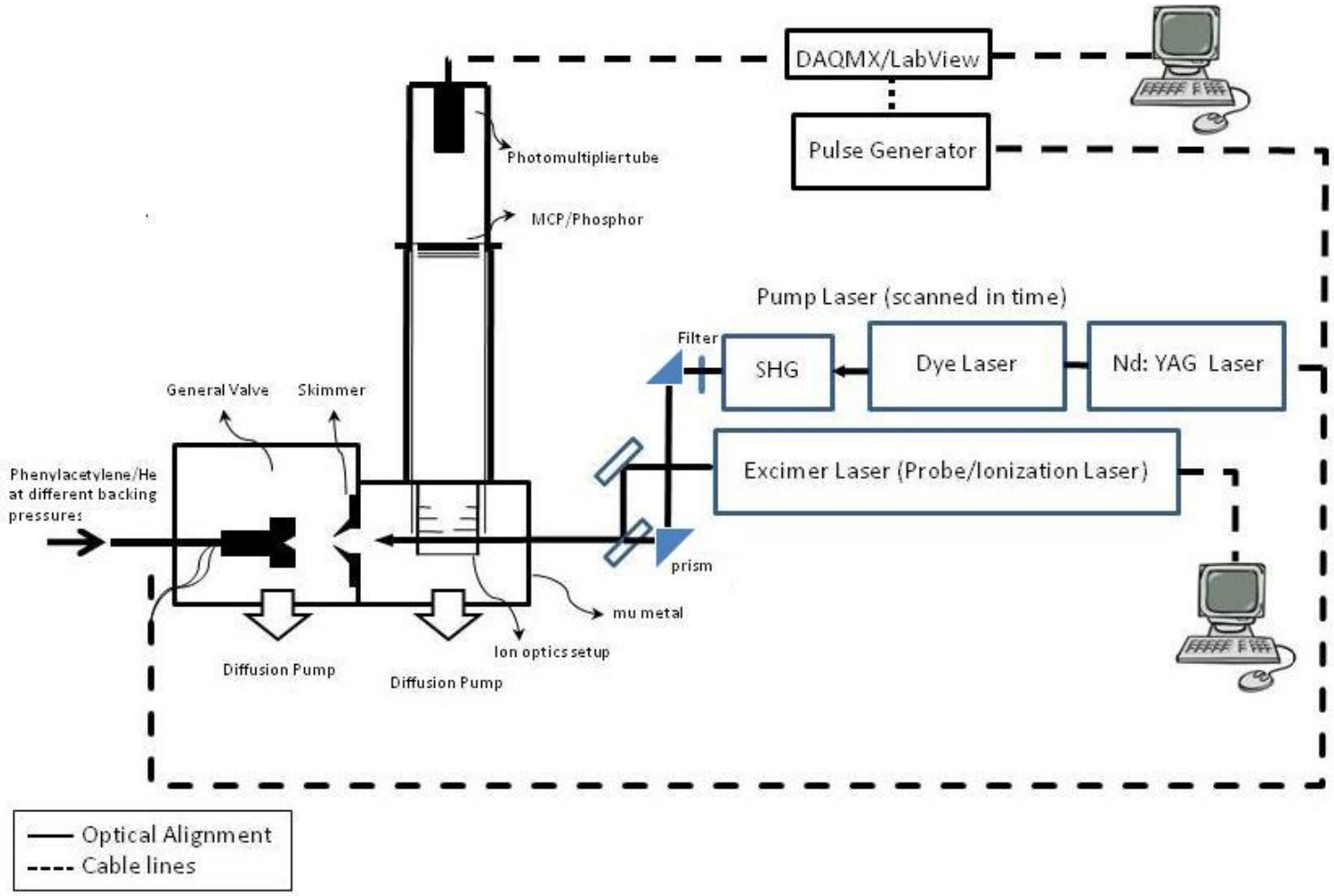

Figure 3.1: Experimental setup for 1+1 REMPI spectroscopy. SHG: Second harmonic generator, DAQMX: data acquisition board.

Briefly, helium was used as a carrier gas in a supersonic expansion of the sample through a pulsed valve running at 10 Hz and with orifice diameter of 300 μm. Three different backing pressures were used (200, 400 and 2560 torr) to see the effect of rotational cooling in the formation of the long-lived species; 200 torr was chosen since CLSJ [14] reported good quality photo-electron spectroscopy images and an absence of dimers in the TOF mass spectrum at this pressure. The molecular beam was collimated by a 3 mm diameter skimmer. The ion optics and the time-of-flight (TOF) region were shielded with mu-metal to provide magnetic isolation. The detection system consisted of a micro-channel plate detector (75 mm chevron-type MCP, Photonis) with a phospor and a photomultiplier tube (PMT). A pulsed Nd:YAG laser (Quantel,YG580,) was used to pump the dye laser and the output of the dye laser was doubled by a BBO crystal located in an autotracker (Inrad, ATIII), and directed into the chamber in the opposite direction to the molecular beam. An ArF excimer laser (GAM Laser, EX5) was used as a probe laser to ionize the excited molecules since the 193nm radiation from this laser is enough to ionize the S_1 states and any possible triplet state produced by the intersystem crossing from the singlet. The probe laser was introduced into the chamber coaxially to both the molecular and pump laser beams in the same direction as the pump beam and in the opposite direction to the molecular beam. The resulting ions were detected by time-of-flight mass spectroscopy using a micro-channel plate (MCP) coupled to a phosphor plate. The fluorescence from the phosphor was captured by a photomultiplier tube, and finally transferred to a computer for storage and further analysis. The scans were acquired by moving the time delay of the pump laser pulse while the time delay of the probe laser pulse was fixed. Measurement of the pump laser wavelength was done with a wavemeter (Coherent, WaveMaster). The timings of the pulsed

valve and laser systems were controlled by pulse generators (Stanford Research System, DG535) and computer controlled NI-DAQ cards.

The data collection and analysis were done using LabVIEW software. The previously analyzed CRD and 1+1 REMPI spectra (Chapter 2) were used to select specific assigned bands in the $S_1 \leftarrow S_0$ transition of PA, i.e. ν_0, ν_{15}, ν_{6a}, $\nu_{\beta CC}$ and ν_1. The experimental time-decay results were fitted with two exponential functions that simulated the formation (exponential growth) and decay (exponential decay) of the excited state.

3. Results and Discussions

The pump-probe delay photoionization decay curves for the band origin and four other assigned strong bands in the $S_1 \leftarrow S_0$ transition of PA confirm that after the $S_1 \leftarrow S_0$ excitation the decay consists of a prompt short-lived component matching the measured singlet fluorescence lifetime (~75 ns as reported before [15]) and a second component with very long lifetime as shown for example in Fig. 3.2.

A possible explanation for this long lifetime species could be the production of the lower vibrational levels of the triplet manifold following the dissociation of clusters. However, by looking at the rotationally resolved structure of the origin band of the PA $S_1 \leftarrow S_0$ transition at different pump-probe delay times, Xu et al. [16] demonstrated that the production of the long-lived species followed the rotationally resolved spectrum of the isolated monomer and was therefore not the result of excitation of clusters. Moreover, photo-electron spectroscopic (PES) experiments previously done by HXSJ [1] have shown that this component is produced independently of the singlet manifold. Plausible explanations for the experimental measurements are the possibility of formation of a stable geometrical isomer of PA following excitation to the S_1 state, or some as yet unexplained way of reaching low-lying triplet state vibrational level.

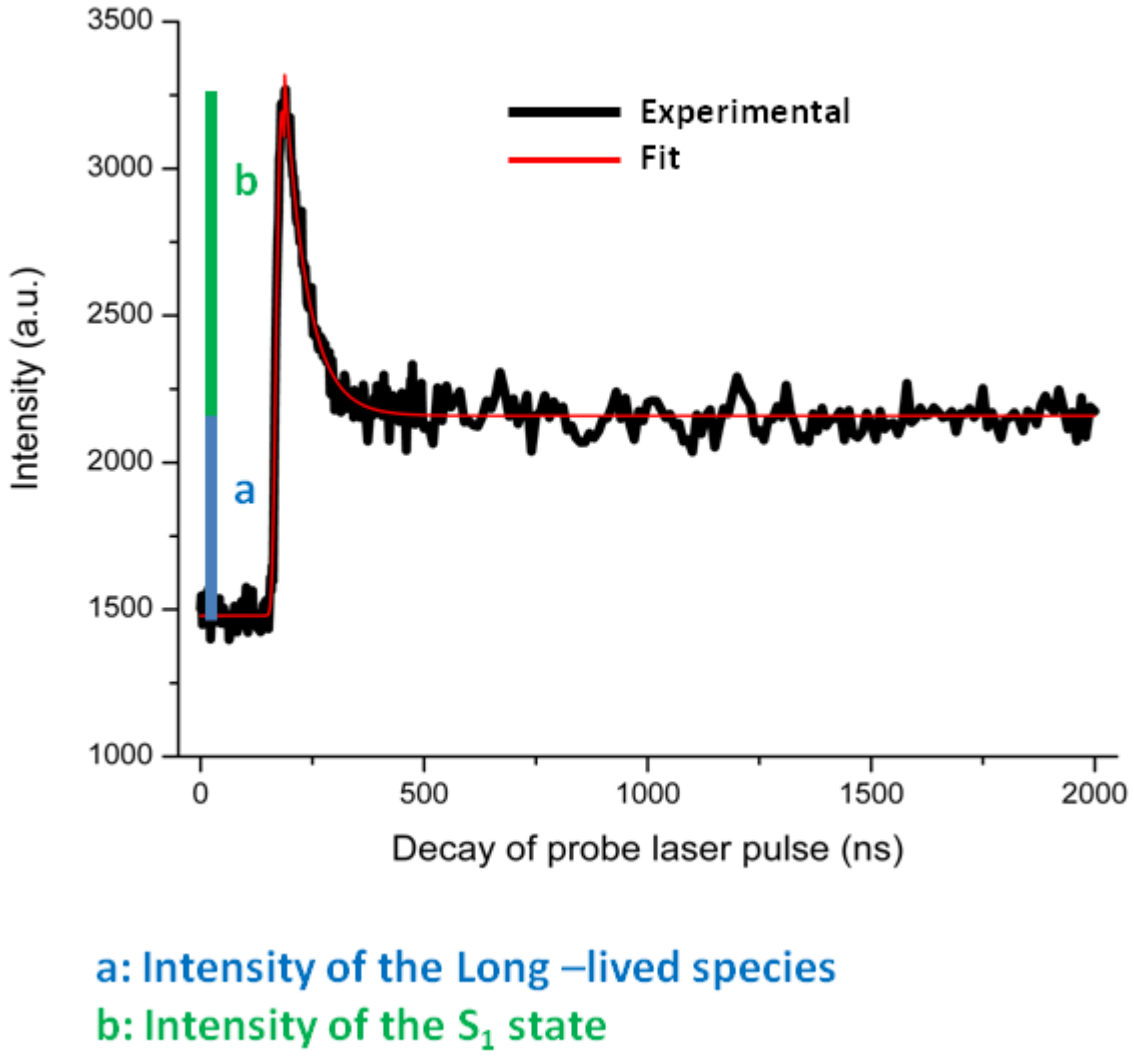

Figure 3.2: Pump-probe delay photoionization decay curve of PA. The wavelength of the pump laser corresponds to the origin of $S_1 \leftarrow S_0$ transition, while an excimer laser was used to ionize the molecules. A fast initial decay due to the decay of S_1 and a long-lived component are shown.

In order to further investigate these results, a study of its formation as a function of the initially excited vibrational levels of PA $S_1 \leftarrow S_0$ transition was made by looking at the ratio between the singlet population (as determine by its ionization signal) and that of the long-lived species, see Fig. 3.2.

The left hand side of the peak is the baseline related to the excitation caused by the excimer laser , the peak is where both lasers (pump and probe lasers) overlap and the right hand side is the intensity of the long-lived species. We know that the lifetime of the S_1 state is ~75ns so to be in a "safe" region, the baseline was considered to be up to 50ns while the intensity of the long-lived species was taken after 5 times the lifetime of the S_1 state (375ns). An average value for the baseline and the long-lived species intensity were obtained while the maximum experimental peak was used as the intensity for the S_1 state. The S_1 state intensity to the Long-lived species ratio (b/a in Fig 3.2) was obtained as follows:

$$\frac{a+b}{a} = \frac{(Peak - \overline{baseline})}{(\overline{long-lived\ species} - \overline{baseline})} \quad \ldots(3.1)$$

$$1+\frac{b}{a} = \frac{(Peak - \overline{baseline})}{(\overline{long-lived\ species} - \overline{baseline})} \quad \ldots(3.2)$$

$$\frac{b}{a} = \left[\frac{(Peak - \overline{baseline})}{(\overline{long-lived\ species} - \overline{baseline})}\right] - 1 \quad \ldots(3.3)$$

It was observed that this ratio was not the same for the different bands studied in this work. Table 3.1 shows the ratios at different sample pressures for the origin and the vibrational modes ν_{15}, ν_{6a}, $\nu_{\beta cc}$, and ν_1, respectively [17, 18]. The results imply that some vibrational modes better promote the formation of the long-lived species than others. In fact, at 2560 and 400 torr,

two of the strong bands in PA (6a and 15) have very low ratios that indicate that the normal coordinates of these modes could lie near the reaction path for the formation of the long-lived species. However, at 200 torr the ratio of the βCC band is the lowest, compared to the other 4 bands.

Numbering the acetylene carbons in PA as 7 and 8 where C7 is attached to the ring at C1, Serrano-Andres et al. [19] described the 6a mode as the C7C8H8-ring breathing, the 15 mode as the CCH – C7C8H8 bend, the mode βCC as the C1C7C8 bend and the mode 1 as the ring breathing. Our results agree with this analysis. Figs. 3.3 and 3.4 describe the motion of the molecule at the different strong bands analyzed in this study.

The results in Table 3.1show that excitation in the ν_{15} or $\nu_{\beta CC}$ modes encourages formation of the long-lived species. Possible geometrical isomers of PA such as phenyl-vinylidene (PV), benzocyclobutadiene (BCBD), cycloocta-1,3,5-trien-7yne (COTY), pentalene and some others have been previously suggested [13]. PV, BCBD and COTY are shown in Fig. 3.5. It is difficult to explain how ν_{6a} will promote formation of any unsymmetrical isomer.

Table 3.1: Ratios between the singlet channel signal to the one of the long-lived species at different sample pressures for the origin, 15, 6a, βcc, and 1bands, respectively.

		2560 Torr		**400 Torr**		**200 Torr**	
Band	**Symmetry**	**S_1/LLS**	**SD**	**S_1/LLS**	**SD**	**S_1/LLS**	**SD**
Origin	a_1	3.03	0.38	2.76	0.12	2.59	0.14
15	b_2	1.48	0.33	1.84	0.15	1.86	0.13
6a	a_1	1.75	0.19	2.08	0.14	1.87	0.12
βCC	b_2	3.11	0.36	2.26	0.24	1.48	0.09
1	a_1	2.77	0.35	2.24	0.19	2.52	0.18

S_1: Singlet manifold
LLS: Long-Lived Species
SD: Standard Deviation

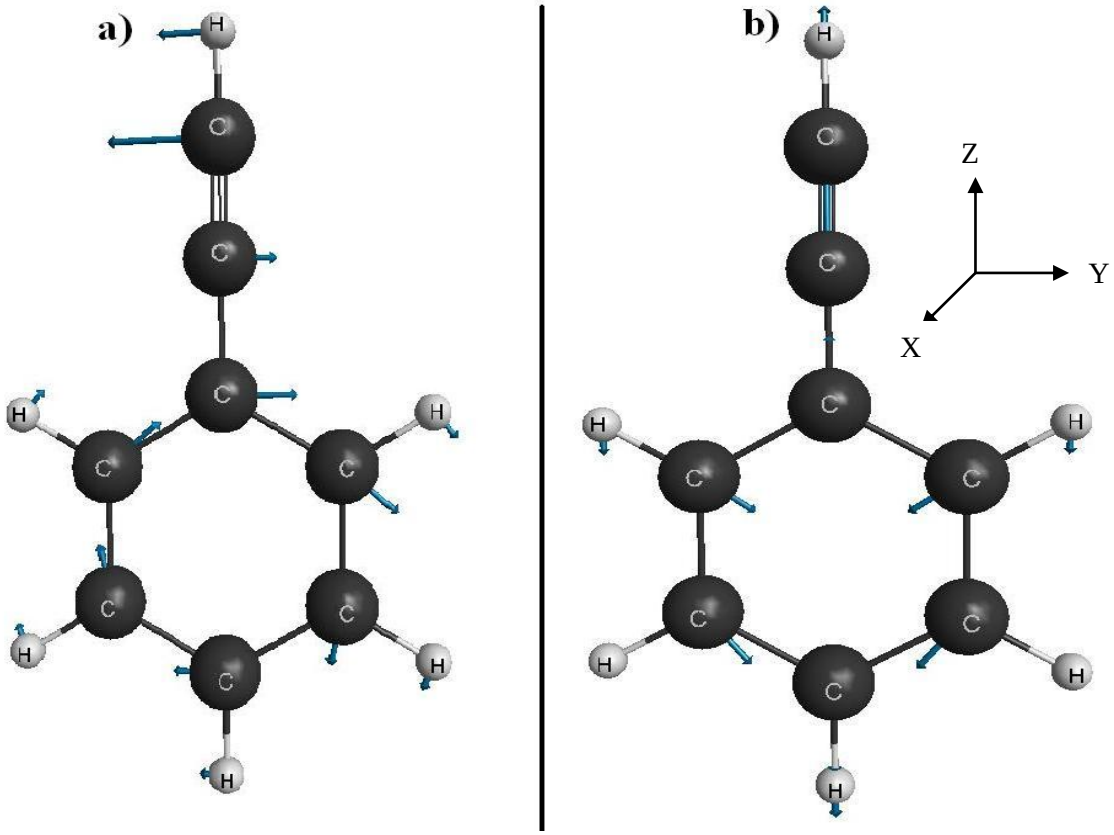

Figure 3.3: Mode description for the ν_{15} and ν_{6a} strong bands for the $S_1 \leftarrow S_0$ transition of PA. a) ν_{15}. b) ν_{6a}. Blue arrows represent the vectors that describe the motion of the atoms.

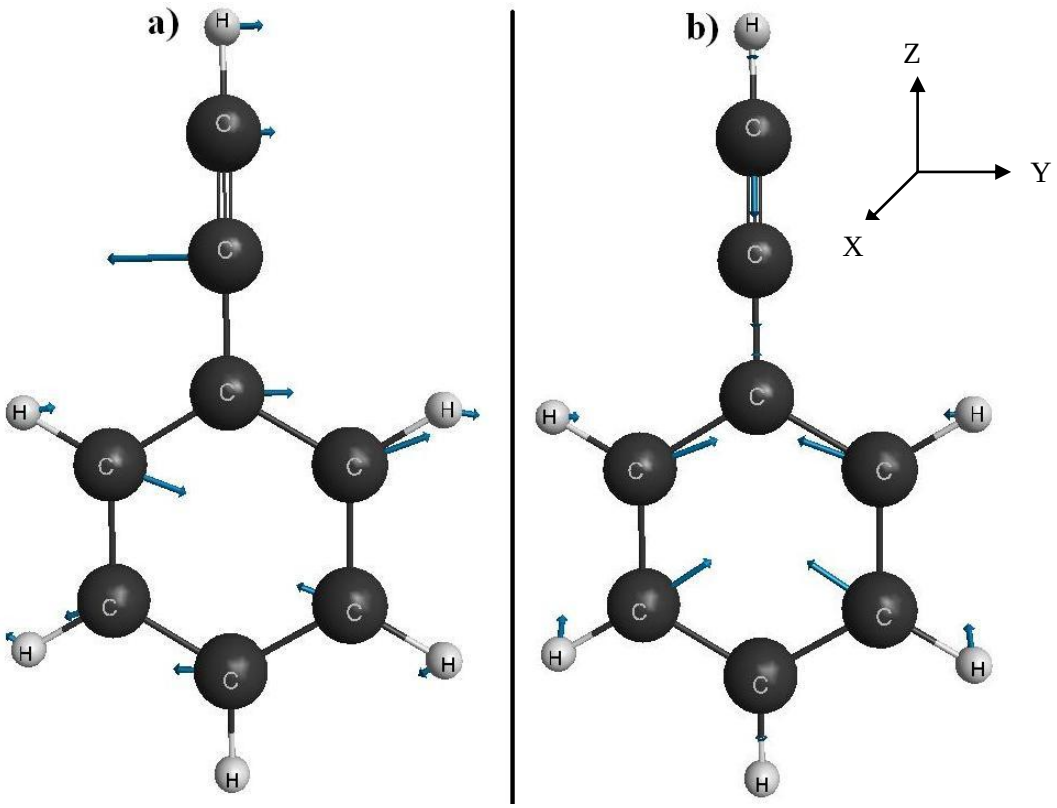

Figure 3.4: Mode description for the $\nu_{\beta cc}$ and ν_1 strong bands for the $S_1 \leftarrow S_0$ transition of PA. a) $\nu_{\beta cc}$. b) ν_1. Blue arrows represent the vectors that describe the motion of the atoms.

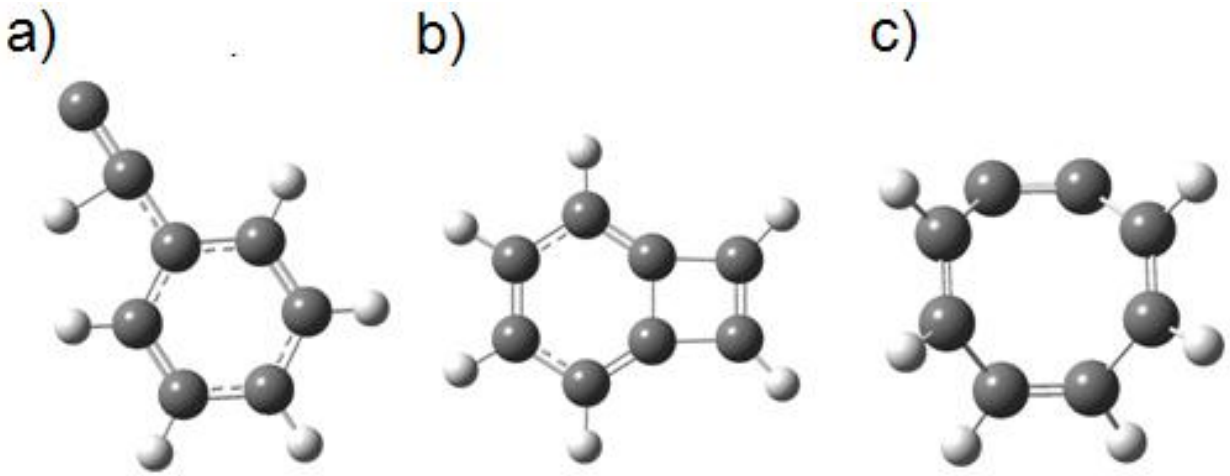

Figure 3.5: Possible PA Isomers considering ν_{15} and $\nu_{\beta cc}$ for the $S_1 \leftarrow S_0$ transition of PA. a) Phenyl-vinylidene (PV). b) Benzocyclobutadiene (BCBD). c) Cycloocta-1,3,5-trien-7-yne (COTY).

Considering that previous experiments by CLSJ [14] reported good quality electron images and absence of dimers in the TOF mass spectrum at 200 torr, it is valid to think that the results obtained at this pressure better represent the behavior of the molecule. This means that the mode βCC could be a strong promoter of the formation of the isomer.

4. Conclusions

The experimental results have confirmed that after $S_1 \leftarrow S_0$ excitation in PA, the decay consists of a prompt short-lived component matching the measured singlet fluorescence lifetime (~75 ns) and a second component with very long lifetime. In addition, it has been observed that there are some vibrational modes that better promote the formation of the long-lived species than others. In fact, the normal coordinates of the 15 and βCC modes facilitate formation of the long-lived state and may be possible precursors of PA isomer responsible of the observed long-lived species.

III. Theoretical Calculations

A. Methods

Theoretical calculations were carried out using Gaussian 09 and GaussView v.3.0 [20]. Pople's notation is used to report the results, i.e. "/"means in the basis [21]. Density functional theory (B3LYP: Becke, Lee, Yang and Parr) was used with the aug-cc-pVDZ (ACCD) basis set.

B. Results and Discussions

The absolute energies of the ground, ground cation, and some of the lower singlet and triplet states of phenyl-vinylidene (PV), benzocyclobutadiene (BCBD) and cycloocta-1,3,5-trien-7yne (COTY) were calculated at B3LYP/aug-cc-pVDZ levels of theory. The results are shown in Table 3.2. Additionally, the same values were calculated for benzonitrile, anisole and pyrazine. These values are shown in Table 3.3.

To identify possible mechanisms that would lead to species with a long lifetime, the calculated states of the possible isomers were placed on an absolute scale with respect to the calculated energy of S_1 of PA, shown in Fig. 3.6. According to this figure, the triplet states of PA and PV; the S_1 and the triplet states of BCBD, and the S_1 and T_1 states of COTY might be reached from the S_1 state of PA. The ground states of the all the possible isomers might be also reached but the IP values from S_0 to D_0 are larger than the energy of the ionization (probe, 193 nm) laser.

Typically, the pump-probe ionization signal remaining after the singlet decay in aromatic molecules (e.g. anisole [22] and pyrazine [2, 6, 8]) has always been ascribed to the ionization of hot triplet levels with vibrational energy equal to the S_1-T_1 gap. The lifetime of a collisionless

triplet (presumably a result of intersystem crossing to S_0) varies dramatically with vibrational energy: the smaller the vibrational energy (small T_1-S_1 gap), the longer the lifetime because the Franck-Condon factors, which scale with the energy gaps, are very small at higher ΔE and the ISC from T_1 to S_1 would take longer [22]. The gap between the PA S_1 (reference energy from where the levels of the possible isomers could be reached; red line in Fig. 3.6) and the T_1 states of BCBD and PA are larger than the gap of the other two isomers; meaning that the T_1 states produced have higher energy. This suggests that the triplet states of these two molecules (PA and BCBD) should have a short lifetime. Since the pump-probe delayed ionization spectrum of PA finds a long lifetime species, one can rule out the initially produced triplet states of PA and BCBD as the possible candidates. The COTY S_0 state is only 0.6 eV below the triplet, a smaller T_1-S_0 gap as compared to the other possible isomers. This small gap might be low enough to suppress ISC between those states, resulting in the T_1 state having a long lifetime. However, the COTY T_1 calculated IP is 6.7 eV and this value is 0.3 eV above the energy of the ionization (probe, 193 nm) laser. Since this small energy difference is within the calculation errors, COTY T_1 is still a possible candidate to be the long-lived species, as previously suggested by H.X.S.J [1].

Fig. 3.6 shows that for all the molecules but COTY, ISC from PA S_1 to an excited triplet state like T_2 is possible. This excited triplet state (T_2) might then populate the T_1 states by fluorescence. For aromatic molecules of this size, such as anisole [23] and pyrazine [2, 6, 8], representing typical behavior (exponential decay showing the fast decay of the S_1 state by fluorescence and a longer, but still short, lifetime component due to hot T_1 state decay) such emission would be observed in the IR region. However, for PA and benzonitrile (BN, a molecule found to also show PA-like unusual photophysics) the T_2-T_1 gap is larger and the

emission would be expected to be in the near-IR region. So far there is still no experimental evidence for this mechanism, although H.X.S.J [1] searched for emission and did not detect it.

C. Conclusions

Placing the calculated states of the possible isomers on an absolute scale with respect to the calculated value of PA S_1 allows one to eliminate some of the possible mechanisms for the formation of the long-lived species seen in the decay of the laser-excited S_1 state of PA in pump-probe photoionization experiments. From the analysis of the PA S_1-T_1 and T_1-S_0 gaps, one could suggest COTY T_1as a strong candidate to be the long lifetime species. However, photoemission to a lower triplet level is a mechanism that should still be considered since there is still not strong experimental evidence to discard it.

Table 3.2: Absolute energies of the ground, ground cation and some of the lower singlet and triplet states of the PA isomers studied in this work: PV, BCBD and COTY.

	S_0 (Hartree)	T_1 (Hartree)	T_1 (eV)	T_2 (Hartree)	T_2 (eV)	S_1 (Hartree)	S_1 (eV)	Cation (D_0, Hartree)	IP (S_0) eV	IP (T_1) eV
PA	-308.410152	-308.326570	2.27	-308.261677	4.04	-308.240429	4.62	-308.117041	7.98	5.70
PV	-308.352948	-308.302695	1.37	-308.292309	1.65	-308.220644	3.60	-308.113527	6.51	5.15
BCBD	-308.392254	-308.333386	1.60	-308.259215	3.62	-308.285308	2.91	-308.121405	7.37	5.77
COTY	-308.334098	-308.310670	0.64	-308.219434	3.12	-308.268880	1.77	-308.063130	7.37	6.74

eV: Electron volts
Calculations done with B3LYP/aug-cc-pVDZ

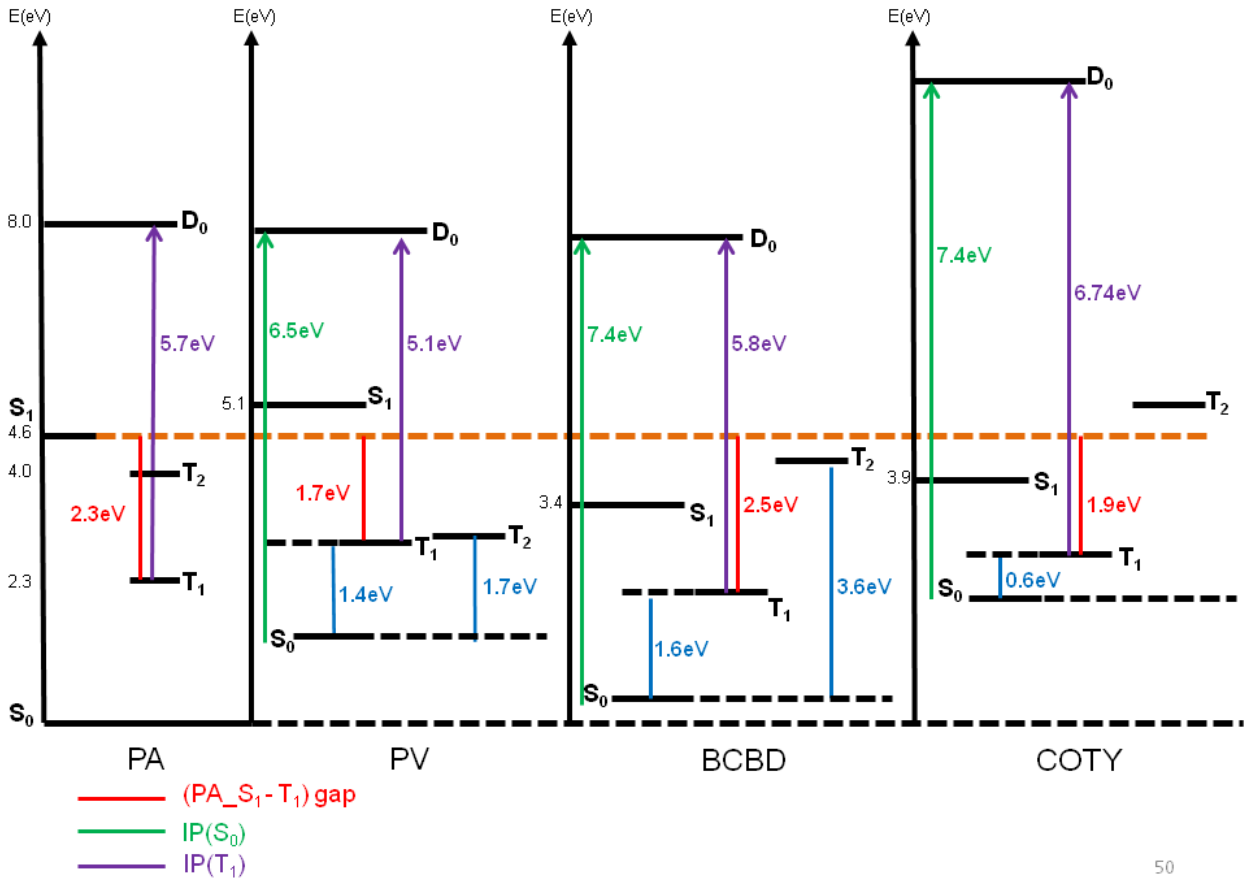

Figure 3.6: Electronic states of the PA isomers studied in this work with respect to the calculated value of PA S_1.

Table 3.3: Absolute energies and ionization potentials (IP) of the singlet and triplet states of PA, benzonitrile, anisole and pyrazine.

	S_0 (Hartree)	T_1 (eV)	S_1 (eV)	Cation (Hartree)	IP (S_0)	IP (T_1)	S_1-T_1 gap (eV)	T_2(eV)	T_2-T_1 (eV)
Phenylacetylene	-308.410152	2.27	4.62	-308.117041	7.98	5.70	2.34	4.04	1.77
Benzonitrile	-324.509878	2.49	4.75	-324.181094	8.95	6.46	2.26	4.01	1.52
Anisole	-346.812588	3.69	4.97	-346.518290	8.01	4.32	1.28	4.12	0.43
Pyrazine	-264.350310	3.21	4.63	-264.014595	9.13	5.92	1.42	3.95	0.74

eV: Electron volts
Calculations done with B3LYP/aug-cc-pVDZ

IV. Conclusions

Experimentally, we were able to confirm that following $S_1 \leftarrow S_0$ excitation the excited state decay, in the absence of collisions, consists of a prompt short-lived component matching the measured singlet fluorescence lifetime (~75 ns), and a second component with a very much longer lifetime. A pump-probe photoionization study of the individual bands located in the low energy part of the S_1 spectrum of PA, showed that some vibrational modes result in production of a larger amount of the long-lived species than others. From the ratios between the observed S_1 and long-lived species signals, excitation of the ν_{15} and $\nu_{\beta CC}$ vibrational modes promote greater amounts of the long-lived species, possibly implying they promote isomerization. Computational results show that the PA S_1-T_1 and the T_1-S_0 gaps for COTY T_1 are consistent with a species with long lifetime. Therefore, combining our experimental and theoretical observations, COTY T_1 emerges as a strong candidate to be the long lifetime species. However, the evidence is still far from conclusive and other experimental work (Chapter 4) is required to investigate the intriguing photophysics of phenylacetylene and benzonitrile, where similar behavior has been observed [1].

V. References

1. Hofstein J., Xu H. F., Sears T., Johnson P. M., *"Fate of excited states in jet-cooled aromatic molecules: Bifurcating pathways and very long lived species from the S-1 excitation of phenylacetylene and benzonitrile"*. Journal of Physical Chemistry A **112**, 1195 (2008).

2. Kommandeur J., Majewski W. A., Meerts W. L., Pratt D. W., *"Pyrazine - an Exact Solution to the Problem of Radiationless Transitions"*. Annual Review of Physical Chemistry **38**, 433 (1987).

3. Duncan M. A., Dietz T. G., Liverman R. E., *"Photoionization measurement of the triplet lifetime of benzene"*. Journal of Physical Chemistry **85**, (1981).

4. Otis C. E., Knee J. L., Johnson P. M., *"Nonradiative Processes in the Channel Three Region of the S-1 State of Ultracold Benzene"*. Journal of Physical Chemistry **87**, 2232 (1983).

5. Knee J. L., Otis C. E., Johnson P. M., *"Nonradiative-Transitions in Collisionless Perdeuterobenzene"*. J Chem Phys **81**, 4455 (1984).

6. Knee J., Johnson P., *"Lifetimes of Dissociation-Relaxed Triplet-States of Pyrazine and Pyrimidine"*. Journal of Physical Chemistry **89**, 948 (1985).

7. Dietz T. G., Duncan M. A., Puiu A. C., Smalley R. E., *"Pyrazine and pyrimidine triplet decay in a supersonic beam"*. Journal of Physical Chemistry **86**, (1982).

8. Hillenbrand S., Zhu L., Johnson P., *"The Pulsed Field-Ionization Spectrum and Lifetimes of the States at the S1 Origin of Pyrazine"*. Journal of Chemical Physics **95**, 2237 (1991).

9. Johnson P. M., Zhu L. C., *"Mass-Analyzed Threshold Ionization - Structural Information for a Mass-Spectrum and Mass Information for Ionic Spectroscopy"*. International Journal of Mass Spectrometry and Ion Processes **131**, 193 (1994).

10. Zhu L., Johnson P. M., *"Mass analyzed threshold ionization spectroscopy"*. J. Chem. Phys. **94**, (1991).

11. Knee J. L., Johnson P. M., *"Triplet-State Nonradiative Lifetimes of Collision-Free Aniline and Aniline-Argon Complexes above the S1 Origin"*. J Chem Phys **80**, 13 (1984).

12. Kennedy K. W., Echt O., *" Delayed electron emission from higher fullerenes Cn, n ≤ 96, following excitation at 1064 nm"*. Journal of Physical Chemistry **97**, (1993).

13. Schroeter K., Schroder D., Schwarz C., *"Structures of the C8H6+ cation formed upon loss of acetylene from ionized naphthalene"*. Journal of Physical Chemistry A **103**, 4174 (1999).

14. Chang C. H., Lopez G., Sears T. J., Johnson P. M., *"Vibronic Analysis of the S(1)-S(0) Transition of Phenylacetylene Using Photoelectron Imaging and Spectral Intensities Derived from Electronic Structure Calculations"*. Journal of Physical Chemistry A **114**, 8262 (2010).

15. Hofstein J. D., Goode J. G., Johnson P. M., *"A comparative investigation of Rydberg-state survival in several molecules using mass-analyzed threshold ionization"*. Chemical Physics Letters **301**, 121 (1999).

16. Xu H. F., Sears T., Johnson P. M., paper presented at the 61st. OSU International Symposium on Molecular Spectroscopy, The Ohio State University, Columbus, Ohio, 2006.

17. King G. W., So S. P., *"Ethynylbenzene: analysis of the 2790 A absorption spectrum"*. J. Molec. Spectrosc. **37**, 543 (1971).

18. Chia L., Goodman L., *"2-Photon Spectrum of Phenylacetylene"*. J Chem Phys **76**, 4745 (1982).

19. Serrano-Andres L., Merchan M., Jablonski M., *"The electronic spectra of aryl olefins: A theoretical study of phenylacetylene"*. J Chem Phys **119**, 4294 (2003).

20. *"Gaussian 09, Revision B.01"*, Frisch M. J., Trucks G. W., Schlegel H. B., Scuseria G. E., Robb M. A., Cheeseman J. R., Scalmani G., Barone V., Mennucci B., Petersson G. A., Nakatsuji H., Caricato M., Li X., Hratchian H. P., Izmaylov A. F., Bloino J., Zheng G., Sonnenberg J. L., Hada M., Ehara M., Toyota K., Fukuda R., Hasegawa J., Ishida M., Nakajima T., Honda Y., Kitao O., Nakai H., Vreven T., Montgomery J., J. A., Peralta J. E., Ogliaro F., Bearpark M., Heyd J. J., Brothers E., Kudin K. N., Staroverov V. N., Kobayashi R., Normand J., Raghavachari K., Rendell A., Burant J. C., Iyengar S. S., Tomasi J., Cossi M., Rega N., Millam N. J., Klene M., Knox J. E., Cross J. B., Bakken

V., Adamo C., Jaramillo J., Gomperts R., Stratmann R. E., Yazyev O., Austin A. J., Cammi R., Pomelli C., Ochterski J. W., Martin R. L., Morokuma K., Zakrzewski V. G., Voth G. A., Salvador P., Dannenberg J. J., Dapprich S., Daniels A. D., Farkas Ö., Foresman J. B., Ortiz J. V., Cioslowski J., Fox D. J. (Gaussian, Inc., Wallingford, CT., 2010)

21. Foresman J. B., Headgordon M., Pople J. A., Frisch M. J., *"Toward a Systematic Molecular-Orbital Theory for Excited-States"*. Journal of Physical Chemistry **96**, 135 (1992).

22. Morse M. D., Puiu A. C., Smalley R. E., *"Intramolecular Vibrational-Relaxation - Effects on Electronic Nonradiative Relaxation Rates"*. J Chem Phys **78**, 3435 (1983).

23. Yeretzian C., Selzle H., Schlag E., *"ZEKE spectroscopy: high-resolution laser spectroscopy in a modified time-of-flight mass spectrometer"*. Eur. Mass. Spectrom. **2**, (1996).

CHAPTER 4

FUTURE DIRECTIONS

The evidence to strongly support the recently observed and intriguing photophysics of PA (long-lived species) is still far from conclusive and additional experimental work is required. Actually, two experiments can be setup considering the equipment that is available to the group.

I. Ion fragmentation spectroscopy

The species produced by pump-probe photoionization (described in Chapter 3) can be irradiated with a tunable third laser with enough power to fragment the excited parent ions. Scanning the third laser and comparing the action spectrum to the photoinduced Rydberg ionization (PIRI) spectrum of the third excited electronic state of phenylacetylene cation obtained by Xu et al. [1] will provide more evidence of the mechanism of formation of the ong lifetime species. PIRI spectroscopy enables electronic spectroscopy to proceed from an experimentally defined vibrational level of the ground state of the cation. The neutral molecule is excited first to a particular vibrational level of the first excited state (S_1), and then selectively excited to a high Rydberg state associated with a particular vibrational of the ground state cation. Finally, the vibrationally selected cation is excited by a tunable laser photon which photodetaches the Rydberg electron, thus providing the cation spectrum according to symmetry and Franck-Condon factor selection rules [1]. Agreement of the ion fragmentation spectrum of the pump-probe photoionized species with Xu et al.'s spectrum would indicate that the long-lived species are triplet states of phenylacetylene cation formed from monomers. Disagrement would suggest isomer formation.

II. Matrix Isolation

Matrix isolation is a technique in which molecules are produced at very low temperatures (~10 K, -440 °F), low pressures (10^{-7} Torr), and keep them isolated from one another by placing them in a matrix of unreactive gas such as argon (Ar) or nitrogen (N_2). Generally, the full setup contains pumps to reduce the pressure, a refrigeration system and temperature controller to keep it cold, a manifold which allows us to control the argon and nitrogen, and the window upon which the chemistry is actually done. Usually, the system is a cart on wheels, which allows placing the window (i.e. CaF_2 window) in instruments such as an IR spectrometer and an UV/vis spectrometer [2, 3].

The sample will be the long-lived species produced within molecular beam by the pump-probe time delay experiment described in Chapter 3. The molecular beam will be deposited onto the cold window. By shining an IR laser onto the matrix window where the molecules have been isolated with Ar, one will obtain the infrared spectrum of the low temperature sample. Soft UV photolysis, temperature annealing and repeated infrared absorption spectroscopy permit a careful and controlled analysis of the sample. An infrared spectrum of the long-lived species would be extremely helpful in determining its identity. Additionally, one would be able to accumulate product (isolated long lifetime species) over a long period of time to get enough to see the spectrum.

III. References

1. Xu H. F., Johnson P. M., Sears T. J., *"Photoinduced rydberg ionization spectroscopy of phenylacetylene: Vibrational assignments of the C-similar to state of the cation"*. Journal of Physical Chemistry A **110**, 7822 (2006).

2. Menke J. L., "*Computational and Matrix-Isolation spectroscopy studies of Cyanocyclobutadienes (Chapter 6)*". University of Wisconsin-Madison (2010).

3. Jovan K. V., Gadre S. R., Sundararajan K., Viswanathan K. S., *"Effect of matrix on IR frequencies of acetylene and acetylene-methanol complex: Infrared matrix isolation and ab initio study"*. J Chem Phys **127**, 104501 (2007).

Complete list of references

1. King G. W., So S. P., *"Allowed and Forbidden Components in 2790 a System of Ethynylbenzene"*. Journal of Molecular Spectroscopy **33**, 376 (1970).

2. King G. W., So S. P., *"Ethynylbenzene - Vibrational Spectra of Some Deuterated Isomers"*. Journal of Molecular Spectroscopy **36**, 468 (1970).

3. King G. W., So S. P., *"Ethynylbenzene Analysis of 2790 a Absorption System"*. Journal of Molecular Spectroscopy **37**, 543 (1971).

4. King G. W., So S. P., *"Ethynylbenzene Calculations of Energies of Electronic States"*. Journal of Molecular Spectroscopy **37**, 535 (1971).

5. Padhye M. R., Rao B. S., *"Infrared Spectra of Substituted Acetylenes"*. Journal of Scientific and Industrial Research B **18B**, (1959).

6. Zhuravleva T. S., Nurmukhametov R. N., Kozlov Y. I., Shigorin D. N., *"Electronic transitions and spectra of phenylacetylene"*. Optika i Spektroskopiya **22**, 898 (1967).

7. Powers D. E., Hopkins J. B., Smalley R. E., *"Vibrational-Relaxation in Jet-Cooled Phenylalkynes"*. Journal of Chemical Physics **74**, 5971 (1981).

8. Chia L., Goodman L., *"2-Photon Spectrum of Phenylacetylene"*. Journal of Chemical Physics **76**, 4745 (1982).

9. Kim M. S., Kwon C. H., Kim H. L., *"Vibrational analysis of vacuum ultraviolet mass-analyzed threshold ionization spectra of phenylacetylene and benzonitrile"*. Journal of Physical Chemistry A **107**, 10969 (2003).

10. Evans J. C., Nyquist R. A., *"The Vibrational Spectra of Ethynyl Benzene and Ethynyl Benzene-D"*. Spectrochimica Acta **16**, 918 (1960).

11. Sponer H., Nordheim G., Sklar A. L., Teller E., *"Analysis of the near ultraviolet electronic transition of benzene"*. Journal of Chemical Physics **7**, 207 (1939).

12. Rappoport Z., *The Chemistry of Phenols*. (John Wiley & Sons Ltd., England ed., 2003).

13. Platt J. R., *"Classification of Spectra of Cata-Condensed Hydrocarbons"*. Journal of Chemical Physics **17**, 484 (1949).

14. Dyke J. M., Ozeki H., Takahashi M., Cockett M. C. R., Kimura K., *"A Study of Phenylacetylene and Styrene, and Their Argon Complexes Pa-Ar and St-Ar with Laser Threshold Photoelectron-Spectroscopy"*. Journal of Chemical Physics **97**, 8926 (1992).

15. Baltzer P., Karlsson L., Wannberg B., Ohrwall G., Holland D. M. P., M. M., Hayes M., von Niessen W., *"An experimental and theoretical study of the valence shell photoelectron spectrum of the benzene molecule"*. Chemical Physics **224**, (1997).

16. Maier J., in *Book "Kinetics of Ion-Molecule Reactions"*, P. Ausloos, Ed. (Plenum Press, New York, 1979).

17. Hufner S., *Photoelectron Spectroscopy*. (Springer-Verlag, New York,3th Edition ed., 2003).

18. Swiderek P., Gootz B., Winterling H., *"Electron-energy-loss spectroscopy of solid phenylacetylene"*. Chemical Physics Letters **285**, 246 (1998).

19. Ribblett J. W., Borst D. R., Pratt D. W., *"Styrene and phenylacetylene: Electronic effects of conjugating substituents "off" and "on" the axis of a benzene ring"*. Journal of Chemical Physics **111**, 8454 (1999).

20. Taylor D. P., Goode J. G., Leclaire J. E., Johnson P. M., *"Photoinduced Rydberg Ionization Spectroscopy"*. Journal of Chemical Physics **103**, 6293 (1995).

21. Xu H. F., Johnson P. M., Sears T. J., *"Photoinduced rydberg ionization spectroscopy of phenylacetylene: Vibrational assignments of the C-similar to state of the cation"*. Journal of Physical Chemistry A **110**, 7822 (2006).

22. Narayanan K., Chang G. C., Shieh K. C., Tung C. C., *"S-1<-S-0 transition of phenylacetylene: Ab initio and resonant two-photon ionization studies"*. Spectrochimica Acta Part a-Molecular and Biomolecular Spectroscopy **52**, 1703 (1996).

23. Philis J. G., Drougas E., Kosmas A. M., *"The (L-b)S-1 <- S-0 transition of phenylpropyne and phenylacetylene: an experimental and ab initio study"*. Chemical Physics **306**, 253 (2004).

24. Chang C. H., Lopez G., Sears T. J., Johnson P. M., *"Vibronic Analysis of the S(1)-S(0) Transition of Phenylacetylene Using Photoelectron Imaging and Spectral Intensities Derived from Electronic Structure Calculations"*. Journal of Physical Chemistry A **114**, 8262 (2010).

25. Serrano-Andres L., Merchan M., Jablonski M., *"The electronic spectra of aryl olefins: A theoretical study of phenylacetylene"*. Journal of Chemical Physics **119**, 4294 (2003).

26. Csaszar A. G., Fogarasi G., Boggs J. E., *"Theoretical Prediction of the Vibrational-Spectrum, Geometry, and Scaled Quantum-Mechanical Force-Field for Phenylacetylene"*. Journal of Physical Chemistry **93**, 7644 (1989).

27. King G. W., Van Putten A. A. G., *"Extended CNDO[complete neglect of differential overlap] calculations upon benzonitrile and ethynylbenzene"*. Journal of Molecular Spectroscopy **42**, (1972).

28. Amatatsu Y., Hasebe Y., *"Ab initio study on phenylacetylene in S-1 and S-2"*. Journal of Physical Chemistry A **107**, 11169 (2003).

29. Amatatsu Y., *" Reaction Coordinate Analysis of the S2-S1 Internal Conversion of Phenylacetylene"*. Journal of Physical Chemistry A **110**, (2006).

30. Hofstein J., Xu H. F., Sears T., Johnson P. M., *"Fate of excited states in jet-cooled aromatic molecules: Bifurcating pathways and very long lived species from the S-1 excitation of phenylacetylene and benzonitrile"*. Journal of Physical Chemistry A **112**, 1195 (2008).

31. Xu H. F., Sears T., Johnson P. M., paper presented at the 61st. OSU International Symposium on Molecular Spectroscopy, The Ohio State University, Columbus, Ohio, 2006.

32. Leopold D. G., Hemley R. J., Vaida V., Roebber J. L., *"Direct Absorption-Spectra of Higher Excited-States of Jet-Cooled Monosubstituted Benzenes - Phenylacetylene, Styrene, Benzaldehyde, and Acetophenone"*. Journal of Chemical Physics **75**, 4758 (1981).

33. Swiderek P., Gootz B., *"The low-lying singlet-triplet transitions of phenylacetylene and styrene: Analysis of the vibronic structure"*. Berichte Der Bunsen-Gesellschaft-Physical Chemistry Chemical Physics **102**, 882 (1998).

34. Johnson P. M., Xu H. F., Sears T. J., *"The calculation of vibrational intensities in forbidden electronic transitions"*. Journal of Chemical Physics **125**, (2006).

35. Johnson P. M., *"Molecular Multi-Photon Ionization Spectroscopy"*. Accounts of Chemical Research **13**, 20 (1980).

36. Taylor D. P., "*REMPI-PES Studies of Some Rydberg States of CO_2*". Doctoral Thesis, State University of New York at Stony Brook (1993).

37. Dixit S. N., McKoy V., *"Theory of resonantly enhanced multiphoton processes in molecules"*. J. Chemical Physics **8**, (1985).

38. Verges J., Effantin C., D'Incan D., Cooper D. L., Barrow R. F., *"Double-minimun (2)1Σu+ state of sodium dimer"*. Physical Review Letters **53**, (1984).

39. Hurst G. S., *"Resonance Ionization Spectroscopy"*. Analytical Chemistry **53(13)**, (1981).

40. Townsend D., Minitti M. P., Suits A. G., *"Direct current slice imaging"*. Review of Scientific Instruments **74**, (2003).

41. Garcia G. A., Nahon L., Powis I., *"Two-dimensional charged particle image inversion using a polar basis function expansion"*. Rev Sci Instrum **75**, (2004).

42. Dribinski V., Ossadtchi A., Mandelshtam V. A., Reisler H., *"Reconstruction of Abel-transdormable images: The Gaussian basis-set expansion Abel transform method"*. Review of Scientific Instruments **73**, (2002).

43. Zhou J., "*Slow Electron Velocity-map Imaging Spectroscopy of small radicals and infrared multiphoton dissociation study of solvated systems.*". University of California, Berkeley (2008).

44. Chestakov D. A., Wu S. M., Parker D. H., Eppink A., Kitsopoulos T. N., *"Slicing Using a Conventional Velocity Map Imaging Setup: O2, I2, and I2+ Photodissociation"*. J Phys Chem A **108**, (2004).

45. Sato Y., Matsumi Y., Kawasaki M., Tsukiyama K., Bersohn R., *"Ion Imaging of the Photodissociation of OCS near 217 and 230 nm"*. J Phys Chem-Us **99**, (1995).

46. Bordas C., Paulig F., Helm H., Huestis D. L., *"Photoelectron imaging spectroscopy: Principle and inversion method"*. Rev Sci Instrum **67**, (1996).

47. Wilson E. B., *"The Normal Modes and Frequencies of Vibrations of the Regular Plane Hexagon Model of the Benzene Molecule"*. Physical Review **45**, (1934).

48. Schutte C. J. H., Bertie J. E., Bunker P. R., Hougen J. T., Mills I. M., Watson J. K. G., Winnerwisser B. P., *"Notations and Conventions in Molecular Spectroscopy: Part 2. Symmetry Notation"*. International Union of Pure and Applied Chemistry **69**, (1977).

49. Schutte C. J. H., Bertie J. E., Bunker P. R., Hougen J. T., Mills I. M., Watson J. K. G., Winnerwisser B. P., *"Notations and Convenctions in Molecular Spectroscopy: Part 2. Symmetry Notation"*. International Union of Pure and Applied Chemistry **69**, (1997).

50. Herzberg G., *Molecular Spectra and Molecular Structure: II. Infrared and Raman Spectra of Ploya tomic Molecules*. (D. Van Nostrand Company, Inc., Princenton ed., 1945).

51. Herzberg G., *Molecular Spectra and Molecular Structure: III. Electronic Spectra and Electronic Structure of Polyatomic Molecules*. (D. Van Nostrand Company, Inc., Princeton ed., 1966).

52. Lin J. L., Tzeng W. B., *"Identification of impurities in phenylacetylene by species-selected mass-analyzed threshold ionization spectroscopy"*. Applied Spectroscopy **57**, 1178 (2003).

53. O'Keefe A., Deacon D. A. G., *"Cavity ring-down optical spectrometer for absorption measurements using pulsed laser sources"*. Review of Scientific Instruments **59**, (1988).

54. Paldus B. A., Kachanov A. A., *"An historical overview of cavity-enhaced methods"*. Canadian Journal of Physics **83**, (2005).

55. Lehmann K., Berden G., Engeln R., in *Book "An introduction to Cavity Ring-Down Spectroscopy"*. (Blackwell Publishing, Ltd., 2009).

56. Berden G., Peeters R., Meijer G., *"Cavity-ring-down spectroscopy: experimental schemes and applications"*. International Reviews in Physical Chemistry **19**, (2000).

57. Markiewicz B., Milan M., Teslja A., Chang C. H., Hall G. (To Be Published).

58. Bacon A. R., Hollas J. M., Ridley T., *"Herzberg-Teller intensity stealing in the 279-nm system of phenylacetylene: Evidence from single vibronic level fluorescence spectra"*. Canadian Journal of Physics **62**, (1984).

59. Hohenberg P., Kohn W., *"Inhomogeneous Electron Gas"*. Physical Review **136**, B864 (1964).

60. Tawada Y., Tsuneda T., Yanagisawa S., Yanai T., Hirao K., *"A long-range-corrected time-dependent density functional theory"*. Journal of Chemical Physics **120**, 8425 (2004).

61. Chai J. D., Head-Gordon M., *"Long-range corrected hybrid density functionals with damped atom-atom dispersion corrections"*. Physical Chemistry Chemical Physics **10**, 6615 (2008).

62. Tozer D. J., Handy N. C., *"Improving virtual Kohn-Sham orbitals and eigenvalues: Application to excitation energies and static polarizabilities"*. Journal of Chemical Physics **109**, 10180 (1998).

63. Kamiya M., Tsuneda T., Hirao K., *"A density functional study of van der Waals interactions"*. Journal of Chemical Physics **117**, 6010 (2002).

64. Yanai T., Tew D. P., Handy N. C., *"A new hybrid exchange-correlation functional using the Coulomb-attenuating method (CAM-B3LYP)"*. Chemical Physics Letters **393**, 51 (2004).

65. Richard R. M., Herbert J. M., *"Time-Dependent Density-Functional Description of the (1)L(a) State in Polycyclic Aromatic Hydrocarbons: Charge-Transfer Character in Disguise?"*. Journal of Chemical Theory and Computation **7**, 1296 (2011).

66. Dunning T. H., *"Gaussian-Basis Sets for Use in Correlated Molecular Calculations .1. The Atoms Boron through Neon and Hydrogen"*. Journal of Chemical Physics **90**, 1007 (1989).

67. Tang B. Z., Law C. C. W., Lam J. W. Y., Qin A. J., Dong Y. Q., Kwok H. S., *"Synthesis, thermal stability, light emission, and fluorescent photopatterning of poly (diphenylacetylene)s carrying naphthalene pendant groups"*. Polymer **47**, 6642 (2006).

68. Duschinsky F., *"On the interpretation of electronic spectra of polyatomic molecules"*. Acta Physico-Chimica U.R.S.S. **7**, (1937).

69. *"Gamess Version 11 Aug. 2011 (R1) and Version 11 Apr. 2008 (R1)"*, Schmidt M. W., Baldridge K. K., Boatz J. A., Elbert S. T., Gordon M. S., Jensen J. H., Koseki S., Matsunaga N., Anguyen K. A., Su S. J., Windus T. L., Dupuis M., Montgomery J. A. (J. Comp. Chem. 14, 1347-1363(1993), 2010, 2011)

70. *"Gaussian 09, Revision B.01"*, Frisch M. J., Trucks G. W., Schlegel H. B., Scuseria G. E., Robb M. A., Cheeseman J. R., Scalmani G., Barone V., Mennucci B., Petersson G. A., Nakatsuji H., Caricato M., Li X., Hratchian H. P., Izmaylov A. F., Bloino J., Zheng G., Sonnenberg J. L., Hada M., Ehara M., Toyota K., Fukuda R., Hasegawa J., Ishida M., Nakajima T., Honda Y., Kitao O., Nakai H., Vreven T., Montgomery J., J. A., Peralta J. E., Ogliaro F., Bearpark M., Heyd J. J., Brothers E., Kudin K. N., Staroverov V. N., Kobayashi R., Normand J., Raghavachari K., Rendell A., Burant J. C., Iyengar S. S., Tomasi J., Cossi M., Rega N., Millam N. J., Klene M., Knox J. E., Cross J. B., Bakken V., Adamo C., Jaramillo J., Gomperts R., Stratmann R. E., Yazyev O., Austin A. J., Cammi R., Pomelli C., Ochterski J. W., Martin R. L., Morokuma K., Zakrzewski V. G., Voth G. A., Salvador P., Dannenberg J. J., Dapprich S., Daniels A. D., Farkas Ö., Foresman J. B., Ortiz J. V., Cioslowski J., Fox D. J. (Gaussian, Inc., Wallingford, CT., 2010)

71. Borrelli R., Peluso A., *"Dynamics of radiationless transitions in large molecular systems: A Franck-Condon-based method accounting for displacements and rotations of all the normal coordinates"*. Journal of Chemical Physics **119**, 8437 (2003).

72. Sears T. J., *"The calculation of the energy levels of an asymmetric top free radical in a magnetic field"*. Computer Physics Reports **2**, (1984).

73. Sears T. J., *"ASYTOP - A program for detailed analysis of gas phase magnetic resonance spectra of asymmetric top molecules"*. Computer Physics Communications **34**, (1984).

74. Mulliken R. S., *"Electronic Population Analysis on LCAO-MO Molecular Wave Functions. I "*. Journal of Chemical Physics **23**, (1955).

75. Wheeler R. A., Sinha P., Boesch S. E., Gu C. M., Wilson A. K., *"Harmonic vibrational frequencies: Scaling factors for HF, B3LYP, and MP2 methods in combination with correlation consistent basis sets"*. Journal of Physical Chemistry A **108**, 9213 (2004).

76. Cox A. P., Ewart I. C., Stigliani W. M., *"Microwave-Spectrum, Structure and Dipole-Moment of Phenylacetylene"*. Journal of the Chemical Society-Faraday Transactions Ii **71**, 504 (1975).

77. Kommandeur J., Majewski W. A., Meerts W. L., Pratt D. W., *"Pyrazine - an Exact Solution to the Problem of Radiationless Transitions"*. Annual Review of Physical Chemistry **38**, 433 (1987).

78. Duncan M. A., Dietz T. G., Liverman R. E., *"Photoionization measurement of the triplet lifetime of benzene"*. Journal of Physical Chemistry **85**, (1981).

79. Otis C. E., Knee J. L., Johnson P. M., *"Nonradiative Processes in the Channel Three Region of the S-1 State of Ultracold Benzene"*. Journal of Physical Chemistry **87**, 2232 (1983).

80. Knee J. L., Otis C. E., Johnson P. M., *"Nonradiative-Transitions in Collisionless Perdeuterobenzene"*. Journal of Chemical Physics **81**, 4455 (1984).

81. Knee J., Johnson P., *"Lifetimes of Dissociation-Relaxed Triplet-States of Pyrazine and Pyrimidine"*. Journal of Physical Chemistry **89**, 948 (1985).

82. Dietz T. G., Duncan M. A., Puiu A. C., Smalley R. E., *"Pyrazine and pyrimidine triplet decay in a supersonic beam"*. Journal of Physical Chemistry **86**, (1982).

83. Hillenbrand S., Zhu L., Johnson P., *"The Pulsed Field-Ionization Spectrum and Lifetimes of the States at the S1 Origin of Pyrazine"*. Journal of Chemical Physics **95**, 2237 (1991).

84. Johnson P. M., Zhu L. C., *"Mass-Analyzed Threshold Ionization - Structural Information for a Mass-Spectrum and Mass Information for Ionic Spectroscopy"*. International Journal of Mass Spectrometry and Ion Processes **131**, 193 (1994).

85. Zhu L., Johnson P. M., *"Mass analyzed threshold ionization spectroscopy"*. J. Chem. Phys. **94**, (1991).

86. Knee J. L., Johnson P. M., *"Triplet-State Nonradiative Lifetimes of Collision-Free Aniline and Aniline-Argon Complexes above the S1 Origin"*. Journal of Chemical Physics **80**, 13 (1984).

87. Kennedy K. W., Echt O., *" Delayed electron emission from higher fullerenes Cn, n ≤ 96, following excitation at 1064 nm"*. Journal of Physical Chemistry **97**, (1993).

88. Schroeter K., Schroder D., Schwarz C., *"Structures of the C8H6+ cation formed upon loss of acetylene from ionized naphthalene"*. Journal of Physical Chemistry A **103**, 4174 (1999).

89. Hofstein J. D., Goode J. G., Johnson P. M., *"A comparative investigation of Rydberg-state survival in several molecules using mass-analyzed threshold ionization"*. Chemical Physics Letters **301**, 121 (1999).

90. King G. W., So S. P., *"Ethynylbenzene: analysis of the 2790 A absorption spectrum"*. J. Molec. Spectrosc. **37**, 543 (1971).

91. Foresman J. B., Headgordon M., Pople J. A., Frisch M. J., *"Toward a Systematic Molecular-Orbital Theory for Excited-States"*. Journal of Physical Chemistry **96**, 135 (1992).

92. Johnson P. M., Anand R., Hofstein J. D., LeClaire J. E., *"Reassessing the orbitals of pi systems using photoinduced Ryberg ionization spectroscopy"*. Journal of Electron Spectroscopy and Related Phenomena **108**, 177 (2000).

93. Menke J. L., "*Computational and Matrix-Isolation spectroscopy studies of Cyanocyclobutadienes (Chapter 6)*". University of Wisconsin-Madison (2010).

94. Jovan K. V., Gadre S. R., Sundararajan K., Viswanathan K. S., *"Effect of matrix on IR frequencies of acetylene and acetylene-methanol complex: Infrared matrix isolation and ab initio study"*. Journal of Chemical Physics **127**, 104501 (2007).

APPENDIX A

SCRIPT NAME: ZiprunG09-GOOD

DESCRIPTION:

This BASH-based script submits Gaussian 09 jobs automatically to a multiprocessor machine and extracts the relevant transition moments along with some other information, like output file names and input file titles, from the output files as they are finished. The script operates on *.tar.gz files and steps through all the zipped input file components of them. Additionally, it creates duplicates of the checkpoint file declared in the input syntax for each input file. When the script is done, the user should expect a folder named “PAbatchout” with tar files containing output and checkpoint files plus a text file named “Info-to-create-database.txt” that will allow the user to create the database to run the vibronic simulation later. This script does not require any particular directory to run, it takes the path automatically and the user just needs to place the script in the directory where the *.tar.gz file is located.

LOCATION:

The script can be found at the BNL Linux-based Computers: CTS5 & 6: /home/trevor/gaussiancalc/

INPUT SYNTAX:

[ ]$ ziprunG09-GOOD <****.gjf.tar.gz> <chkpointfile> <# of processors> <excited state #>

example:

[ ]$ ziprunG09-GOOD trialgjf.tar.gz trial.chk 16 2 & (to extract second excited state TM)

PROGRAM:

```
**************************************************************************
#!/bin/bash
#Input syntax is ziprunG09-GOOD <input archive.tar.gz> <chkpointfile> <# of processors>
<state>
path=$(pwd)
i=0                                                    #initialize index
if  [ ! -d $path/PAbatchinp ]                          #set up temp input directory
  then
     mkdir $path/PAbatchinp
  else
     rm -f $path/PAbatchinp/*.*
  fi
if  [ ! -d $path/PAbatchout ]                          #see if temp output directory exists
  then
     mkdir $path/PAbatchout                            #if not, make one
  else
     if [ ! -d $path/PAbatchout/backup ]
     then
      mkdir $path/PAbatchout/backup                    #make a backup directory
      fi
  mv -f $path/PAbatchout/*.* $path/PAbatchout/backup   #move all its files to backup
  fi
cp -f $1 $path/PAbatchinp                              #put archive in temp input directory
cd $path/PAbatchinp                                    #go to the input directory
archbase=${1%.*z}                                      #to get a base name for the output archive,
archbase=${archbase%.*r}                               #strip the extensions from the input archive
archbase=${archbase%g*f}                               #also strip inp from the end, if there
gunzip < $1 | tar xf -                                 #unzip the archive in the input directory
for input in *.gjf; do                                 #step through the input files
   filebase=${input%.*f}                               #strip the extension
   infile="$filebase""_.gjf"                           #name for temporary input file
   cp $input $infile
   mv -f "$infile" $path
   cd $path
   for chkfile in "$2"; do                             #take chkpoint file given in the command line
    inchk="$filebase"".chk"                            #create a copy of chkpoint file
    cp $chkfile $inchk          #copy chkpoint file in command line into the copy done before
   done
   outfile="$filebase"".out"                           #name for output file
   outlist="$outlist $outfile"                         #add to output file list
   nohup rung09 <"$infile" > "$outfile" &              #submit job
   let "i += 1"                                        #increment index
   let "rem = $i % $3"                                 #index--modulo--# of processors
   if [ "$rem" -eq "0" ]                               #see if all processors are used
```

```
    then
     sleep 10                                    #give rungms a chance to launch the programs
     for job in `ps -C "rung09" -o pid=`; do     #find pid's of the running jobs
      wait $job                                  #wait until all ongoing jobs are finished
     done
    outlist="" #restart the output file list
    rm -f *_.gjf                                #remove the temporary input files
    fi
    cd $path/PAbatchinp                         #return to the temp input directory
done
sleep 10                                        #wait for the last jobs to get launched
for job in `ps -C "rung09" -o pid=`; do         #find the running jobs
 wait $job                                      #wait until final jobs are finished
done
cd $path
for abc in *.out; do                            #extracting info from output files
 bas=${abc%.*t}
 fil="$bas"".txt"
 grep -A 4 "#T" $path/$abc >> "$fil"
 grep -m 1 "Framework group" $path/$abc >> "$fil"
 grep -A 11 "dipole moments (Au):" $path/$abc >> "$fil"
 for def in "$fil"; do
  basa=${def%.txt}
  fila="$basa""data.txt"
  sed -n 3p $path/$def >> "$fila"
  echo ${basa} >> "$fila"
  sed -n 4p $path/$def >> "$fila"
  sed -n 5p $path/$def >> "$fila"
  sed -n 12p $path/$def >> "$fila"
  sed -n 14p $path/$def >> "$fila"
  for line in "$4"; do
  let state="$line+14"
  sed -n ${state}p $path/$def >> "$fila"
  done
 done
 for ghi in "$fila"; do
  basb=Info-to-create-database
  filb="$basb"".txt"
  cat $fila >> "$filb"
 done
rm -f $fil
rm -f $fila
done
mv -f $filb $path/PAbatchout
tar cf -  *.out | gzip > "$archbase""out.tar.gz"          #gzip the *.out files
tar cf -  *.chk |gzip > "$archbase""chk.tar.gz"           #gzip the *.chk files
```

```
mv -f "$archbase""out.tar.gz" $path/PAbatchout
mv -f "$archbase""chk.tar.gz" $path/PAbatchout
rm -f *.out
rm -f *.chk
rm -f *_.gjf
rm -f $path/PAbatchinp/*.*                    #remove contents of temp input directory
rmdir $path/PAbatchinp                        #remove the temp input directory
*****************************************************************************************
```

APPENDIX B

SCRIPT NAME: TransitionMomentsExtraction

DESCRIPTION:

This BASH-based script extracts transition moments, output file names and titles. This script is included in ZiprunG09-GOOD. This script does not require any particular directory to run, it takes the path automatically and the user just needs to place the script in the directory where the output files are located.

LOCATION:

The script can be found at the BNL Linux-based Computers: CTS5 & 6: /home/trevor/gaussiancalc/

INPUT SYNTAX:

[ ]$ TransitionMomentsExtraction <excited state #>

example:

[ ]$ TransitionMomentsExtraction 2 & (to extract second excited state TM and info)

PROGRAM:

****

```
#!/bin/bash
#Input syntax is TransitionMomentsExtraction <excited state>
path=$(pwd)
for res in *.out; do
 filebase=${res%.*t}
 file="$filebase"".txt"
```

```
 grep -A 4 "#T" $path/$res >> "$file"
 grep -m 1 "Framework group" $path/$res >> "$file"
 grep -A 11 "dipole moments (Au):" $path/$res >> "$file"
 for rest in "$file"; do
 filebased=${rest%.txt}
 filed="$filebased""data.txt"
 sed -n 3p $path/$rest >> "$filed"
 echo ${filebased} >> "$filed"
 sed -n 4p $path/$rest >> "$filed"
 sed -n 5p $path/$rest >> "$filed"
 sed -n 12p $path/$rest >> "$filed"
 sed -n 14p $path/$rest >> "$filed"
 for line in "$2";do
 let state="$line+14"
 sed -n ${state}p $path/$rest >> "$filed"
 done
 done
 for resta in "$filed"; do
 filbase=Info-to-create-database
 fil="$filbase"".txt"
 cat $filed >> "$fil"
 done
 rm $file
 rm $filed
done
*********************************************************************************
```